THERMOBAROMETRIC CONSTRAINTS ON THE EVOLUTION OF THE MENDERES MASSIF (WESTERN TURKEY): INSIGHTS INTO THE METAMORPHIC HISTORY OF A COMPLEXLY-DEFORMED REGION

By

CENK OZERDEM

Masters of Science

Oklahoma State University

Stillwater, OK

2004

Submitted to the Faculty of the
Graduate College of the
Oklahoma State University
in partial fulfillment of
the requirements for
the Degree of
MASTER OF SCIENCE
July, 2004

THERMOBAROMETRIC CONSTRAINTS ON THE EVOLUTION OF THE MENDERES MASSIF (WESTERN TURKEY): INSIGHTS INTO THE METAMORPHIC HISTORY OF A COMPLEXLY-DEFORMED REGION

Thesis Approved

Dr. Elizabeth J. Catlos

_____

Thesis Adviser

Dr. Ibrahim Çemen

_____

Dr. Stan Paxton

_____

Dr. Al Carlozzi

_____

Dean of the Graduate College

ACKNOWLEDGMENTS

First and foremost, I would like to thank Dr. Elizabeth Catlos, thesis adviser, for her scientific guidance, encouragement, patience, introducing me to this research project and most important for her friendship, which helped me get over a lot of things. My special thanks go Dr. Ibrahim Çemen who was helpful in contributing to my studies, for his advice, and suggestions for improvement and for being my committee member. I would also like to thank Dr. Stan Paxton for being my committee member and sharing his knowledge in classroom studies.

I am thankful to Oguz Gögűş for encouraging me with his never-ending energy. His deep interest in research always amazed me. I wish to thank Dr. Veysel Işık, Dr. Hasan Sözbilir and Mr. Ökmen Sűmer for directing me to some important literature and also sample location areas in western Turkey.

I do wish to express my appreciation to my friends Burcu Özdemir, Idil Atalık, Sibel Irmak, and Pelin Koz for their support and kind assistance.

I am thankful to Halil Kahraman, his family for their hospitality and helping me to find the rocks in the field. I'm also thankful to the people in Horzumalayaka village for helping me find my way in the area.

Last but not least, I would like to thank to my parents Gűlay and Erkan Özerdem, and my sister, Selen, for the financial and emotional support throughout my graduate studies. This thesis is dedicated to all of them.

TABLE OF CONTENTS

LIST OF FIGURES

LIST OF TABLES

1. INTRODUCTION: THE MENDERES MASSIF IN PERSPECTIVE

1.1 Introduction to the Menderes Massif

The Aegean extended region (Figure 1.1) experienced a series of continental collisions from Late Cretaceous to Eocene, which led to the formation of the Izmir-Ankara Neo-Tethyan suture zone (e.g., Şengör and Yılmaz, 1981; Stampfli, 2000). The collision zone may have extended southwestward, possibly close to the present position of the Hellenic arc (e.g., Doglioni et al. 1999). Post-collisional extension in the region, although controversial in its timing and nature, caused the exhumation of several Alpine metamorphic belts, termed the Menderes, Crete, Rhodop and Kazdag Massifs (Figure 1.1). The largest of these, the Menderes Massif, accommodated a significant amount of extension, covering an area of >40,000 km^2 between the Izmir-Ankara Neo-Tethyan suture in the north and the Lycian Nappes to the south. The mechanisms that create and facilitate large-scale extension of the Earth's crust are not well-understood, thus the Menderes Massif is a key locale for studying the processes involved.

The Massif is considered as a metamorphic core complex, which forms during continental extension when deformation in the upper crust is localized by detachment faults (e.g., Dewey, 1988; Gessner et al. 2001). Metamorphic core complexes were first described in the Basin and Range province of the North American Cordillera (Coney, 1980). The presence of metamorphic core complexes in the Aegean region was first proposed by Lister et al. (1984) based on their work in the Cycladic massif in the Aegean Sea (Işık et al. 2003) (Figure 1.1).

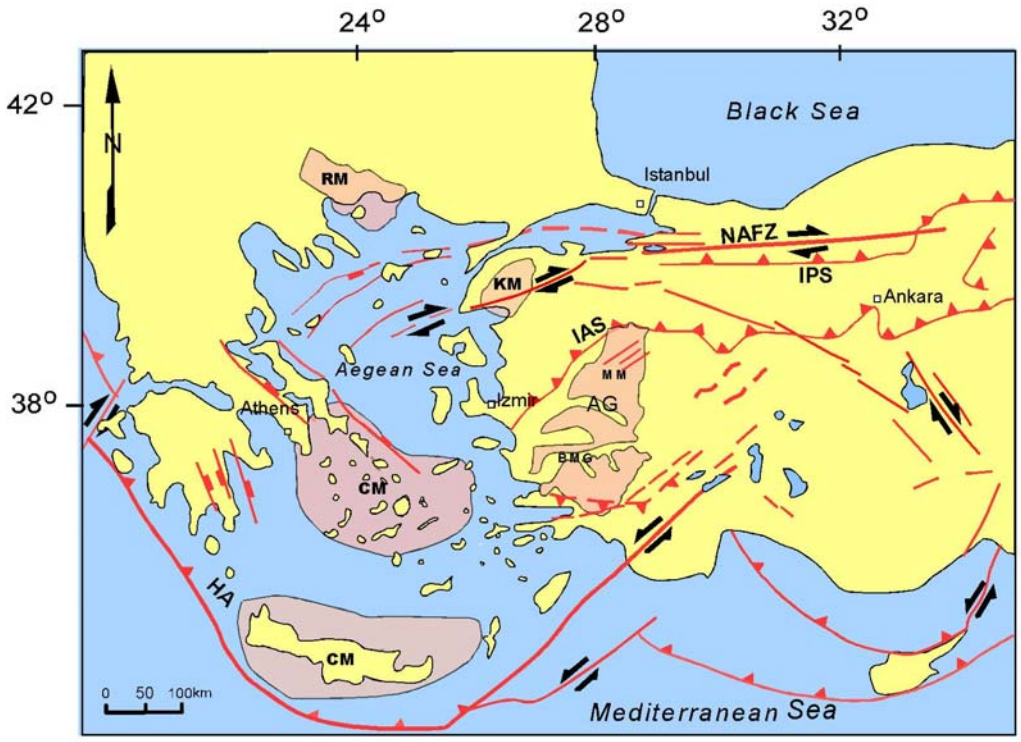

Figure 1.1 Generalized tectonic map of Western Turkey and Aegean Sea showing major structural elements. Abbreviations: BMG=Buyuk Menderes Graben, AG = Alaşehir Graben, IAS= Izmir-Ankara Suture zone, NAFZ=North-Anatolian Fault Zone, IPS= Intrapontid Suture Zone, HA=Hellenic Arc

Although the metamorphic core complex origin of the Menderes Massif has been generally accepted (e.g., Hetzel et al. 1995a, b; Lips et al. 2001; Gessner et al. 2001; Işık et al. 2003), the timing and mechanism of post-collisional extension that created the Menderes Massif are controversial (e.g., Seyitoglu and Scott 1996b; Yılmaz et al. 2000; Bozkurt and Oberhaensli, 2001; Bozkurt, 2003; Işık et al. 2003). Mineral grains in rocks from the Menderes Massif record multiple events, including a Pan-African (Cambro-Ordovician) (Satır and Friedrichsen, 1986; Hetzel and Reischmann, 1996; Hetzel et al. 1998; Loos and Reischmann, 1999; Candan et al. 2001; Gessner et al. 2004) to early/late-Cenozoic history (Eocene-Oligocene; Satır and Friedrichsen, 1986; Hetzel and Reischmann, 1996; Bozkurt and Satır, 2000; Lips et al. 2001). Extensional exhumation

began sometime in the mid- to late Cenozoic (Oligocene-Miocene; Seyitoglu et al. 1992; Jolivet et al. 1994; Hetzel et al. 1995a,b; Seyitoglu and Scott, 1996a; Gessner et al. 2001a; Lips et al. 2001).

To decipher the peak metamorphic conditions recorded by rocks in the Menderes Massif, many researchers have carried out thermobarometric studies (e.g., central Menderes Massif: Akkök, 1983; Ashworth and Evirgen, 1985; Oberhaensli et al. 1997; Bozkurt and Oberhaensli, 2001a; Okay, 2001; Candan et al. 2001; Ring et al. 2001; southern Menderes Massif: Ashworth and Evirgen, 1985; Bozkurt and Park, 1994; Bozkurt, 1996; Oberhaensli, 2001; Whitney and Bozkurt, 2002; Rimmele et al. 2003; northern Menderes Massif, Okay and Satir, 2000).

To ascertain the pressure-temperature (P-T) conditions experienced by rocks in the central Menderes Massif metamorphic core complex and identify if Menderes Massif garnets record a polymetamorphic history, the Oklahoma State University (OSU) JEOL 733 Electron Microprobe was used to X-ray element map and identify garnet zoning types. The Electron Microprobe was also used for mineral identification, describing and classifying rocks. The machine's spatial resolution makes it a powerful tool for studying zoned minerals. Garnet [$(Fe,Mg,Mn,Ca)Si_3O_8$] has the capability to record the P-T evolution of a sample by variations in Fe, Mg, Mn and Ca (e.g., Spear, 1993; Kohn and Spear, 2000). These zoned crystals record the chemical reaction history of the Menderes Massif and provide evidence for how the range evolved and was created.

1.2 Broader Scale Models for the Evolution of the Menderes Massif

Three major models have been proposed to explain the cause of the extreme extension in the Aegean Region:

(1) *Lateral Extrusion/Tectonic Escape*: In this model, the Anatolian plate moves towards the Aegean along the North and East Anatolian Faults in response to the collision of Arabia and Eurasia (Figure 1.1) (e.g., Dewey and Şengör, 1979; Şengör and Yılmaz, 1981; Şengör et al. 1985; Çemen et al. 1999; Yılmaz et al. 2000; Bozkurt, 2001);

(2) *Back-Arc Spreading*: In this model, the migration of the Hellenic Arc trench system (Figure 1.1) to the south-southwest gave rise to an extensional regime in the back-arc Aegean region (e.g., Le Pichon and Angelier, 1979; 1981; Meulenkamp et al. 1988; Buick, 1991; Okay and Satir, 2000);

(3) *Orogenic collapse*: In this model, thickened and elevated continental crust due to Alpine orogeny extensionally collapses and thins (e.g., Berkhemer, 1977; Jolivet et al., 1994; Dewey, 1988; Seyitoglu and Scott, 1992; Seyitoglu and Scott, 1996b; Bozkurt, 2001).

Timing the initiation of extension in the region can identify which of these models apply to the creation of the Menderes Massif. In this thesis, minerals suitable for future geochronology (e.g., monazite and zircon) were identified in several Menderes Massif rocks. However, the main focus of this thesis is obtaining peak P-T conditions and garnet zoning maps from rocks in the central Menderes Massif. These results were then used to elucidate the tectonic nature and evolution the range.

1.3 Methods of Analyses and Brief Summary of the Results

During the summer of 2003, samples were collected from the central Menderes Massif. The rocks were identified using a handlens and detailed petrographic analyses were made to identify which had suitable mineral assemblage for thermobarometric calculations.

Using the OSU Electron Microprobe, three major zoning types are identified in Menderes Massif garnets: retrograde zoning (compositions affected by diffusion), prograde zoning (preserves compositions during growth), and polymetamorphic zoning (compositional changes during multiple stages of garnet growth). Garnet-based P-T conditions are frequently used to evaluate and develop models for the tectonic evolution of the Menderes Massif. If the garnets are detrital, polymetamorphic, or developed during a previous metamorphic event, using their compositions in combination with matrix minerals generates misleading conditions and erroneously constrained tectonic models. The P-T conditions generated from Menderes Massif rocks in this thesis are consistent with their mineral assemblages, and are high-P (ranging from 8 to 12 kbar) and moderate-T (~500ºC-750ºC).

1.4 Organization of the Thesis

This thesis is organized into five chapters. Chapter 2 describes the previous geochronologic and thermobarometric studies done in the Menderes Massif. Chapter 3 outlines and justifies the research question in this thesis. The major models for the evolution of the Menderes Massif are reviewed in detail. Chapter 4 describes the methodology used to obtain thermobarometric data from rocks collected from metamorphic units that are associated with the detachment. Chapter 5 shows and describes the thermobarometric data and X-ray element maps obtained from rocks collected along the three transects.

2. GEOLOGIC BACKGROUND: EMPHASIS ON PREVIOUS WORK

2.1. Rocks and Structures Associated with the central Menderes Massif

The Menderes Massif is divided into northern (Gördes), central and southern (Çine) submassifs based on the presence of E-W trending grabens, northern Alaşehir (Gediz) and southern Bűyűk Menderes (Figure 2.1) (see Bozkurt et al. 2001). These grabens separate the central Menderes metamorphic core complex from the adjacent Gördes Massif to the north and the Çine Massif to the south (Figure 2.1).

Rocks of the Menderes Massif are classified by lithology and metamorphic history (e.g., Şengör et al. 1984; Gessner et al. 2001). In one interpretation, the lowest unit is a high-grade Cambro-Ordovician gneissic series termed the "Core Series" and the overlying Paleozoic schist and Mesozoic-Cenozoic marble are considered "Cover Series" (e.g., Dűrr, 1975; Şengör and Yılmaz, 1981; Şengör et al. 1984; Satır and Friedrichsen, 1986; Dora et al. 1995; Loos and Reischmann, 1999). The Core Series consists of granitic augen gneisses, paragneisses, schists, and minor migmatites. The oldest clearly documented geological event in the Core Series is the intrusion of large volumes of granites at ~550 Ma in the southern and central Menderes massif (Reischmann et al. 1991; Loos and Reischmann, 1995; Hetzel and Reischmann, 1996). These intrusions are presumably related to a Pan-African orogeny and most of them were subsequently transformed to augen gneisses (Şengör et al. 1984; Dora et al. 1995).

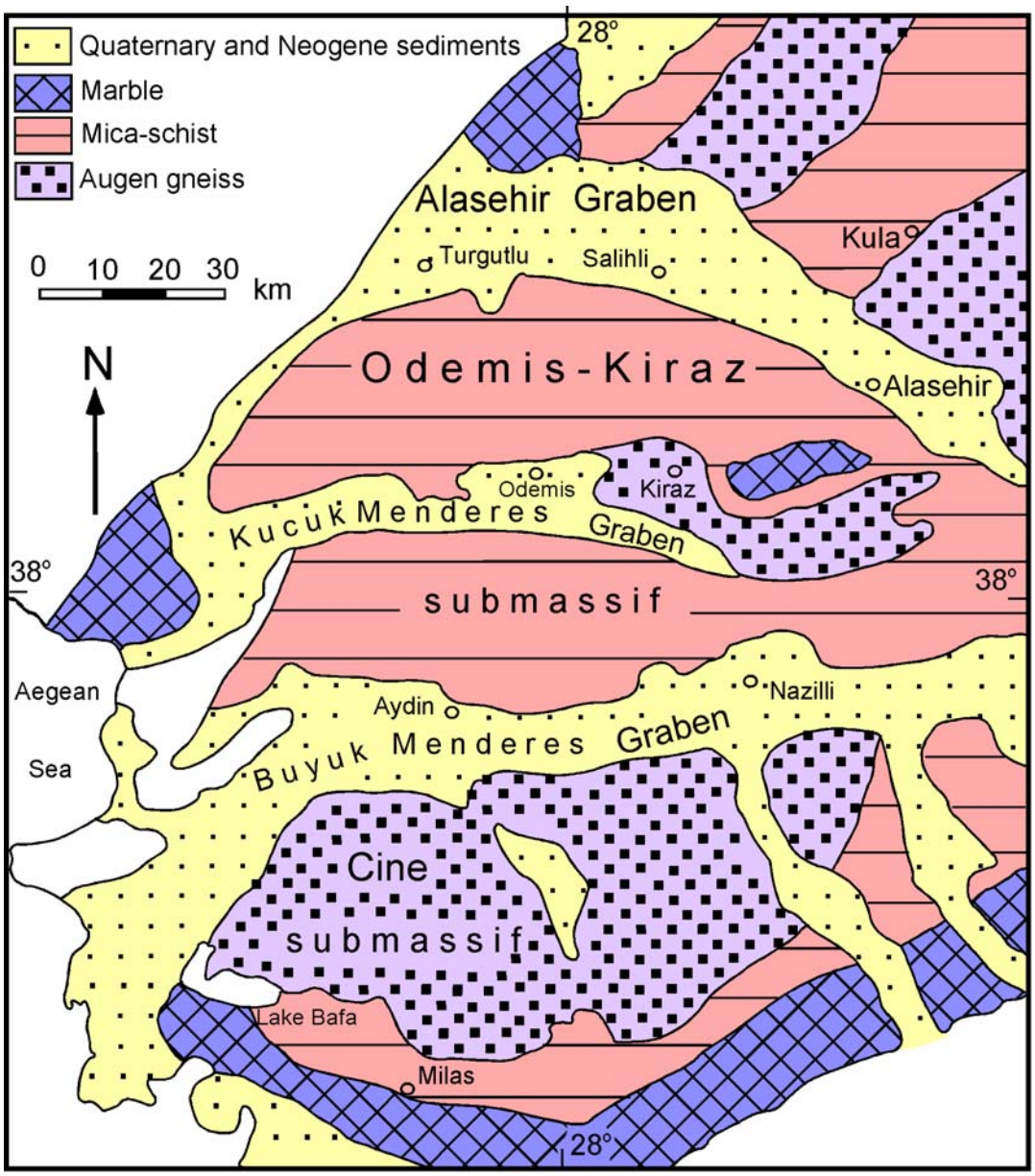

Figure 2.1 General map of the Menderes Massif [after Hetzel et al. (1995a)]

The presence of a metaconglomerate in the Cover series in the southern Menderes Massif that contains pebbles presumably derived from the Core Series suggests that the Paleozoic/Mesozoic Cover Series has been deposited unconformably on the Core Series

(Dora et al. 1995). The lower part of the Cover Series consists of low- to medium-grade schists, phyllites, and quartzites, whereas the upper part is dominated by marbles (Dűrr, 1975). The Core and the lower part of the Cover Series are thought to have both experienced two phases of deformation and metamorphism in the Triassic and Alpine. The Triassic episode reached greenschist facies metamorphic conditions in the eastern part of the central submassif (Derbent area; Akkök, 1983). This phase was followed by the intrusion of the post-tectonic Late Triassic Dede Dagi granite (Dora et al. 1995). The Alpine phase affected the entire Menderes massif and reached upper greenschist to upper amphibolite facies conditions (Akkök, 1983; Ashworth and Evirgen, 1984).

In a series of papers, the traditional Core/Cover interpretation has been disputed (e.g., Ring et al. 1999; Gessner et al. 2001; Işık and Tekeli, 2001). For example, Figure 2.2 shows a cross section through the Menderes Massif after Gessner et al. (2001). The Bayindir and Bozdag nappes are metapelitic assemblages with amphibolite and marble lenses. Overlying the Bayindir and Bozdag nappes is a Proterozoic-Cambrian basement called the Çine nappe and an upper metasedimentary succession of intercalated marble and calcschist termed the Selimiye nappe. The Bayindir nappe may have experienced only one major Alpine tectonometamorphic event, whereas the overlying Bozdag, Çine and Selimiye nappes record both pre-Alpine and Alpine events (Ring et al. 1999).

The central Menderes metamorphic core complex is bounded by two detachments: the north-dipping (10-20°N) Kuzey detachment (e.g., Hetzel et al. 1995a;b) and the south-dipping (5-15°S) Guney detachment (e.g., Emre and Sözbilir, 1997) (Figures 2.2). These structures cut upper levels of the nappe pile for a distance of 80 km and sole into the Alaşehir (Gediz) and Bűyűk Menderes Grabens, respectively (Figure 2.2). Gessner et

al. (2001) and Hetzel et al. (1995b) report the presence of an overall dome-shaped foliation pattern and north-northeast trending stretching lineation. They indicate that the asymmetry of shear bands and quartz c-axis fabrics on either side of the structural dome record a top to the north-northeast shear sense along the Kuzey detachment and a top to the south and southwest shear sense along the Guney detachment surface. The presence of these two opposite-dipping detachments led to the development of a bivergent-rolling hinge model for the evolution of the central Menderes metamorphic core complex (Gessner et al. 2001).

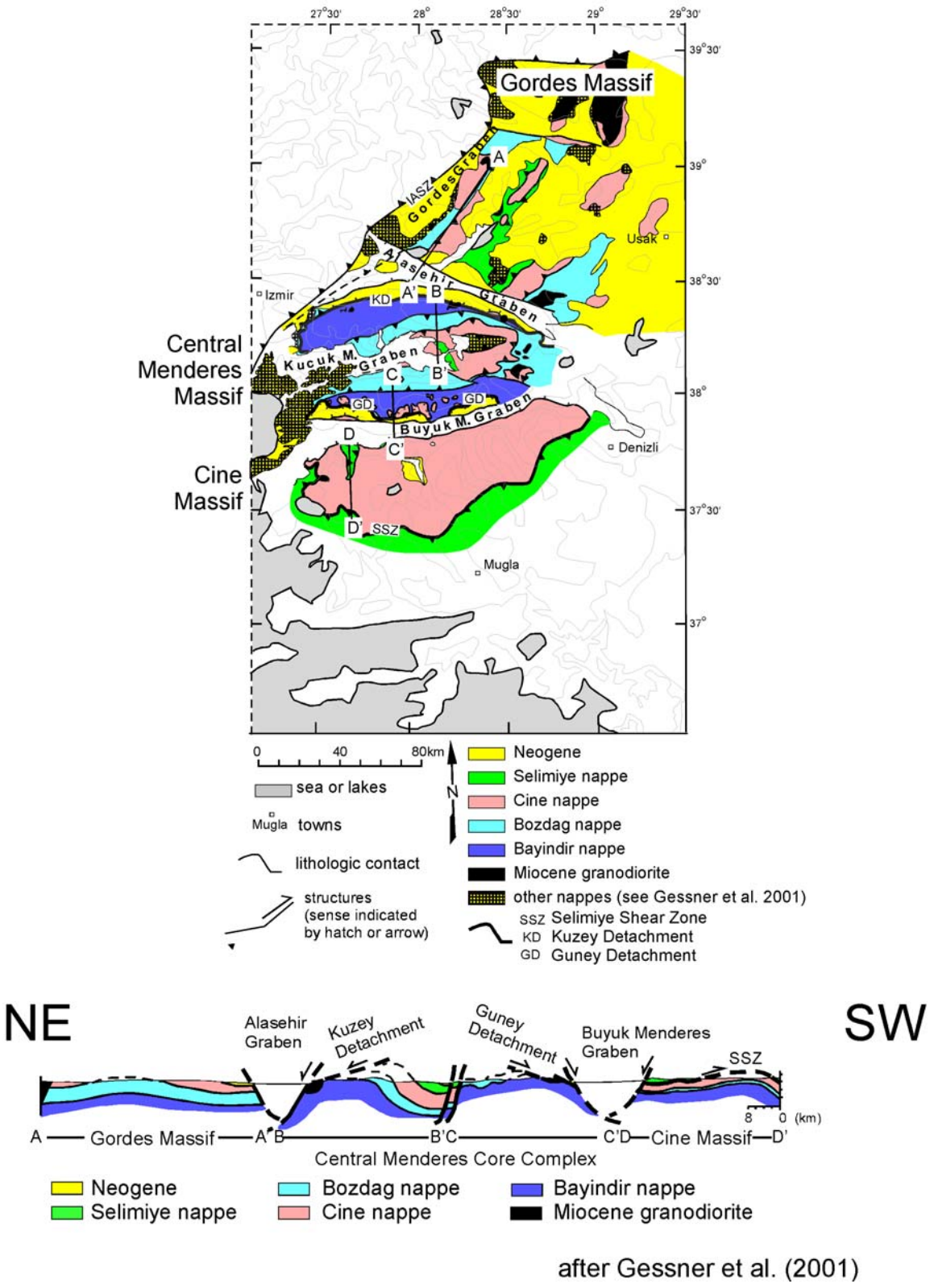

Figure 2.2 (Upper) Geologic map and (lower) cross-section through the Menderes Massif after Gessner et al. (2001).

2.2 Previous Work

2.2.1 Geochronology

Attempts to obtain the metamorphic history of the region include U-Pb and $^{207}Pb/^{206}Pb$ single zircon isotope dilution, Th-Pb monazite, K-Ar and $^{40}Ar/^{39}Ar$ biotite, muscovite, and amphibole Rb-Sr whole rock and mica and apatite and zircon fission track geochronology. Results from these studies (Tables 2.1-2.3) show rocks of the Menderes Massif experienced a prolonged and complicated tectonic history.

Table 2.1 Ages of rocks from the northern Menderes Massif

Lithology, locality	Age (Ma)	Method	Reference
Metagranites and orthogneisses; Entire Anatolide belt	2555-1740	$^{207}Pb/^{206}Pb$ Single zircon evaporation	Reischmann et al. 1991
Granodiorite whole rock	471±9	Rb/Sr	Satır and Freidrichsen, 1986
Granite gneiss	288±5,229±5	Rb/Sr	Satır and Freidrichsen, 1986
Egrigoz granitoid; Northern MM	23-20	$^{40}Ar/^{39}Ar$ biotite isochron age	Reischmann et al. 1991; Işık et al. 2004
Acid Volcanic domes	18.4±0.8 to 16.3±0.5	K-Ar biotite isochron age	Seyitoglu et al. 1992
Tourmaline leucogranite dykes	24.2±0.8 to 21.1±1.1	K-Ar muscovite isochron age	Seyitoglu et al. 1992

Table 2.2 Ages of rocks from the central Menderes Massif

Lithology, locality	Age (Ma)	Method	Reference
Birgi metagranite	551±1.4	U-Pb zircon dating	Hetzel et al. 1998
Granites; Bozdag nappe	~240-250	$^{207}Pb/^{206}Pb$ Single zircon evaporation	Koralay et al. 1998
Salihli granodiorite	19.5±1.4	$^{40}Ar/^{39}Ar$ Amphibole isochron age	Hetzel et al. 1995a
Alaşehir graben sediments	19-20 to 14-15	Sporomorph	Seyitoglu and Scott, 1996a
Turgutlu and Salihli granodiorites	13.1±0.2 to 12.2±0.4	$^{40}Ar/^{39}Ar$ Biotite isochron age	Hetzel et al. 1995a
Kuzey detachment;	7±1	$^{40}Ar/^{39}Ar$ Muscovite isochron age	Lips et al. 2001
Kuzey detachment;	4.5±1.0	Th-Pb monazite	Catlos et al. 2002

Table 2.3 Ages of rocks from the southern Menderes Massif

Lithology, locality	Age (Ma)	Method	Reference
Metagranites and orthogneisses;	659±7; 563±3 – 521±8	$^{207}Pb/^{206}Pb$ Single zircon evaporation, U-Pb dating	Loos and Reischmann, 1999
Metagranite in Selimiye shear zone	546.2±1.2	$^{207}Pb/^{206}Pb$ Single zircon evaporation	Hetzel and Reischmann, 1996
Granite gneiss	502±10	Rb/Sr	Satır and Freidrichsen, 1986
Granite gneiss	61±1	Rb/Sr	Satır and Freidrichsen, 1986
Granite gneiss	48±1	Rb/Sr	Satır and Freidrichsen, 1986
Augen gneiss, schist	43-37	$^{40}Ar/^{39}Ar$ Muscovite isochron age	Hetzel and Reischmann, 1996
Orthogneiss, Guney detachment	36±2	$^{40}Ar/^{39}Ar$ Muscovite isochron age	Lips et al. 2001

Timing slip along the north-dipping Kuzey detachment and south dipping Guney detachment has implications for understanding the exhumation history of the central Menderes Metamorphic Core Complex (e.g., Lips et al. 2001). Hetzel et al. (1995a,b) proposed that extension initiated along a detachment surface in early Miocene (19.5±1.4 Ma), based on the $^{40}Ar/^{39}Ar$ amphibole age from a syn-extensional (?) granodiorite that intruded prior to brittle deformation along the detachment surface. However, the argon age spectrum and correlation diagram of the Kuzey detachment amphibole shows that the sample is affected by excess argon (Figure 2.3). Hetzel et al. (1995a) note that the amphibole concentrate from the granodiorite shows "a complex release spectrum without a plateau age" and a higher than atmospheric $^{40}Ar/^{36}Ar$ ratio of 370.3±6.1, indicating the presence of excess argon. Despite this recognition, the isochron age is frequently cited as a reliable constraint for early Miocene extension (e.g., Hetzel et al. 1995a; Seyitoglu and Scott, 1996; Gessner et al. 2001; Lips et al. 2001).

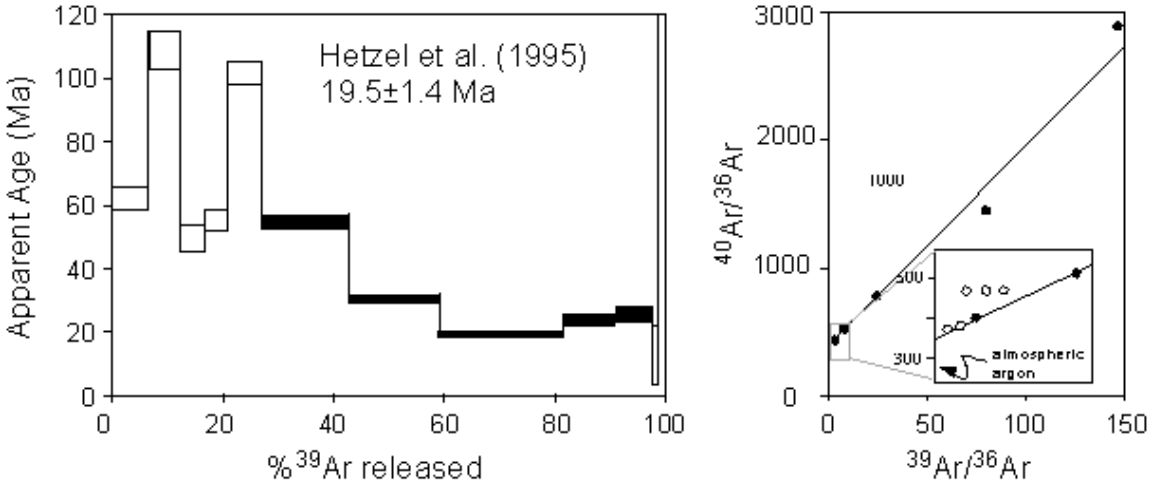

Figure 2.3 Results of step-heated amphibole argon age spectra and correlation diagram after Hetzel et al. (1995a). Note that the correlation isochron for this sample intersects $^{40}Ar/^{36}Ar$ values at a non-atmospheric value. Black steps (left figure) correlate to black circles (right figure)**,** and were used to calculate the isochron age of 19.5±1.4 Ma.

The extensional origin of the granodiorite is also controversial (Yılmaz et al. 2000). The granodiorite may be related to crustal thickening during the formation of the Izmir-Ankara suture zone. The interpretation precludes an Early Miocene initiation age of extension in western Turkey.

Lips et al. (2001) recognized the benefits of *in situ* geochronology in the region, the attempted to step-heat handpicked grains of syn-kinematic muscovite collected from the Bűyűk Menderes graben and Kuzey Detachment. Their laser probe step-heating experiments resulted in large analytical errors attributed to the analysis of small samples, therefore low argon retentivities (Figure 2.4).

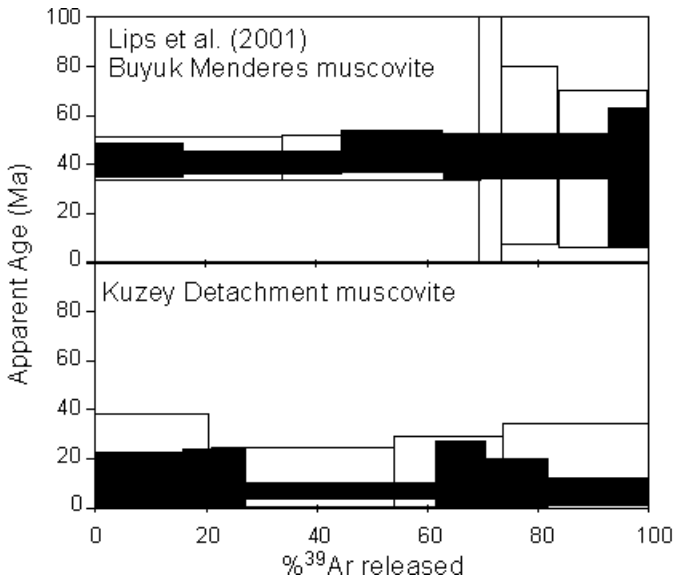

Figure 2.4 Results of $^{40}Ar/^{39}Ar$ laser-probe experiments of two muscovite samples from the Buyuk Menderes **(upper)** and two muscovite samples from the Kuzey Detachment **(lower)** after Lips et al. (2001). Note the large uncertainties.

Lips et al. (2001) discarded the step-heating results in Figure 2.4 and reported single fusion muscovite ages of 36±2 Ma from the Bűyűk Menderes graben and 7±1 Ma from the Kuzey detachment. The Oligocene muscovite age was attributed to recrystallization of the deformational fabric, which was accompanied or followed by extensional ductile faulting along the southern margin of the Menderes Massif, whereas the Late Miocene age was attributed to the last stage of activity along the Kuzey detachment or to continuous movement along the low-angle fault zone (Catlos and Çemen, 2004).

Catlos and Çemen (2004) report Th-Pb ages of monazite inclusions in garnet and in the rock matrix from a sample on the Kuzey detachment surface (Figure 2.5). The garnet contains an Ordovician monazite inclusion and younger monazites in the matrix. This matrix monazite is only found in reaction with allanite. The association of monazite with allanite is interpreted as a decompression feature because the 4.5±1.0 Ma monazite

grain is younger than any speculated compressional event and the age is within 1σ of the apatite fission track result of 3.7±0.6 Ma from a rock collected along the same detachment (Gessner et al. 2001).

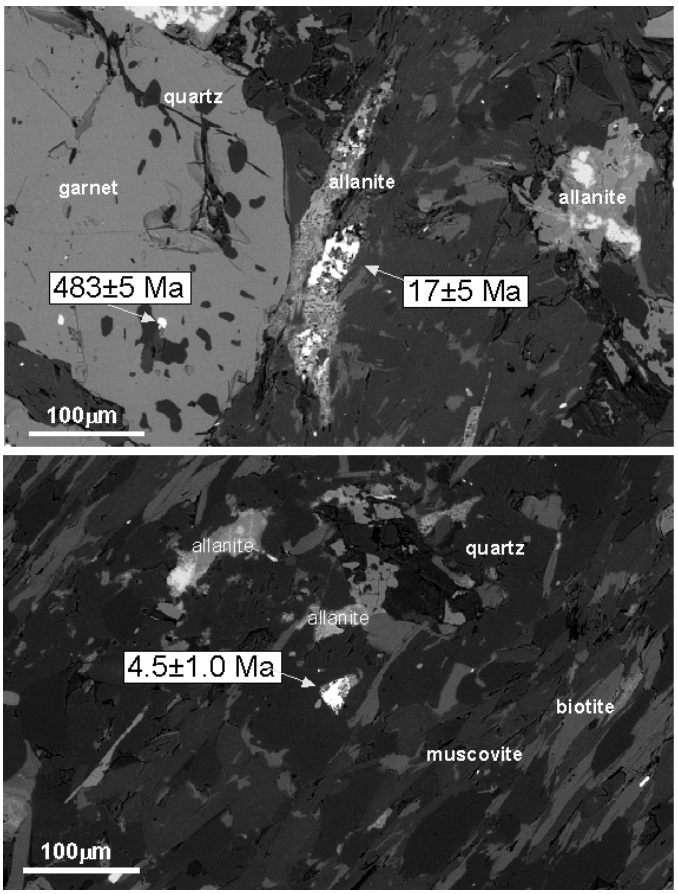

Figure 2.5 Backscattered electron images of a central Menderes metamorphic core complex sample with Th-Pb monazite ages indicated (1σ) (see Harrison et al. 2002; Catlos and Çemen, 2004). Other minerals present in the rock are labeled. Scale bars are indicated in each image.

The textures and ages in Figure 2.4 are important because they indicate early Pan-African metamorphism that was overprinted in the Miocene and Pliocene. Clearly, the chemistry of the garnet and its inclusions would not yield P-T conditions relevant to Cenozoic peak metamorphic conditions or extension. This is an important factor in

petrologically interpreting these rocks as many reported P-T conditions may not be relevant to Cenozoic metamorphism and tectonics.

2.2.2 Thermobarometery

Previous attempts at obtaining the peak P-T conditions from rocks of the Menderes Massif include garnet-biotite and garnet-clinopyroxene thermometry, garnet-bioite-plagioclase-clinopyroxene-quartz, garnet-biotite-muscovite-biotite, and garnet-sillimanite-plagioclase barometry. Table 2.4 shows the previous thermobarometric calculations from different regions in the Menderes Massif. Note that most of these studies focus on rocks of the southern and central Menderes Massif.

Table 2.4 P-T data from rocks of the Menderes Massif.

Lithology, locality	T (°C)	P (kbar)	Reference
northern Menderes Massif			
sillimanite-gneisses	640±50	5±1	Okay and Satır, 2000
central Menderes Massif			
eclogites	580 – 660	~15	Candan et al. 2001
retrograded eclogites	~650	~13	Oberhaensli et al. 1997
Metapelitic rocks	480 – 660	6.1 – 10.8	Ring et al. 2001
garnet-bearing rocks	530±40	8±2	Okay, 2001
garnet-bearing rocks	450-660	5 - 8	Akkök, 1983;
pelite	450 – 600	4 - 7	Ashworth and Evirgen, 1985
southern Menderes Massif			
Eclogitic gabbro	510 – 690	10 – 12	Candan et al. 2001
magnesiocarpholite, chloritoid, chlorite and sudolite	~440	10 – 12	Rimmele et al. 2003
Metasedimentary rocks	525 – 650	7 – 11	Regnier et al. 2003
garnet-bearing schist	~430 – ~550	~ 8	Whitney and Bozkurt, 2002
Metapelitic rocks	550 – 730	6.2 – 6.5	Ring et al. 2001
garnet-bearing rocks	530±50	5.5 – 6.1	Ashworth and Evirgen, 1984

Figure 2.6 shows the previous work done in the Menderes Massif on a P (depth) – T plane. These conditions overlie the greenschist, epidote-amphibolite, amphibolite, and eclogite facies. Northern Menderes Massif shows the lowest pressure conditions (~5

kbar, ~ 15 km), whereas the central Menders Massif exposes eclogites, which lie at the highest pressures (~15 kbar, ~55 km).

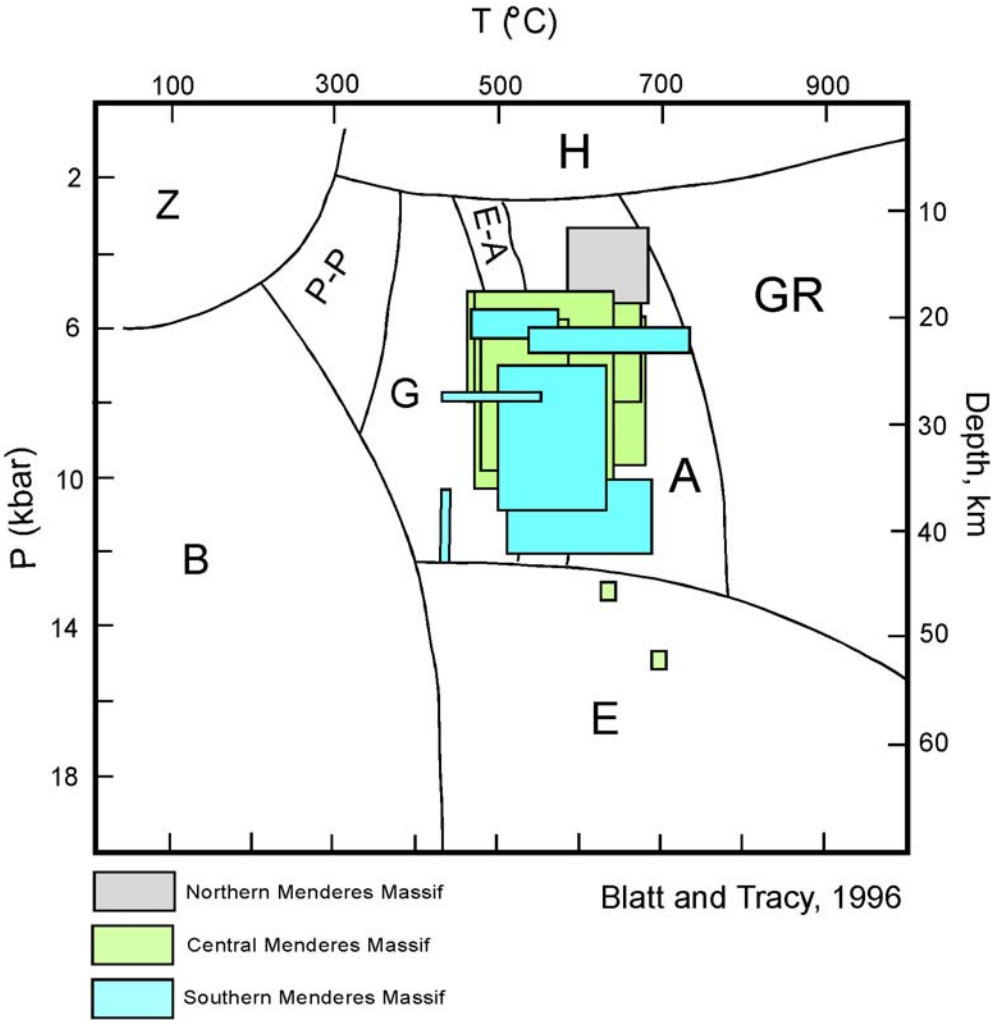

Figure 2.6 Plot of P (depth) – T plane showing distribution of metamorphic facies (after Blatt and Tracy, 1996). Data shown is from Ashworth and Evirgen, (1984), (1985); Oberhaensli, (1997); Okay and Satır, (2000); Candan (2001); Okay (2001); Ring et al. (2001); Whitney and Bozkurt (2002); Regnier et al. (2003); Rimmele et al. (2003). Abbreviations: A, Amphibolite; B, Blueschist; E, Eclogite; E-A, Eclogite-Amphibolite; G, Greenschist; GR, Granulite, H, Hornfels; P-P, Prehnite-Pumpellyite, Z: Zeolite.

3. DETAILED DESCRIPTION OF THE RESEARCH QUESTION

3.1 Introduction

Previous strategies approached the problem of the origin of extension in the Menderes Massif by geochronology (e.g., Satır and Freidrichsen, 1986; Seyitoglu et al. 1992; Hetzel et al. 1995a; Hetzel and Reischmann, 1996; Loos and Reischmann, 1999; Lips et al. 2001), field mapping (e.g., Sözbilir, 2001; Işık et al. 2003) and garnet-based thermobarometry (e.g., Ashworth and Evirgen, 1984, 1985; Oberhaensli et al. 2001; Whitney and Bozkurt, 2002; Regnier et al. 2003; Rimmele et al. 2003). This thesis addresses the third approach. Garnets in the Menderes Massif are assumed to form during a single time (e.g., Bozkurt, 1996; Whitney and Bozkurt, 2002), however, the data in this thesis suggest that some Menderes Massif garnets can form during the Cambro-Ordovician (Figure 2.5).

The purpose of the thesis is to establish the P-T histories of rocks collected near the Kuzey detachment of the central Menderes Massif as a means to identify if garnets record a polymetamorphic history. Justification for this approach is presented in section 3.2

3.2 Justification of the Research Question

This study tests the hypothesis that polymetamorphic garnets exist along the Kuzey detachment in the central Menderes Massif in western Turkey. The following list

is an attempt to outline the significance of understanding the P-T conditions experienced by rocks in the Menderes Massif.

1. *Thermobarometry of rocks in the Menderes Massif can be used to evaluate the feasibility of models that seek to explain large-scale extension.*

The timing and cause of extension in the Menderes Massif is still in debate. Three end-member models have been proposed to describe the formation of the area including lateral extrusion/tectonic escape, back arc spreading, and orogenic collapse (e.g., Seyitoglu and Scott, 1996).

In the lateral extrusion/tectonic escape model, the Anatolian plate moves towards the Aegean along the North and East Anatolian Faults in response to the collision of Arabia and Eurasia (Figure 3.1) (e.g., Dewey and Şengör, 1979; Şengör and Yılmaz, 1981; Şengör et al. 1985; Çemen et al. 1999; Yılmaz et al. 2000; Bozkurt, 2001).

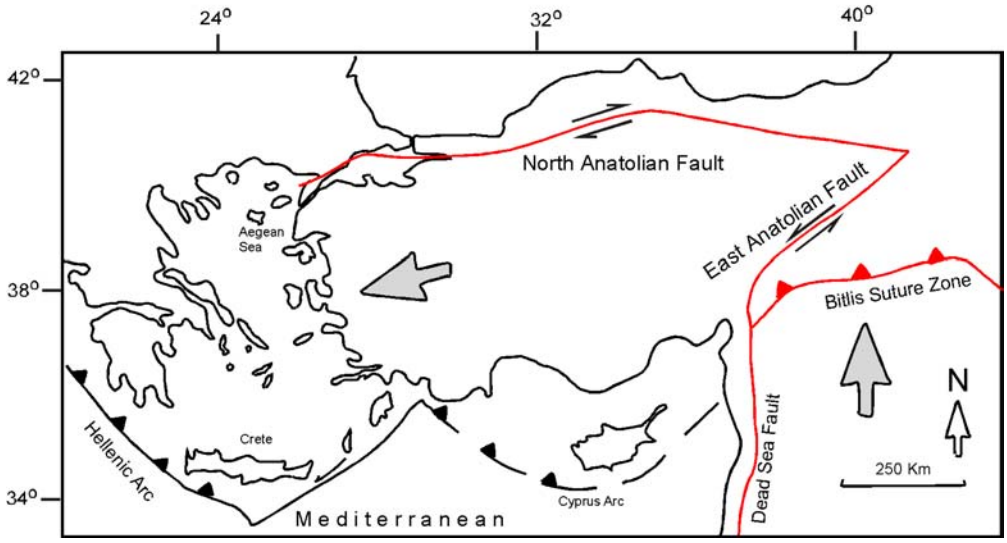

Figure 3.1 General area map of Turkey showing the lateral escape. The arrow on western Turkey indicates the location of the Menderes Massif and also the direction of the movement of Anatolian plate along North and East Anatolian Faults.

Tapponnier et al. (1982) used plane indentation experiments on confined blocks of plasticine to understand the intracontinental deformation and the evolution of strike-slip faulting in eastern Asia. In this experiment, a "rigid" block indents a "plastic" body. The rigid block represents India, whereas the plastic body represents Asia. The indenter is 5 cm wide and hits the plasticine at a constant rate of 2.5 cm/h. This number was chosen due to simple geometric and kinematic comparisons with the collision between India and Asia (~5 cm/yr of convergence along a collision front of ~ 2000 km; see Figure 3.2). The asymmetry of collisional deformations in Asia suggests that continental lithosphere in western Eurasia offers more resistance comparing to the east. The first goal of this experiment was to test this hypothesis in the situation of a free lateral boundary (Figure 3.2).

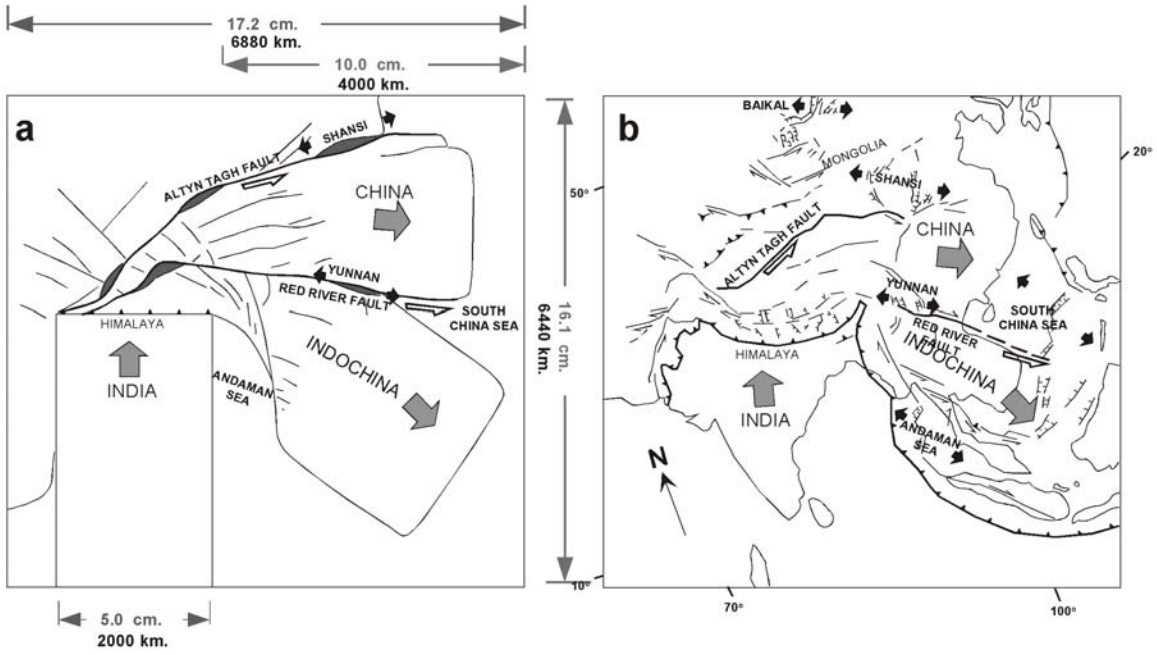

Figure 3.2 Comparing the experimental model of extrusion of blocks to eastern Asia (Tapponnier et al. 1982). In the left figure the rigid block has advanced 6.3 cm into plasticine.

The Tapponnier et al. (1982) experiment shows that one large left lateral fault forms and guides the extrusion. Increasing penetration of the indenter causes a second extrusion phase along a second major fault, which allows large displacement to the right. Numerous gaps similar to pull-apart basins along strike-slip faults open along the left lateral faults to the right.

As collision of India and Eurasia was earlier (~70 Ma; e.g., Yin and Harrison, 2000) than the formation of Bitlis Suture Zone (~11 Ma; e.g., Şengör and Yılmaz, 1981) we suggest that Turkey shows the early steps of this experiment (Figure 3.2). If we compare an earlier step of the Tapponnier et al. (1982) model to Turkey, many extensional features are missing. Although the model describes the development of the East and North Anatolian Fault systems, it fails to describe large-scale extension in western Turkey.

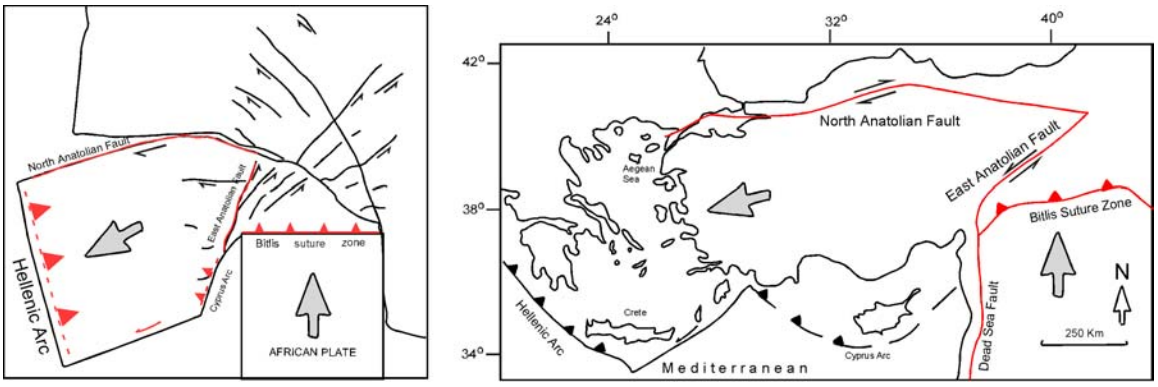

Figure 3.3 Comparing the Tapponnier et al. (1982) experimental model of extrusion of blocks to Turkey. In the left figure, a rigid block has advanced 3.5 cm into plasticine. Arrows show the location of the Menderes Massif in western Turkey and the direction of the movement of Anatolian plate.

In the back-arc spreading model, the migration of the Hellenic Arc trench system (Figure 3.4) to the south-southwest creates an extensional regime in the back-arc Aegean region (e.g., Le Pichon and Angelier, 1979; 1981; Meulenkamp et al. 1988; Buick, 1991;

Okay and Satır, 2000). Schellart et al. (2002) used an analogue model to explain asymmetric back-arc extension. The model consists of three layers confined in a 60 by 40 cm box. The top brittle layer is made of fine-grained glass microspheres, the high viscosity middle layer is made of silicone putty, simulating the viscous lower lithosphere in the nature. The lowermost viscous layer is made of glucose syrup. A rotational sidewall is used to simulate a subducting plate. Most of the deformation in the experiment is accommodated by normal faults, which show E-W trending extension (Figure 3.4).

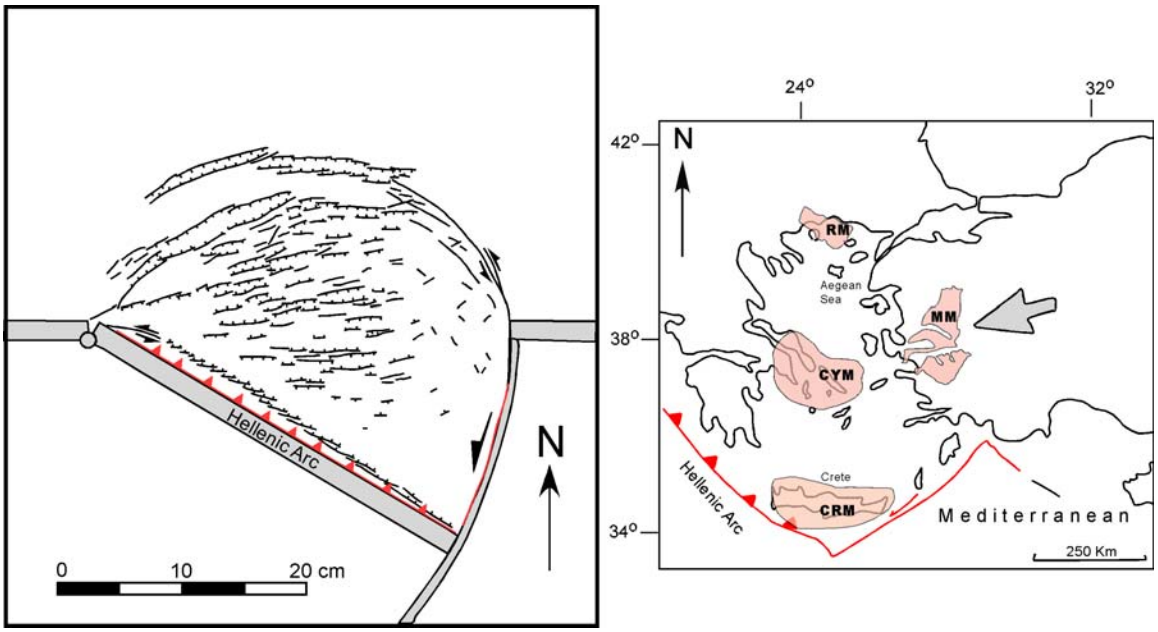

Figure 3.4 Comparing the Schellart et al. (2002) experimental model of back-arc spreading in block to Turkey. Abbreviations: CRM, Crete Massif, CYM, Cycladic Massif; MM, Menderes Massif; RM, Rhodop Massif.

The strike-slip fault between the Hellenic Arc and the Cyprus arc can be compared to the rotational sidewall in the Schellart et al. (2002) model, and the graben system can be used to describe the metamorphic core complexes seen in the Aegean

Region (Figure 3.4). However, the model predicts that a left-lateral strike-slip fault forms in western Turkey that is not observed.

In the orogenic collapse model, thickened and elevated continental crust due to Alpine orogeny extensionally collapses and thins (e.g., Berkhemer, 1977; Dewey, 1988; Seyitoglu and Scott, 1992; Jolivet et al. 1994; Seyitoglu and Scott, 1996; Bozkurt, 2001; Vanderhaeghe and Teyssier, 2001) (Figure 3.5). Metamorphic core complexes form in the hinterland of the collapsed orogenic belt. Note that in the cross-section of collapsed orogen, sedimentary basins and structures that were active while the middle crust of this orogen was partially molten and eventually exhumed.

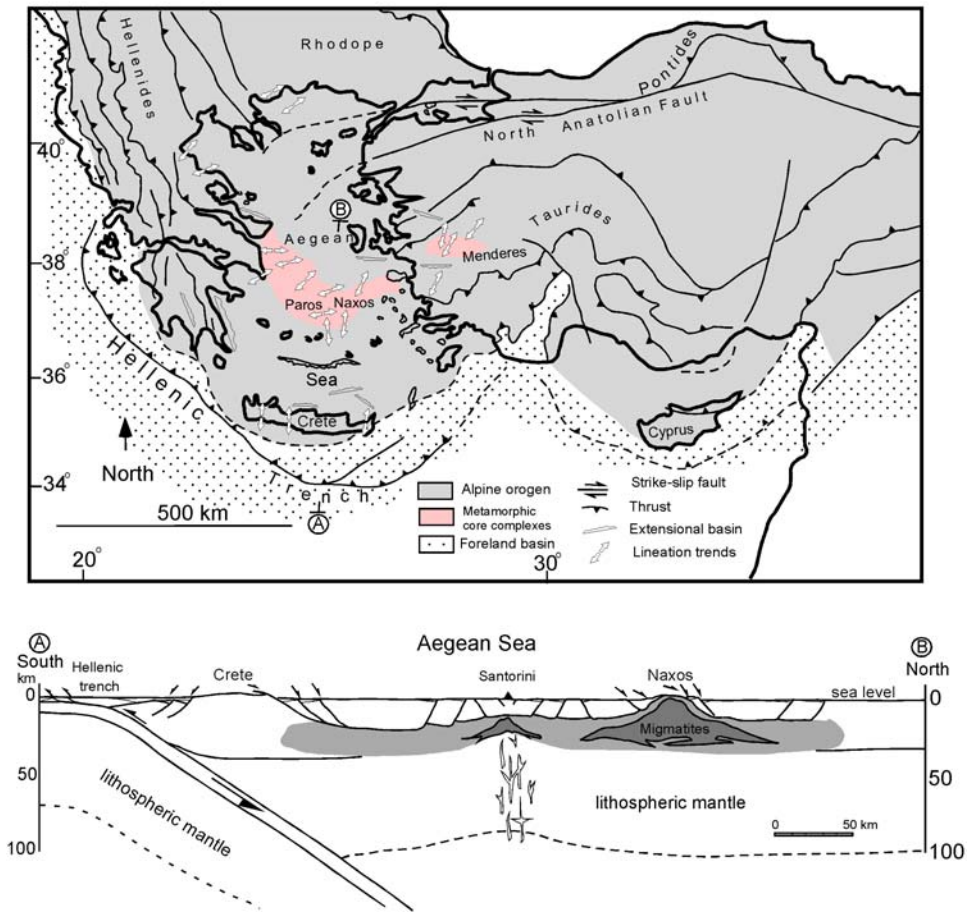

Figure 3.5 Orogenic collapse model (Vanderhaeghe and Teyssier, 2001)

Crustal thickening, suggested by the metamorphic record of the Aegean Sea rocks and in the continental part of the Hellenides, implies that collision and plate convergence played a key role during the evolution of Hellenides (Vanderhaeghe and Teyssier, 2001). The westward extrusion of Anatolian block contributed to the activation of large strike-slip faults in the north Aegean region. The observation of crustal thinning cannot be explained by compressive tectonic forces, gravity is required as an additional driving force. Most models of gravitational collapse of the Aegean crust invoke the role of slab roll-back and the creation of a free boundary along the Hellenic trench. It is difficult to demonstrate by geological means whether rollback is a cause or related to gravitational collapse. Vanderhaeghe and Teyssier (2001) have proposed that trigger for gravitational collapse of the Aegean crust is provided by weakening of the deep level of the orogenic crust related to partial melting which caused mechanical decoupling between the thickened crust and the subduction zone.

The thickness of the lithospheric mantle underneath the Aegean Sea is not well constrained by geophysical data. However, active magmatic arc, with active volcanism at the island of Santorini suggests the presence of a partially molten mantle source at depth between the Cyclades and Crete (Vanderhaeghe and Teyssier, 2001). Nevertheless, atmospheric upwelling at the scale of the Aegean Sea is unlikely. The continental crust flooring the Aegean Sea is 25-30 km thick and is essentially at sea level. Under these conditions, an increased mantle heat cannot explain high-temperature metamorphism and partial melting of the middle crust at the scale of the Aegean (Vanderhaeghe and Teyssier, 2001).

2. *The possibility of polymetamorphic garnet growth in the central Menderes Massif has implications on previous results produced by garnet-based thermobarometric methods*.

P-T conditions are used to evaluate models of the evolution of the Menderes Massif (Ashworth and Evirgen, 1984, 1985; Oberhaensli et al. 1997; Whitney and Dilek, 1997; Okay, 2001; Ring et al. 2001; Whitney and Bozkurt, 2002; Regnier et al. 2003; Rimmele et al. 2003). Microtectonic studies are useful for identifying pre-, inter-, syn-, and post-metamorphic garnet growth (e.g., Bozkurt, 1996; Passchier and Turow, 1996), and element mapping using electron microprobe provides conclusive evidence on the episodes of deformation that may have affected the central Menderes Massif.

Early studies in Menderes Massif have shown that there are relict eclogite- and blueschist-facies assemblages (Oberhaensli et al. 1997; Candan et al. 2001). High-pressure assemblages have been described in the central Menderes Massif (Candan et al. 1997; Oberhaensli et al. 1998; Okay, 2001), in the Lycian nappes (Oberhaensli et al. 2001) and in southern Menderes Massif (Dora et al. 2001; Whitney and Bozkurt, 2002).

Whitney and Bozkurt (2002) proposed that by using thermobarometric calculations from metasedimentary rocks they assess whether the metamorphic minerals contain evidence from more than one metamorphic event, as the rocks record at least two kinematically distinct episodes of deformation. Whitney and Bozkurt (2002) also used the results to evaluate tectonic models proposed for this region and suggest that, based on the petrographic or compositional characteristics of the minerals (e.g., garnet zoning), there is no evidence for more than one regional metamorphic event.

3. *P-T constraints and garnet X-ray element maps can be used to understand the role of the Massif in broader-scale reconstructions of the Tethyan suture.*

The mountain belts of Turkey are the result of repeated continental collisions that eventually welded together the two mega-continents Laurasia and Gondwana-Land (e.g., Şengör and Yılmaz, 1981). Since its formation, the internal geometry of the Tethyan domain has been characterized by complex plate boundary systems, which are composed of ridges, transforms, and subduction zones (Figure 3.6). Their record of activity is found in various states of preservation, mainly along the sutures of the Alpides, which are the sites of former Tethyan oceans (Şengör and Yılmaz, 1981).

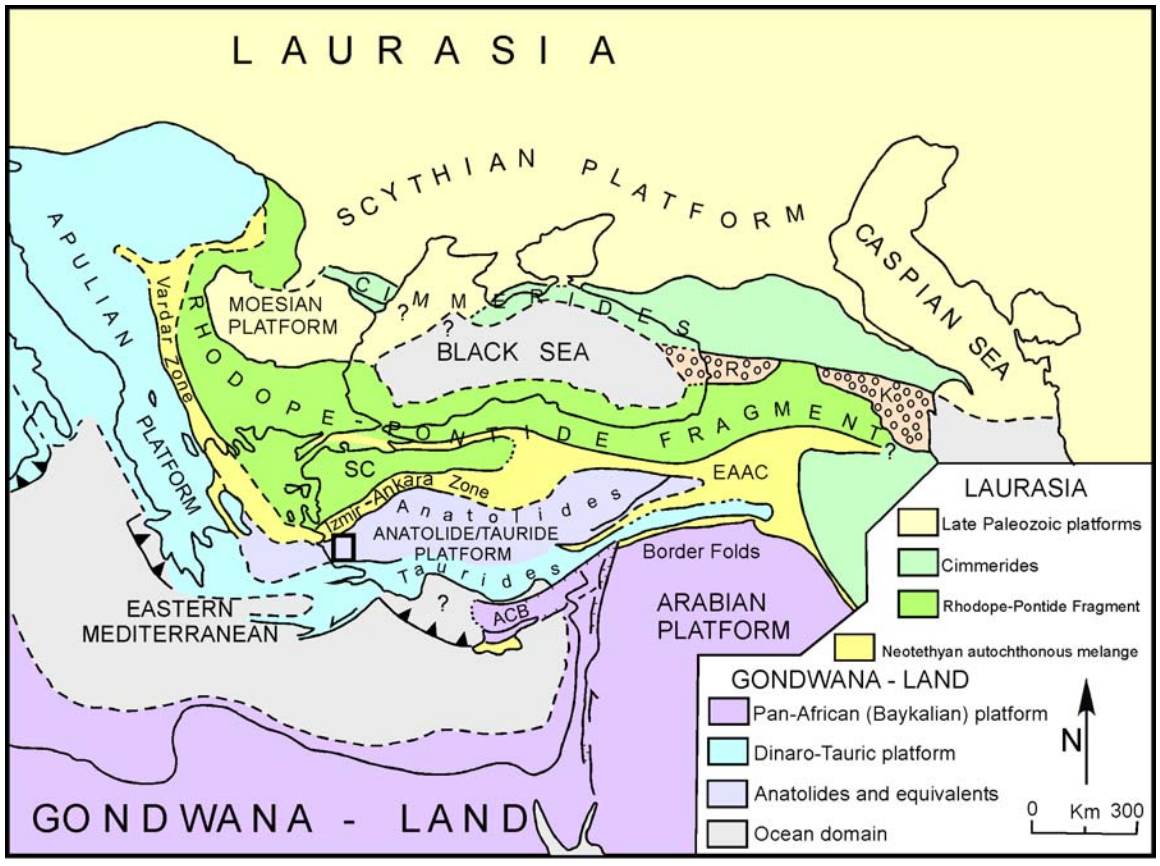

Figure 3.6 Tectonic setting of Turkey within the larger framework of the eastern Mediterranean Alpides (modified after Şengör and Yılmaz, 1981). Abbreviations, ACB, Adana-Cilicia Basin; EAAC, Eastern Anatolian Accretionary Complex, K, Khoura

depression; R, Riou depression; SC, Sakarya Continent. The square indicates the location of the Menderes Massif.

The Menderes Massif is a fundamental component of the Turkish orogen. The mountain ranges of Turkey are part of the eastern segment of the Mediterranean Alpides, where Tethyan deformation has been superimposed on rocks affected during the Pan African orogeny (e.g., Şengör and Yılmaz, 1981). The massif has a complex internal structure recording a multiphase deformation history and repeated metamorphism since the late Proterozoic (e.g., Dűrr, 1975; Şengör and Yılmaz, 1981). Numerous researchers have explored differences in the nature, style, and formation of the Menderes Massif (e.g., Dűrr, 1975; Le Pichon and Angelier, 1979; Şengör and Yılmaz, 1981; Ashworth and Evirgen, 1984, 1985; Seyitoglu and Scott, 1996b; Sözbilir and Emre, T., 1996; Ring et al. 1999, Gessner et al. 2001, Rimmele et al. 2003, Regnier et al. 2003). The first step in reconstructing the past configurations of continents and oceans is to identify the sutures with the help of P-T constraints and garnet X-ray element maps. This work will has implications for Aegean tectonics and the transition from compression to extension in orogens overall.

3.3 Discussion

The three fundamental models proposed for the development of the Menderes Massif indicate that the region is a key area for understanding the processes that control extension in the lithosphere. The goal of this thesis is to explore if the garnet-bearing rocks can be used constrain the P-T history of the range and further elucidate the mechanisms of extension in the range.

4. METHODS OF ANALYSIS

4.1. Introduction

Garnet is used as a chemical tape recorder in which the evolution of a sample is recorded by variations in Fe, Mg, Mn, Ca and Y (Pyle and Spear, 1999; Kohn and Spear, 2000). These zoned minerals hold a key to understanding the chemical reaction history of the Menderes Massif and its pressure – temperature (P-T) history. To obtain the P-T history, an electron microprobe is used. ConocoPhilips donated the Oklahoma State University JEOL733 electron microprobe to the university in 2002.

Electron microprobe analysis is a technique used to image and chemically analyze small selected areas of solid samples (see Reed, 1993, 1996; Klein, 2002 for reviews). In this method, X-rays and electrons are excited by a focused electron beam (e.g., Reed, 1996). The X-ray spectrum contains lines that are characteristic of the elements present in a mineral and qualitative analysis is possible by identifying the lines and their wavelengths, whereas the electrons are used to image the sample (e.g., Reed, 1996). The OSU electron microprobe uses EVEX software for qualitative analyses, imaging, and X-ray element mapping, and SAMX software for standardizing and obtaining compositions of minerals important for thermobarometry.

4.2. Sample Preparation

Garnet-bearing schists and gneisses were collected from three transects across the central Menderes Massif during the summer of 2003 (Figure 1.1; Table 4.1). Mineral assemblages were first identified and characterized in hand sample. Uncovered thin sections were made from all rocks collected by Vancouver Petrographics. A polarized optical microscope (Olympus BX51) was then used to identify minerals that could not be seen with a handlens and to identify rocks that had mineral assemblages ideally suited for thermobarometric calculations.

The ideal mineral assemblage for the thermobarometric part of this thesis is garnet + biotite + muscovite + plagioclase. Garnets chosen for thermobarometric analysis were euhedral to subhedral and not found in contact with minerals characteristic of significant retrogression (e.g., chlorite). Other minerals found in the rocks collected include: tourmaline, apatite, rutile, monazite, ilmenite, hematite and staurolite. Staurolite was only found in the units mapped as Precambrian by Konak (2002).

The selected thin sections were then cleaned in distilled water with high-purity ultrasonic cleanser (Buehler Ultramet 2 Sonic Cleaning Solution) and carbon coated using an EFFA MkII Carbon Coater.

Table 4.1 Mineral assemblages and locations of the rocks analyzed.[a]

Sample[b]	Northing	Easting	Assemblage [c]											
MM03			Upper Paleozoic Unit [c]											
			grt	bt	ms	plg	qtz	mz	rt	il	ap	hm	st	tr
33	586666	4237133	■	■	■	■	■	■	■	■				■
36	609173	4245427	■	■	■	■	■	■	■					
38	609480	4245905	■	■	■	■	■	■	■	■	■			
39	609490	4246007	■	■	■	■	■		■	■	■			
40	609863	4246174	■	■	■	■	■		■	■	■			
41	609868	4246181	■	■	■	■	■							
45	593931	4255450	■	■		■	■	■						
48	591002	4239955	■	■	■	■	■	■	■	■				
Paleozoic Units														
22	616900	4244965	■	■	■	■	■		■		■			
23	616890	4244972	■	■	■	■	■		■		■			■
32	616928	4245256	■	■	■	■	■	■	■		■			■
Precambrian Units														
26	616403	4245187	■		■		■	■		■	■	■	■	■
27	616405	4245186	■		■		■		■	■	■		■	
28	616408	4245182	■		■		■	■	■	■	■	■	■	

a. See Figure 1.1 for sample locations. Major minerals were identified in hand sample and using a petrographic microscope and an electron microprobe.

b. Sample names are referred to as MM03-# in the text.

c. Filled areas indicate the mineral is found in the sample. Abbreviations: grt = garnet, bt = biotite, ms = muscovite, plg = plagioclase, qtz = quartz, mz = monazite, rt = rutile, il = ilmenite, ap = apatite, hm = hematite, st = staurolite and tr = tourmaline.

d. Age of units provided by Konak (2002).

4.3. Electron Microprobe Analytical Methods

4.3.1. Imaging

Two major types of images are produced by the electron microprobe: secondary electron images (SEI) and backscattered electron images (BSE). SEI images are generated when the electron beam excites electrons from the outermost shell of an atom, and are typically used to show topography (e.g., Reed, 1996). These types of images were not used in this study.

In BSE images, contrast depends on the variation in the number of electrons emitted from the point of impact of the beam on the surface of the specimen (e.g., Reed, 1996). The fraction of incident electrons that backscattered depends on atomic number. A detector sensitive to backscattered electrons produces images showing differences in average atomic number. Minerals that contain elements of different atomic numbers show different brightness in the grayscale BSE image (Figure 4.1 and 4.2). This brightness difference is key for helping to identify what minerals are present. For example in Figure 4.1, ilmenite ($FeTiO_3$, highest atomic number = 81) are brighter compared to garnet ($Fe_3Al_2(SiO_4)_3$, highest atomic number = 26) (Figure 4.1), whereas quartz (SiO_2, highest atomic number = 14) are the darkest grains in the images.

The imaging capability is one of the most useful aspects of the electron microprobe. Rock thin sections can be scanned to find suitable minerals for chemical analyses and to photograph minerals and inclusions that are too small to be seen with a regular petrographic microscope. For example, in Figure 4.1 monazite inclusions are ~20 μm. These minerals appear as bright inclusions in the garnet but are impossible to see with a petrographic microscope.

BSE images of rocks can also be used to evaluate the history of the sample. For example, in Figure 4.1, the garnet is subhderal and contains scattered inclusions that are generally similar in size. In Figure 4.2, the garnet is also subhedral, but the inclusions are located within specific domains (rim and mid-rim area). These observations suggest that these garnets formed in different environments.

BSE images are also useful for qualitatively identifying suitable minerals for chemical analysis and thermobarometry. The phyllosilicates, such as biotite, muscovite, and chlorite typically appear as elongated sheets, whereas the framework silicates, like quartz and feldspar are generally seen as anhedral grains. Quartz and felsdspar are difficult to distinguish due to their similarity in contrast in BSE images and chemical analyses were required to identify them. However, the orthosilicates, like garnet and staurolite, typically appear as large porphyoblasts and are easily seen (Figure 4.1 and.2).

Note that for imaging in this thesis, the electron microprobe operated using an accelerating voltage of 15 kV and a beam current of 15-20 nA.

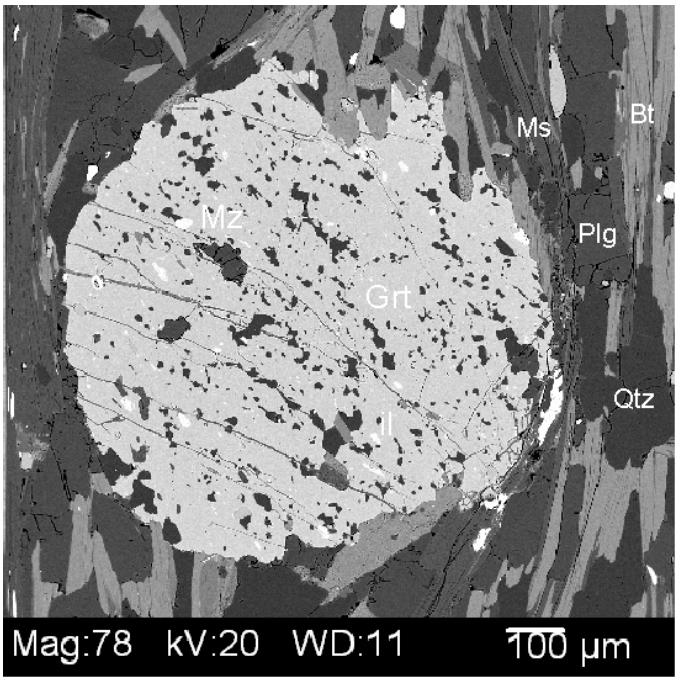

Figure 4.1 BSE image of sample MM03-33. The big grain in the center is garnet (Grt). It is surrounded by quartz (Qtz), plagioclase (Plg), muscovite (Ms) and biotite (Bt). Garnet contains monazite (Mz) and ilmenite (Il) inclusions.

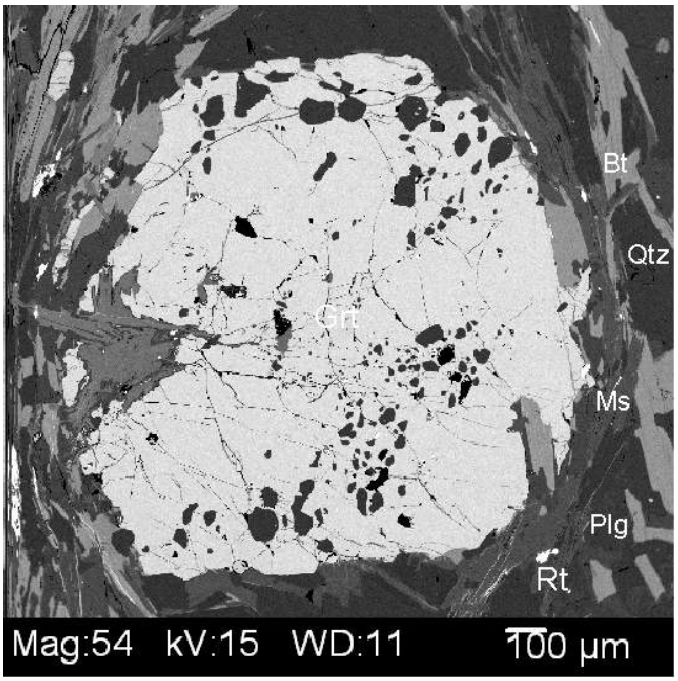

Figure 4.2 BSE image of the sample MM03-23. Garnet (Grt) is surrounded by quartz (Qtz), plagioclase feldspar (Plg), muscovite (Ms) and biotite (Bt). This sample contains rutile (Rt) in the matrix.

4.3.2. X-Ray Element Mapping

Garnet has a chemical formula of $A_3B_2(SiO_4)_3$ where the *A*-sites contain Mg, Fe, Mn or Ca and the *B*-sites contain Al, Fe, or Cr. The most abundant garnets are pyrope [$Mg_3Al_2(SiO_4)_3$], almandine [$Fe_3Al_2(SiO_4)_3$], spessartine [$Mn_3Al_2(SiO_4)_3$] and grossular [$Ca_3Al_2(SiO_4)_3$] (Johnsen, 2002). An important step prior to acquiring quantitative data for thermobarometry is identifying how elements within the garnet are distributed. This process is done by X-ray element mapping

To obtain the X-ray element map, an Energy Dispersive Spectrometer (EDS) collects an X-ray spectrum and energy bands containing the peaks of elements of interest are defined (e.g., Reed, 1996). For example, Figures 4.3 and 4.4 show EDS spectra of garnets that differ in composition. Each peak in the spectra corresponds to a specific X-ray emitted from an element in the garnets. Peak heights in EDS spectra indicate the relative concentrations of the elements. Figure 4.3 was collected from an almandine garnet (18.09% Fe, 6.45% Mg), whereas Figure 4.4 was obtained from a pyrope garnet (8.67% Fe, 11.66% Mg). Note that the Mg peak is higher in the pyrope garnet, the Fe peak is higher in the almandine garnet.

In this thesis, garnets and the surrounding areas were X-ray element mapped in Fe, Mg, Mn, Ca, Al, K, Na and Si for compositional traverses and compositional analyses. These maps were then converted in colors using EVEX software. Note that the conditions for X-ray element mapping are an accelerating voltage of 20 kV, a beam current of 15 nA and a run time of approximately 12 hours.

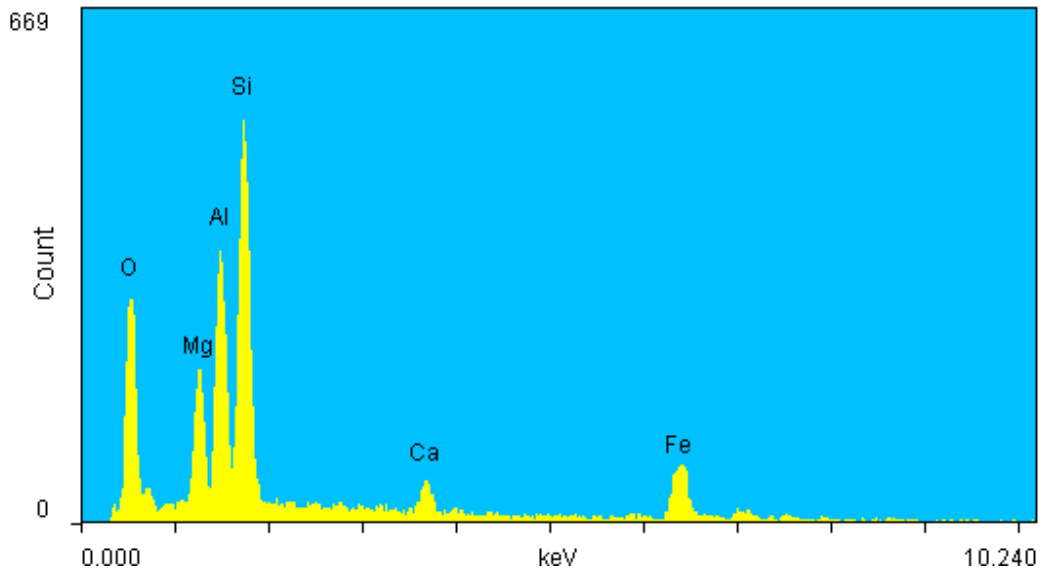

Figure 4.3 EDS spectrum of almandine garnet (SPI Mineral Standard Block #02753-AB).

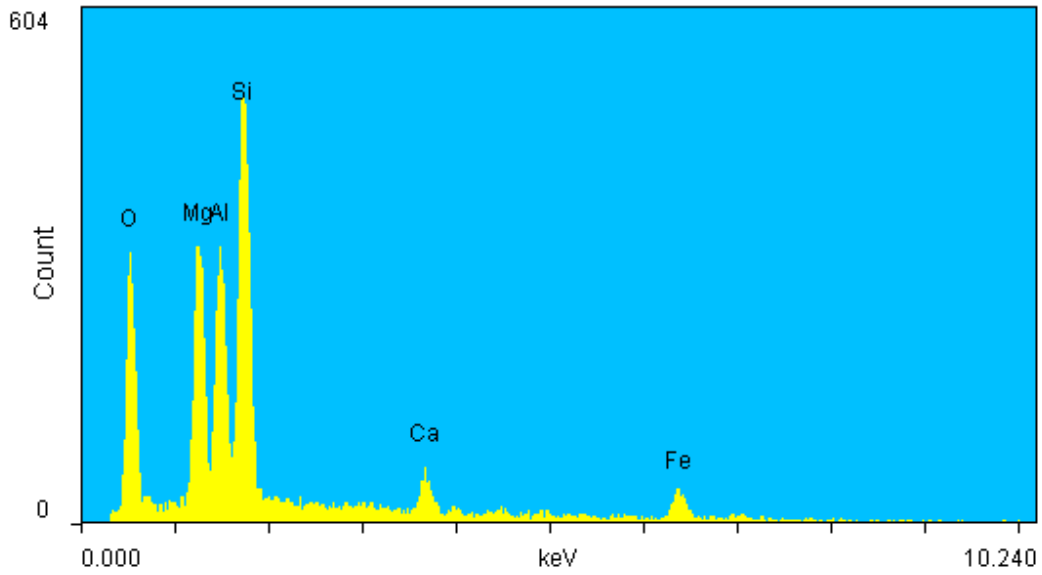

Figure 4.4 EDS spectrum of pyrope garnet (SPI Mineral Standard Block #02753-AB).

Slow diffusion of major elements (Mn, Ca, Fe, and Mg) in garnet results in compositional zonations, which can be used to unravel metamorphic events (Spear, 1993). Prograde garnets that grow during an increase in temperature can show characteristic "bell-shaped" growth zoning profiles, with concentrations of Mn and Fe/(Fe+Mg) that are high in the core and decreasing toward the rim (Figure 4.5A) (e.g., Spear, 1993). However, an increase in Fe/(Fe+Mg) content at a garnet rim indicates a retrograde ion exchange of Fe-Mg with minerals adjacent to the garnet (e.g., biotite or chlorite), enriching these nearby minerals in Mg (Kohn and Spear, 2000). Garnets that have experienced retrograde dissolution can be identified by sharp increases in Mn and Fe/(Fe+Mg) concentrations at their rims (Figure 4.5B).

Polymetamorphic garnets can be identified by Mn concentrations and Fe/(Fe+Mg) that deviate from these two characteristic zoning profiles. For example, Figure 4.5C shows a polymetamorphic profile in which the Mn concentration and Fe/(Fe+Mg) are high in the core and decreasing toward the rim and increasing again in the rim and stays constant.

The P-T results in this study were estimated using the lowest Mn and Fe/(Fe+Mg) values from the garnet rims (e.g., Spear and Peacock, 1989). Choice of this composition is key for obtaining realistic conditions experienced by the rock. Arrows in Figure 4.5 show the locations of these compositions along schematic garnet traverses. For prograde garnets, the composition at the very edge of a garnet rim is used for P-T calculations. For retrograde garnets, this position is located within the garnet rim.

However, in polymetamorphic garnets, the lowest Mn and Fe/(Fe+Mg) values may not be a useful composition to obtain realistic P-T conditions. Polymetamorphic

garnets may show variations in Mn and Fe/(Fe+Mg) values throughout the grain, thus the location of the composition for P-T calculations may not be readily identifiable. In Figure 4.5C, the composition at the very edge of the garnet is chosen because this may be the closest to equilibrium with matrix minerals.

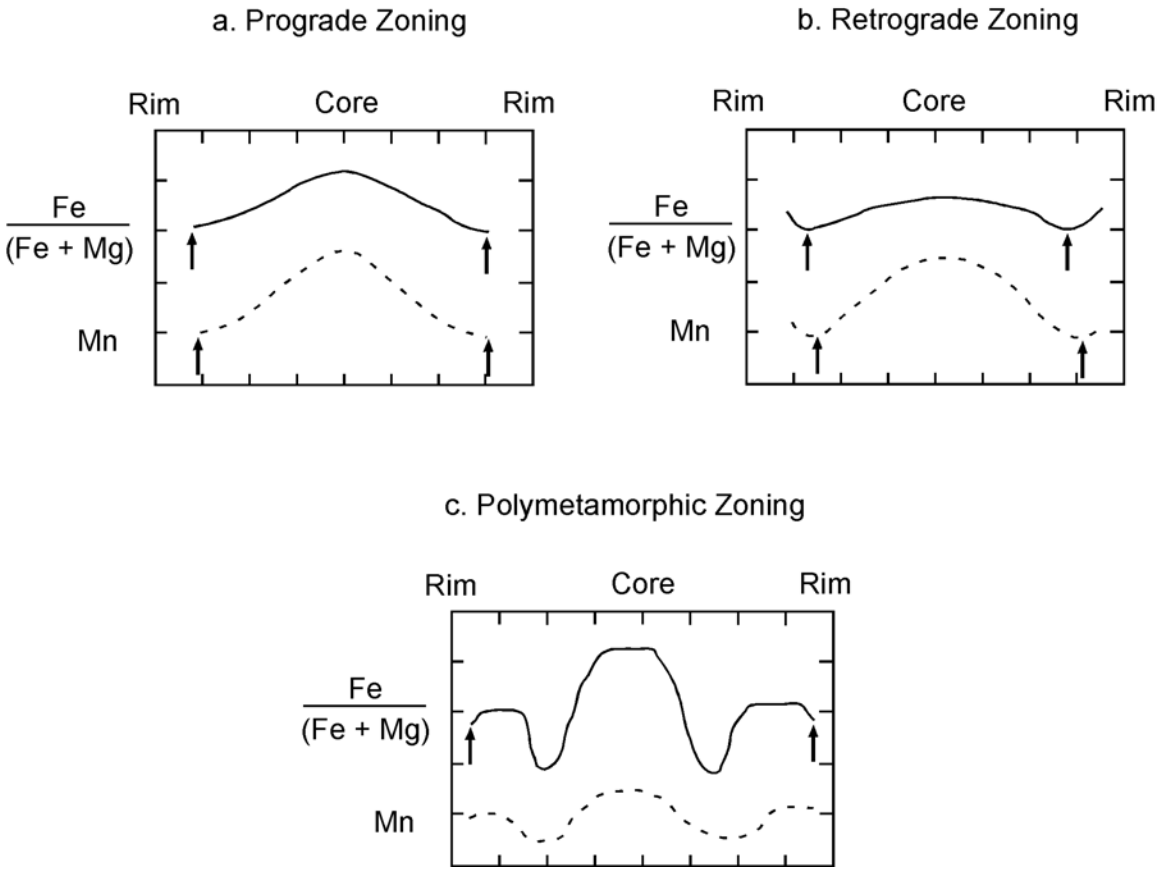

Figure 4.5 Schematic compositional traverses across a garnet from rim to rim, showing (A) prograde zoning, (B) retrograde zoning and (C) polymetamorphic zoning. Arrows show the places where the compositions for peak P-T conditions are obtained.

4.3.3. Chemical Analyses

To obtain chemical analyses, the intensities of the relevant X-ray lines generated in the specimen and in suitable standards are measured. The relationship between the intensity of an X-ray line and concentration of the element concerned depends on the composition of the sample (see Figures 4.3 and 4.4). Element concentrations are calculated from the ratios of specimen and standard intensities and the known concentrations in the standards (e.g., Reed, 1996).

An accelerating voltage of 15 kV and a beam current of 15 nA were used for both standardizing and analyzing. Wavelength Dispersive Spectrometers (WDS) are used for chemical analyses. WDS crystals (LIF, PET, and TAP) were chosen for suitable elements (Table 4.2). Matrix corrections are used to convert specimen to standard intensity ratios into concentrations (e.g., Reed, 1993). All raw data is reduced using the PAP matrix correction, which corrects for absorption, fluorescence, backscattering which could affect the compositional results (e.g., Reed, 1993).

Table 4.2 shows the standards used for the quantitative electron microprobe analysis. Oxygen was not measured and was calculated by stoichiometry (e.g., Deer et al. 1992). Multiple analyses were sometimes performed on single spots to check for consistent results. The results were then used in thermobarometric calculations to obtain P-T conditions.

Table 4.2 Standards for quantitative electron microprobe analysis.[a]

Mineral Name	Mineral Formula	Element	Crystal used	Crystal position
Chromium Oxide	Cr_2O_3 (Synthetic)	Cr	LIF	159.175
Diopside	$MgCaSi_2O_6$	Si	TAP	77.385
Diopside	$MgCaSi_2O_6$	Ca	PET	107.600
Magnetite	Fe_3O_4	Fe	LIF	134.515
Jadeite	$NaAlSi_2O_6$	Na	TAP	129.280
Pyrope Garnet	$Mg_3Al_2Si_3O_{12}$	Mg	TAP	107.320
Rhodonite	$MnSiO_3$	Mn	LIF	146.075
Rutile	TiO_2	Ti	PET	88.090
Sanidine	$KAlSi_3O_8$	K	PET	119.865
Spodumene	$LiAlSi_2O_6$	Al	TAP	90.520

a. Standards are from SPI supplies #02753-AB

4.4. Thermobarometric methods

Thermobarometry is based on well-known properties of equilibrium exchange of cations between garnet and matrix minerals under varying P-T conditions (e.g., Spear, 1993, Gilley 2001). In each sample, garnet porphyroblasts were analyzed along rim-core-rim and rim-core traverses at 20 μm intervals to obtain quantitative chemical zoning profiles (Spear and Peacock, 1989). The compositions of biotite, muscovite, and plagioclase were also measured for thermobarometry. As explained before, the P-T conditions were estimated from the garnet rim (lowest Mn and Fe/(Fe+Mg) values) and matrix minerals adjacent to the garnet. Peak T estimates were obtained using the garnet-biotite thermometer (Ferry and Spear, 1978; Berman, 1990) and peak P were estimated using the garnet-muscovite-biotite-plagioclase barometer (Hoisch, 1990).

Many geothermometers are based on cation exchange reactions, typically between Fe and Mg. These include garnet-biotite, garnet-cordierite, garnet-hornblende, garnet-chlorite, garnet-orthopyroxene, garnet-clinopyroxene, garnet-olivine, garnet-phengite,

garnet-ilmenite, and biotite-tourmaline (Spear and Peacock, 1989). In this study the rock assemblages are more suitable for the garnet-biotite thermometer.

The garnet-biotite thermometer is based on the exchange between Fe and Mg between the coexisting silicates as seen in the following reaction (Ferry and Spear, 1978):

Fe-rich garnet + Mg-rich biotite → Mg-rich garnet + Fe-rich biotite

Almandine + Phlogopite → Pyrope + Annite

$Fe_3Al_2Si_3O_{12} + KMg_3AlSi_3O_{10}(OH)_2 \rightarrow Mg_3Al_2Si_3O_{12} + KFe_3AlSi_3O_{10}(OH)_2$

The equilibrium constant (K_{eq}) for exchange reactions can be simplified as a ratio of the exchanging cations in one phase divided by the same ratio in the second phase. This formulation is defined as the distribution coefficient ($K_D = \{Fe/Mg\}_A / \{Fe/Mg\}_B$). K_{eq} can be regressed as a function of the temperature and pressure of the equilibration, from which values of standard state enthalpy (ΔH) and entropy of reaction (ΔS) and in some cases the volume of the reaction (ΔV) of reaction are derived (Spear and Peacock, 1989; Spear, 1993). Exchange reactions generally have a small ΔV with moderate ΔS and ΔH so that the K_{eq} isopleth has a relatively shallower slope (Figure 4.6).

Many net transfer equilibria make excellent geobarometers because they have reasonably large volume changes. One way to balance the transfer of Ca from grossular to anorthite is with muscovite and biotite. The garnet-plagioclase-muscovite-biotite barometer is based on this reaction (Hoisch, 1990):

Fe-rich garnet + Ca-rich garnet + muscovite ↔ Ca-rich plagioclase + Fe-rich biotite

Almandine + Grossular + Muscovite ↔ Anorthite + Annite

$Fe_3Al_2Si_3O_{12} + Ca_3Al_2Si_3O_{12} + KAl_3Si_3O_{10}(OH)_2 \leftrightarrow 3\ CaAl_2Si_2O_8 + KFe_3AlSi_3O_{10}(OH)_2$

In contrast to the exchange reactions, net exchange reactions have larger ΔV values, which results in steeper slopes of K_{eq} in P-T space (e.g., Spear and Peacock, 1989; Spear, 1993). This geobarometer was chosen due to the mineral assemblage of the rocks that are studied.

In this study, K_{eq} lines were calculated using the software *Thermobarometry v 2.1* (Spear and Kohn, 1999), and the equilibrium determined for each sample was plotted together in P-T space (see Figures in Chapter 5 for P-T plots).

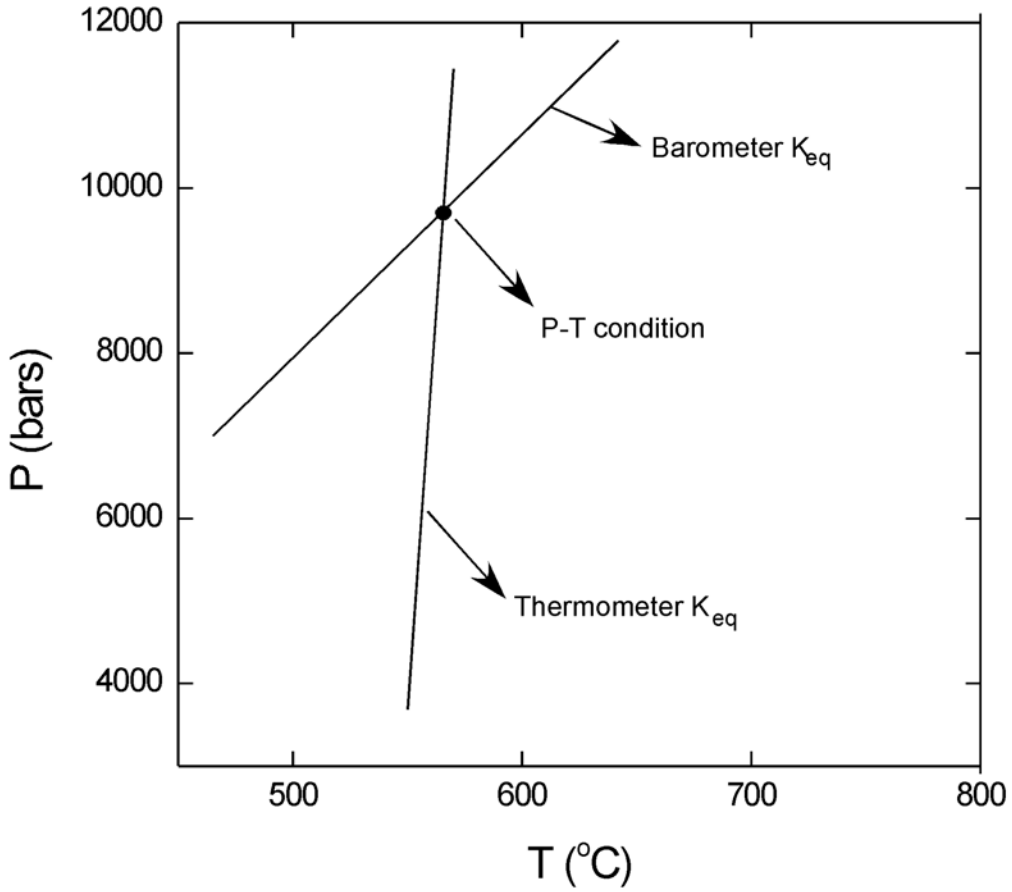

Figure 4.6 An example of P-T lines calculated from thermobarometric expressions using compositional data. The shallower line represents the equilibrium constant (K_{eq}) for the garnet-biotite exchange reaction (Ferry and Spear, 1978) and the steeper line represents the equilibrium constant (K_{eq}) for geobarometric expressions (Hoisch, 1990). The point at which these two lines intersect is the peak P-T condition experienced by the rock.

5. RESULTS AND CONCLUSIONS

5.1 Introduction

This chapter presents new thermobarometric data from the rocks collected from rocks adjacent to Kuzey detachment in central Menderes Massif (Figure 1.2). This area was the site of earlier studies of garnet-based thermobarometry (e.g., Ashworth and Evirgen, 1984, 1985; Oberhaensli et al. 2001; Whitney and Bozkurt, 2002; Regnier et al. 2003; Rimmele et al. 2003). The goal of this study is to establish the P-T histories of the central Menderes Massif as a means to identify if garnets record a polymetamorphic history.

Garnet-bearing assemblages were sampled adjacent to Kuzey detachment in Alasehir Graben (Figure 5.1). See Figure 2.1 for an overview of the regional geology of the Menderes Massif. Samples were collected from the hanging wall schist and gneiss units, whereas sediments make up the footwall rocks of the Kuzey detachment (Seyitoglu et al. 2002; Konak, 2002). Garnets from the three transect (Figure 5.1) differ in compositional zoning of Mn, Ca, Mg, and Fe. X-ray element maps collected from the samples using an electron microprobe show that the Menderes Massif is comprised of prograde and retrograde garnets. P-T data show that the rocks experienced high-grade metamorphic conditions, from 505±55°C to 715±55°C, and 8.9±2.3 kbar to 11.4±1.6 kbar. Results from adjacent samples are sometimes inconsistent, indicating that garnets may have grown in response to different events, thus recording a polymetamorphic history.

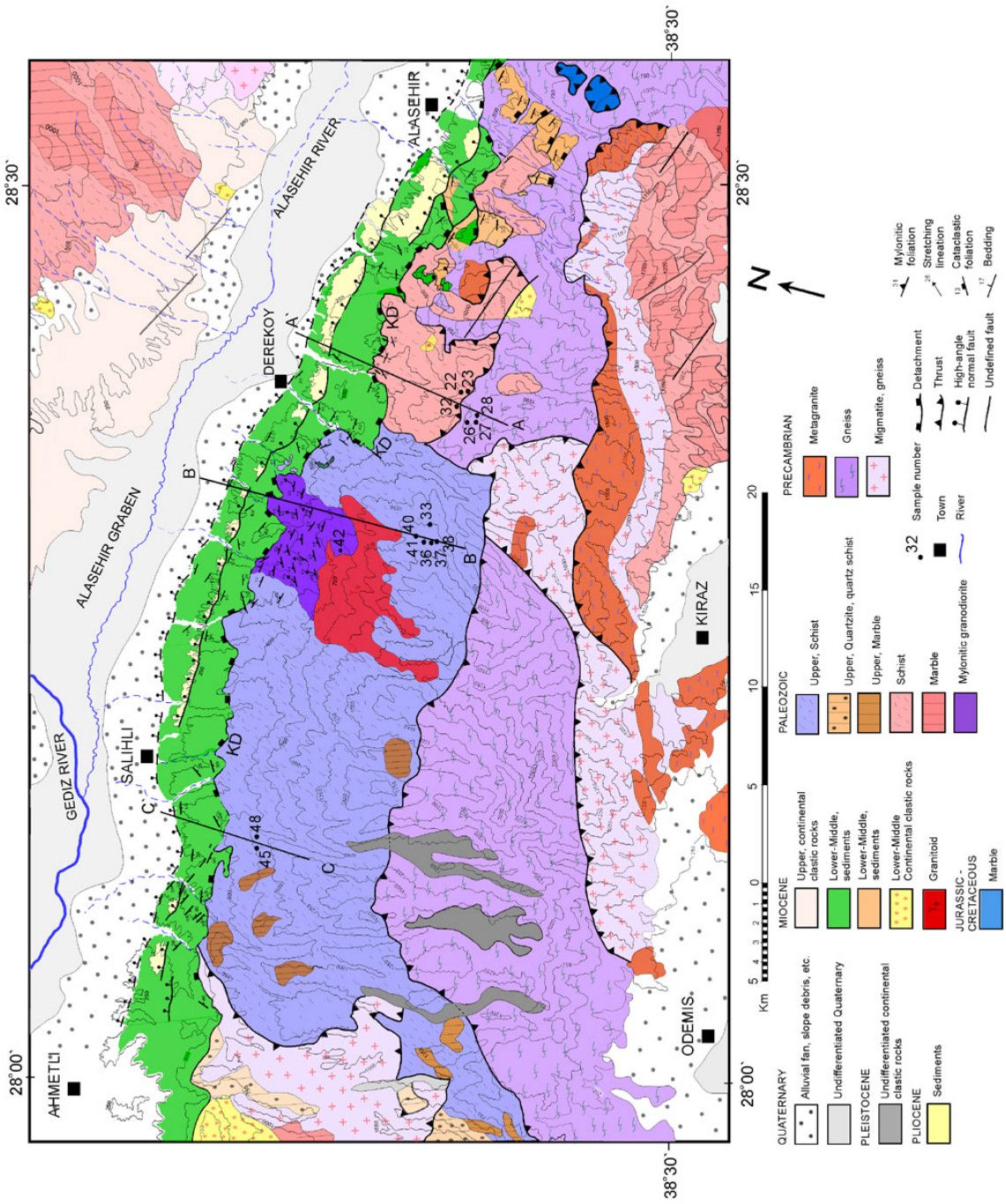

Figure 5.1 Sample location map (modified after Konak, 2002; Seyitoglu et al. 2002; Işık et al. 2003). Abbreviations: KD, Kuzey Detachment.

5.2 Thermobarometric results

X-ray element maps of Menderes Massif garnets show differences in zoning of Mn, Ca, Fe and Mg. A summary of the compositional zoning character of the garnets is indicated in Table 5.1. To evaluate these differences in zoning and P-T conditions experienced by the rocks, the samples are divided according to transects they were collected from.

Table 5.1 Summary of the zoning characteristics of the Menderes Massif samples.

Sample (MM03-#)	Mn		Ca		Mg		Fe		zoning type
				Transect A-A'					
	C[a]	R[a]	C	R	C	R	C	R	
22[b]	high[c]	low[c]	high	low	flat[c]		high	low	prograde
23[b]	high	low	high	low	low	high	low	high	prograde
26[b]	flat		flat		low	high	flat		retrograde
27[b]	flat		flat		low	high	flat		retrograde
28[b]	flat		flat		flat		flat		retrograde
32[b]	flat		flat		high	low	high	low	retrograde
32[b]	flat		flat		flat		flat		
				Transect B-B'					
33[b]	low	high	flat		flat		low	high	retrograde
36	flat		flat		high	low	flat		retrograde
37	low	high	high	low	low	high	low	High	retrograde
38[b]	flat		flat		flat		flat		retrograde
40	flat		low	high	flat		flat		retrograde
41	flat		high	low	flat		flat		retrograde
				Transect C-C'					
45	high	low	flat		flat		flat		prograde
48[b]	high	low	high	low	low	high	low	high	prograde

a. Abbreviations "C", Core, "R", Rim, Note that more than one garnet was mapped in sample MM03-32.
b. Indicates a compositional traverse was made across this garnet.
c. "High", "low", and "flat" are qualitative interpretations based only on observations of the X-ray element maps.

5.2.1 Transect A-A'

Samples MM03-22 through MM03-32 were collected along transect A-A' (Figure 5.2). Only samples MM03-22, MM03-23, MM03-26, MM03-27, MM03-28, and MM03-

32 contain garnet (Table 4.1) and are identified on the cross section. Field photos show the outcrops where those samples were collected (Figure 5.3).

Along transect A-A', garnets in samples MM03-22 and MM03-23 are interpreted to have prograde zoning (Table 5.1). X-ray element maps of MM03-22 and MM03-23 garnets have high Mn cores and lower Mn concentrations towards the rim, consistent with compositional preservation and prograde garnet growth (Figure 5.4 and 5.5). Garnets from both samples show similar Ca zoning with higher Ca cores and lower Ca rims. However, Fe and Mg zoning in these samples differ significantly. The MM03-22 garnet has a high Fe core and flat Mg zoning, whereas the MM03-23 garnet has a low Fe core and Mg increases towards the rim. Overall, these qualitative observations suggest that these samples grew under similar baric conditions, but different thermal conditions.

Garnets in samples MM03-26, MM03-27, MM03-28, and MM03-32 appear retrograde. X-ray element maps of garnets from these samples (Figures 5.6-5.9) show flat zoning in Mn and Ca, consistent with diffusional homogenization. Two garnets were element mapped from sample MM03-32, which was collected from the Paleozoic schist unit; one garnet has a higher Mg and Fe core and lower concentrations in the rim, whereas another garnet shows flat zoning in these elements (Table 5.1; Figure 5.9).

Samples MM03-26, MM03-27, and MM03-28 were collected within 50m of each other. All garnets from these samples show flat Fe zoning, but different Mg zoning. Garnets from MM03-26 and MM03-27 have low Mg cores and high Mg rims, whereas MM03-28 has flat Mg zoning. Again, qualitative observations of the X-ray element maps suggest these rocks experienced different metamorphic histories.

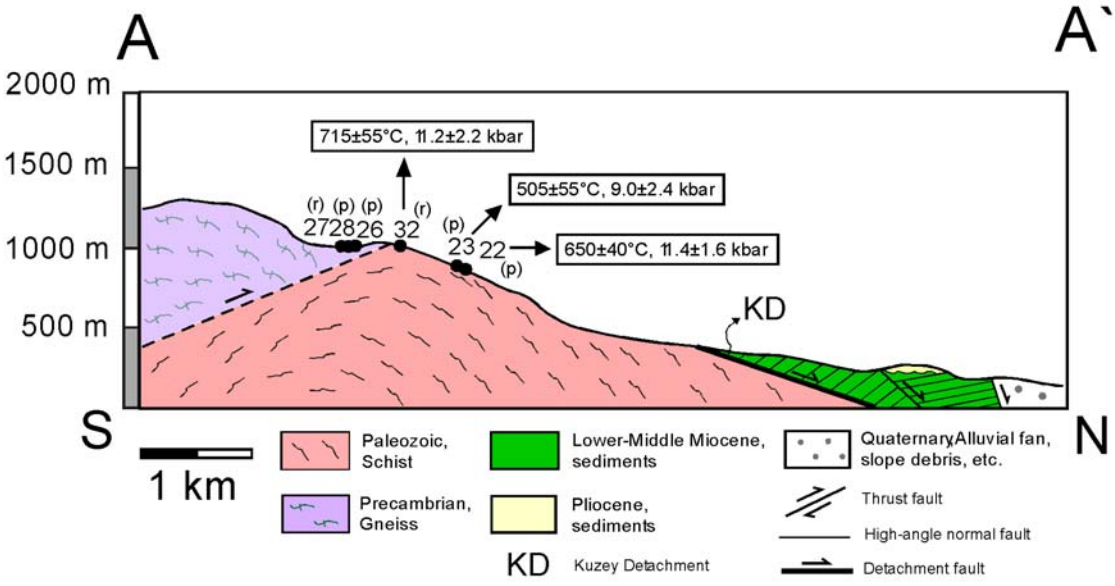

Figure 5.2 Transect A-A' showing the locations of the samples and P-T data. See Figures 5.4 to 5.8 for garnet X-ray element maps and Figures 5.10, 5.12, and 5.14 for garnet traverses. Abbreviations: (p) prograde zoning, (r) retrograde zoning.

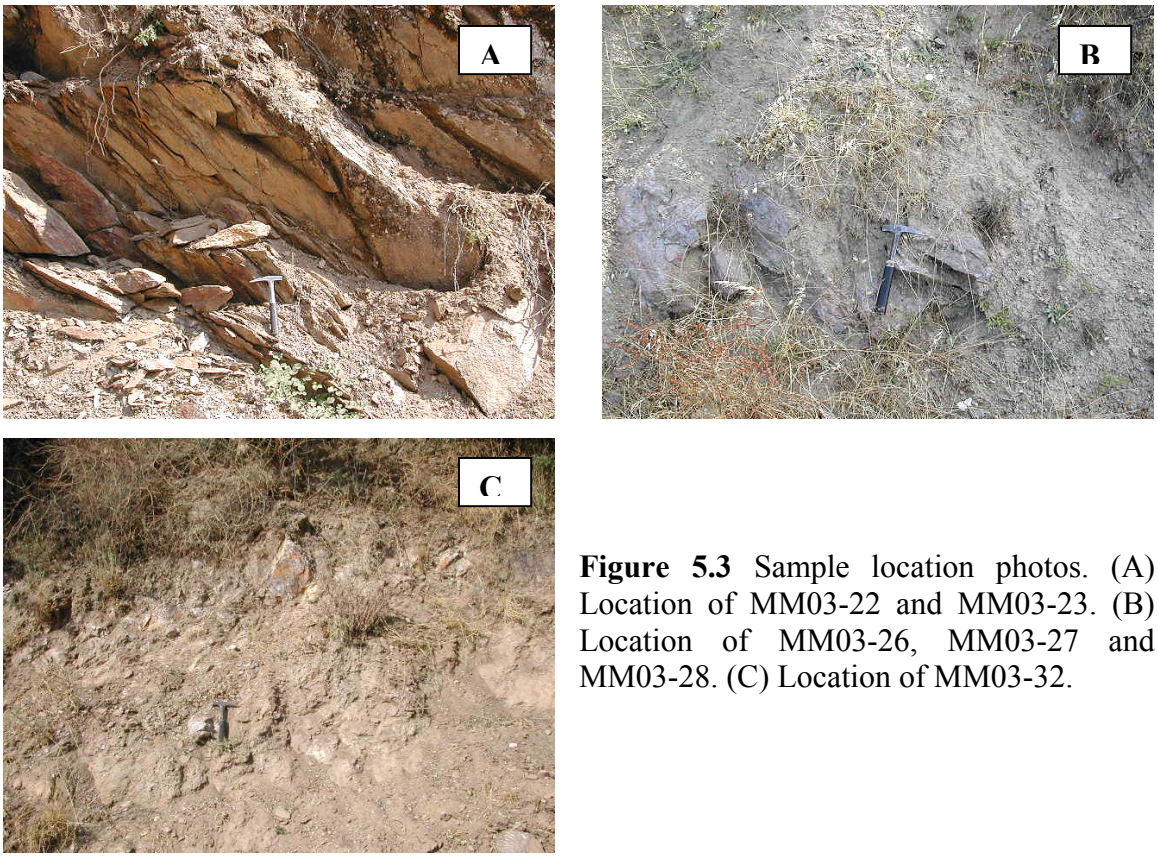

Figure 5.3 Sample location photos. (A) Location of MM03-22 and MM03-23. (B) Location of MM03-26, MM03-27 and MM03-28. (C) Location of MM03-32.

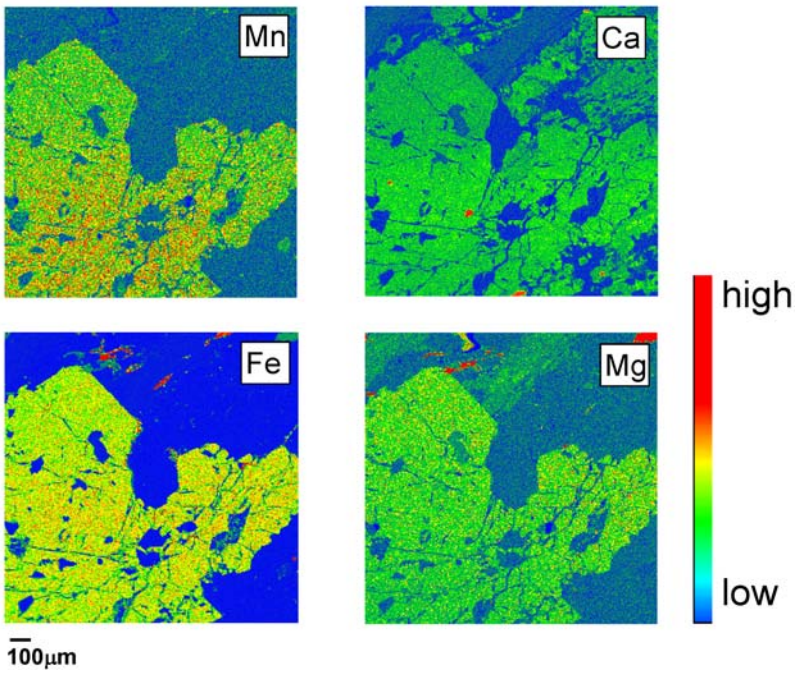

Figure 5.4 X-ray element maps of Mn, Ca, Fe, and Mg of garnet from MM03-22. See Figure 5.11 for a BSE image of this sample and Figure 5.10 for a compositional traverse across this garnet.

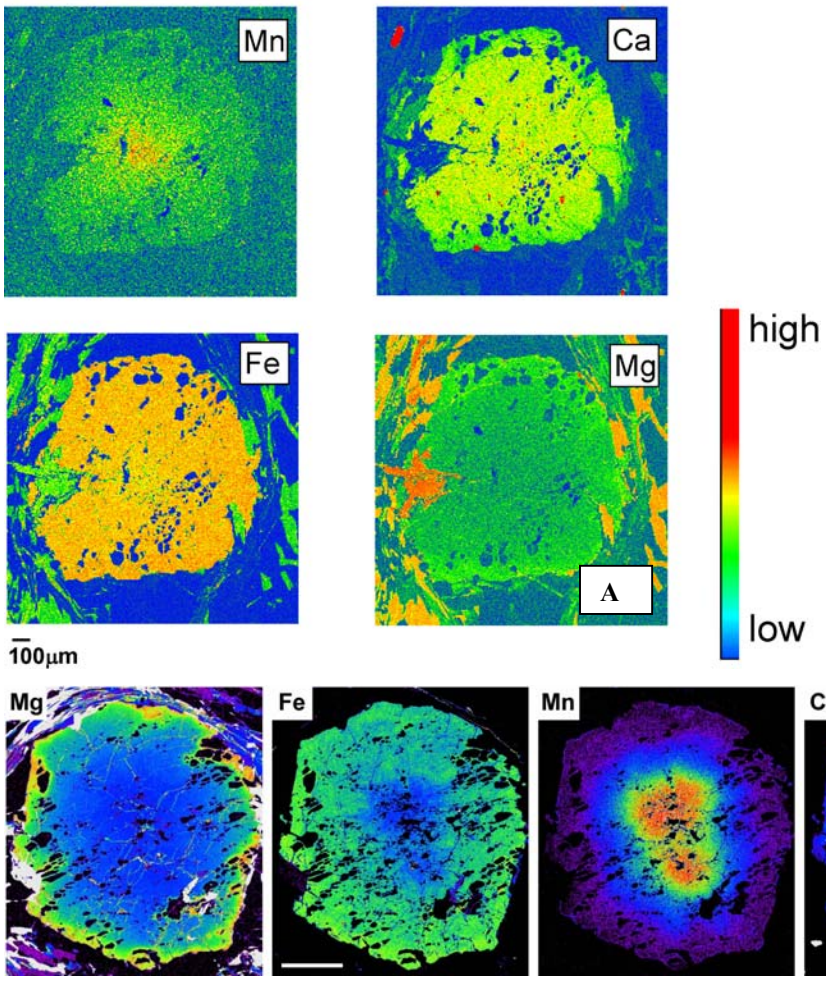

Figure 5.5 X-ray element maps of Mn, Ca, Fe, and Mg of garnets from MM03-23. Lower map collected by Dr. M. Kohn, University of South Carolina. See Figure 5.11 for a BSE image of this sample and Figure 5.10 for a compositional traverse across this garnet.

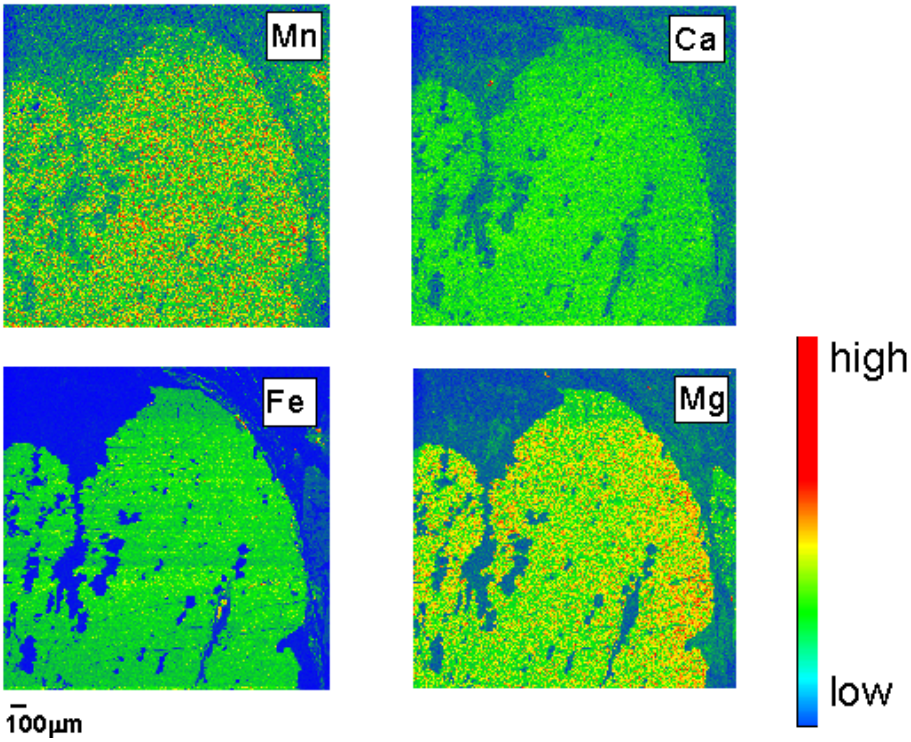

Figure 5.6 X-ray element maps of Mn, Ca, Fe, and Mg of a garnet from MM03-26. See Figure 5.13 for a BSE image of this sample and Figure 5.12 for a compositional traverse across this garnet.

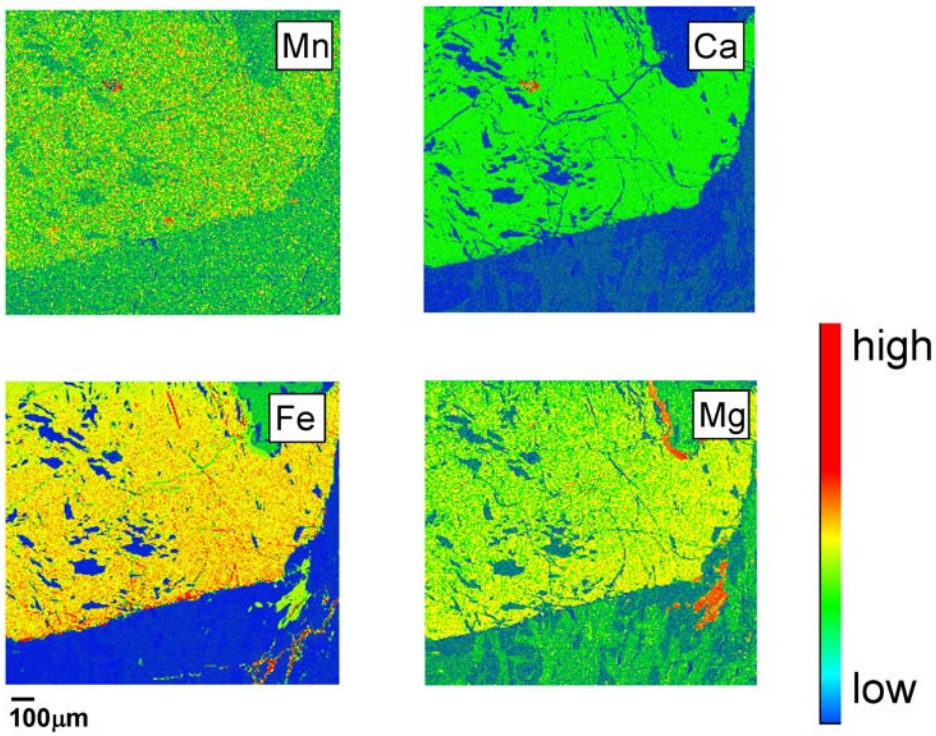

Figure 5.7 X-ray element maps of Mn, Ca, Fe, and Mg of a garnet from MM03-27. See Figure 5.13 for a BSE image of this sample and Figure 5.12 for a compositional traverse across this garnet.

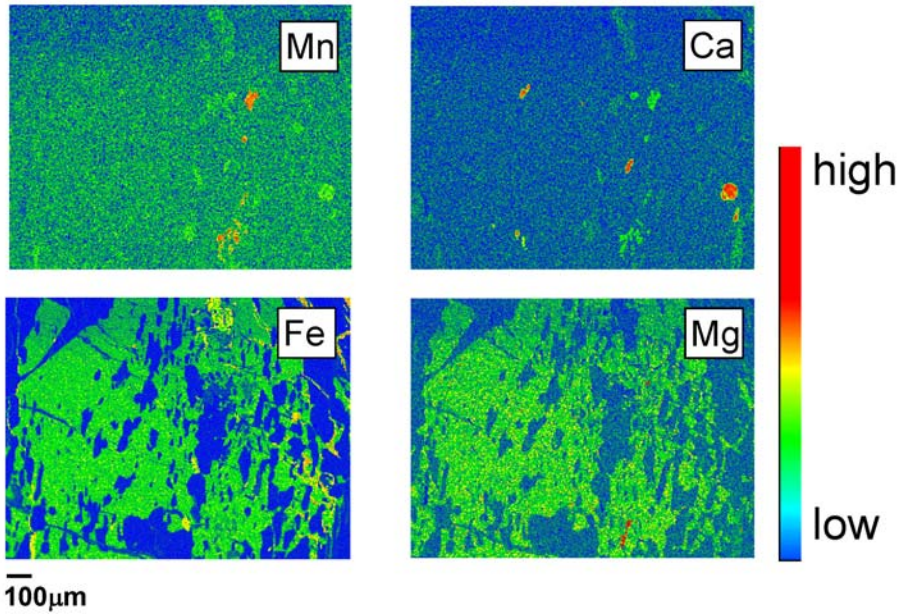

Figure 5.8 X-ray element maps of Mn, Ca, Fe, and Mg of garnet from MM03-28. See Figure 5.13 for a BSE image of this sample and Figure 5.12 for a compositional traverse across this garnet.

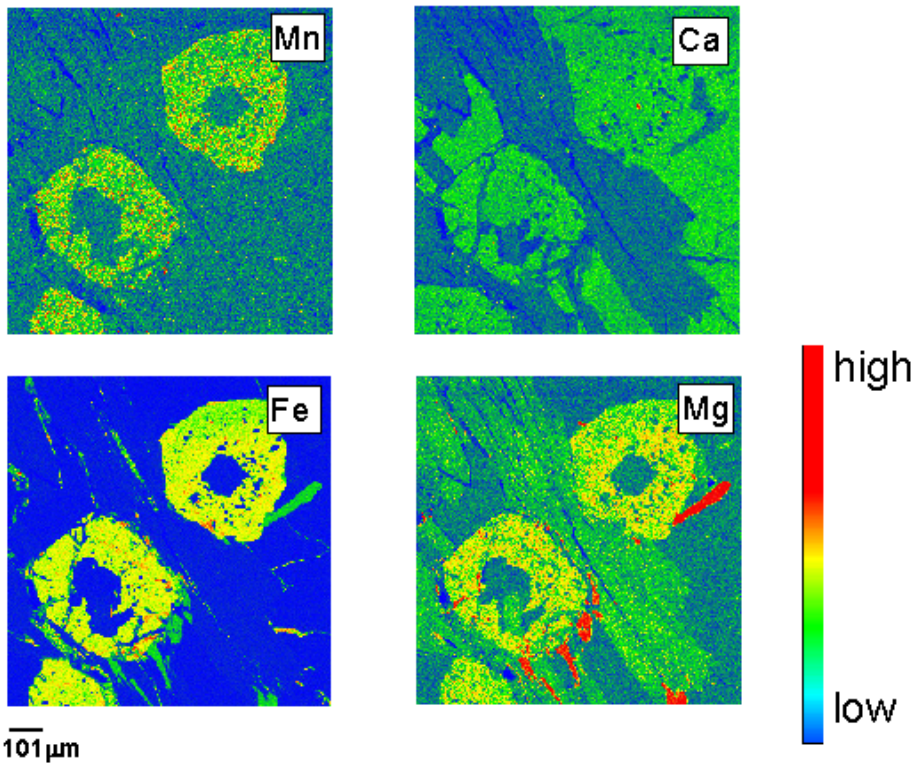

Figure 5.9 X-ray element maps of Mn, Ca, Fe, and Mg of garnets from MM03-32. See Figure 5.15 for a BSE image of this sample and Figure 5.14 for a compositional traverse across this garnet.

Although the X-ray element maps are useful for deciphering the qualitative zoning characteristics over a region within a garnet, compositional traverses show the chemical zoning in more detail. In Figures 5.10-5.15, compositional traverses and BSE images of Menderes Massif garnets from transect A-A' are presented.

Samples MM03-22 and MM03-23 were collected from the same outcrop. To compare their zoning characteristics, traverses were made from mid-rim to rim across a garnet in MM03-22 and from rim to core to rim in sample MM03-23 (Figures 5.10 and 5.11). The traverse across a garnet in sample MM03-22 in mole fraction spessartine from mid-rim to rim show a decrease in abundance towards the rim of the crystal from 0.074 to 0.041 with a sharp increase at the rim to 0.053. Fe/(Fe+Mg) broadly decreases from 0.859 to 0.823 with a slight increase at the rim to 0.833. These observations are consistent with prograde growth, with minor diffusive retrogression at the edge of the garnet. Grossular is flat at 0.138±0.033 mole fraction across the whole garnet, suggestive of a path of constant pressure.

The traverse across the garnet in sample MM03-23 shows a "bell-shape" profile from core, typical of a prograde growth. The spessartine content is high in the core (0.089) and decreases towards the rim (0.006) with a slight increase at the very edge of the crystal (to 0.010). Unlike MM03-22, the grossular content of this garnet is high in the core (0.291) and low in rim (0.007). Fe/(Fe+Mg) decreases from core to rim (from 0.952 to 0.860), consistent with growth under increasing T. These differences in the zoning profiles from garnets collected from the same outcrop suggest that the rocks experienced different metamorphic histories.

Although samples MM03-26, MM03-27, and MM03-28 were collected from the same outcrop, their compositional zoning characteristics are different. MM03-26 and MM03-28 shows prograde zoning whereas MM03-27 shows retrograde zoning. The spessartine content in MM03-26 is high in the core (0.021) and decreases towards the rim (0.005) with a slight increase at the very edge of the crystal (to 0.008). MM03-28 shows similar characteristics with MM03-26. In this sample, spessartine content is high in the core (0.025) of the garnet and decreases towards the rim (0.006). Unlike MM03-26 and MM03-28, the garnet in sample MM03-27 shows flat zoning in spessartine (0.010±0.001). The garnets in samples MM03-26 and MM03-28 have significantly less grossular content (0.051±0.010, 0.034±0.005) compared to the garnet in sample MM03-27 (0.148±0.011).

The compositional traverse across a garnet in MM03-32 (Figure 5.14) shows flat zoning in spessartine (0.023±0.004) with a slight increase at the very edge of the crystal (to 0.032). Fe/(Fe+Mg) content shows flat zoning (0.842±0.005). This behavior suggests that its composition homogenized via diffusion at high temperature and experienced retrograde garnet resorption during cooling (e.g., Florence and Spear, 1991).

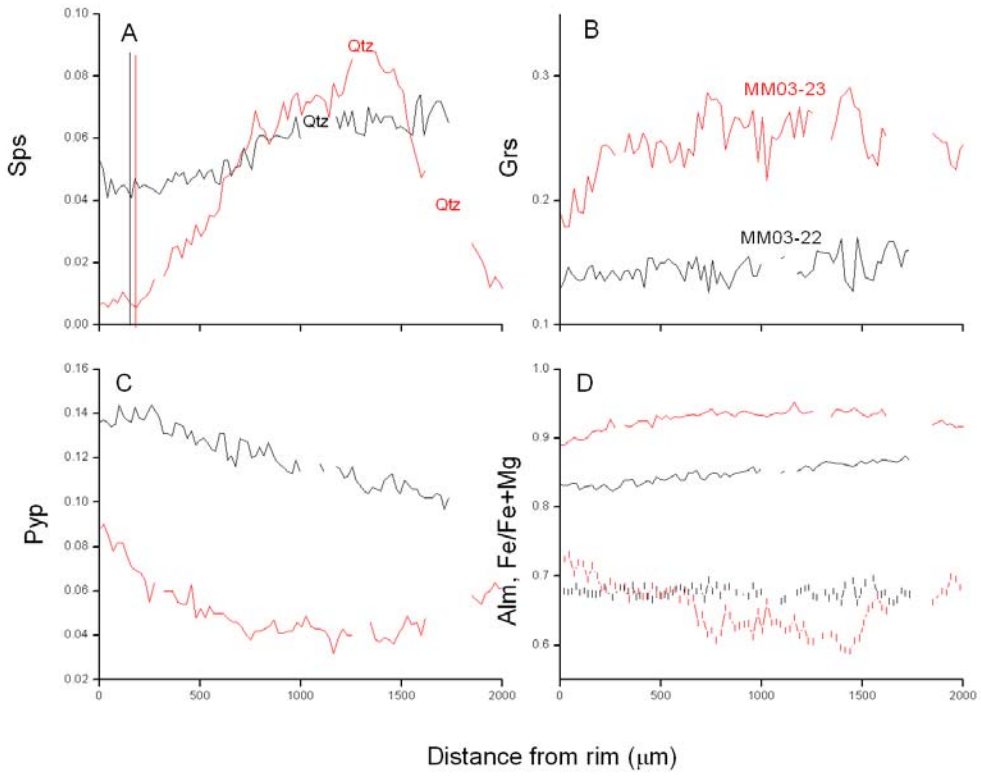

Figure 5.10 Compositional traverses in (A) Spessartine, (B) Grossular, (C) Pyrope, (D) Almandine and Fe/(Fe+Mg) across garnets in samples MM03-22 (black) and MM03-23 (red). Abbreviation: Qtz, Quartz inclusion. The vertical lines show the locations of compositions used for estimating the P-T conditions. Tick marks in (D) are plotted on the almandine traverses; the each tick corresponds to the location of an analysis. The length of the tick has no statistical significance.

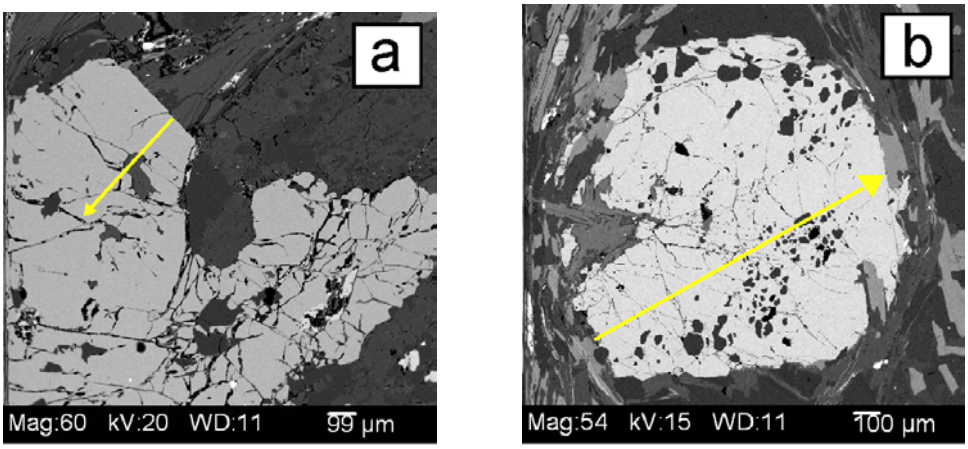

Figure 5.11 BSE images of sample MM03-22 (A) and MM03-23 (B). Arrows indicate the path of the compositional traverse plotted in Figure 5.10. The arrowheads indicate the end point.

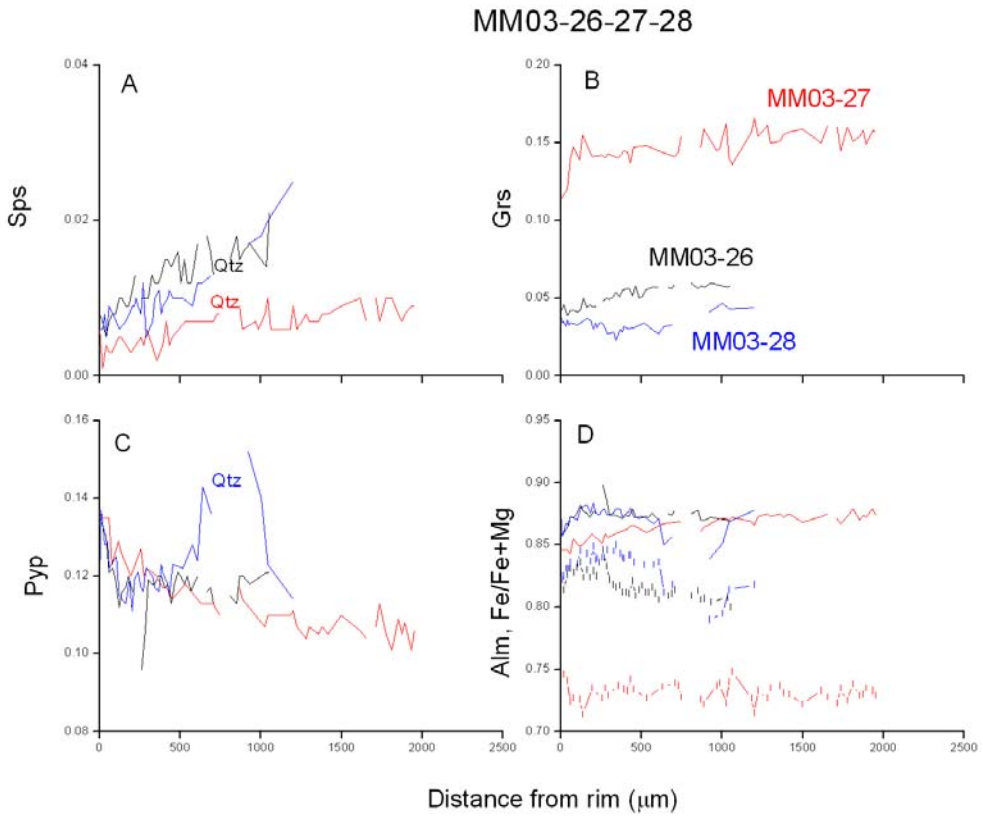

Figure 5.12 Compositional traverses in (A) Spessartine, (B) Grossular, (C) Pyrope, (D) Almandine and Fe/(Fe+Mg) across garnets in samples MM03-26 (black) and MM03-27 (red), and MM03-28 (blue). Abbreviation: Qtz, Quartz inclusion. Tick marks in (D) are plotted on the almandine traverses; the each tick corresponds to the location of an analysis. The length of the tick has no statistical significance.

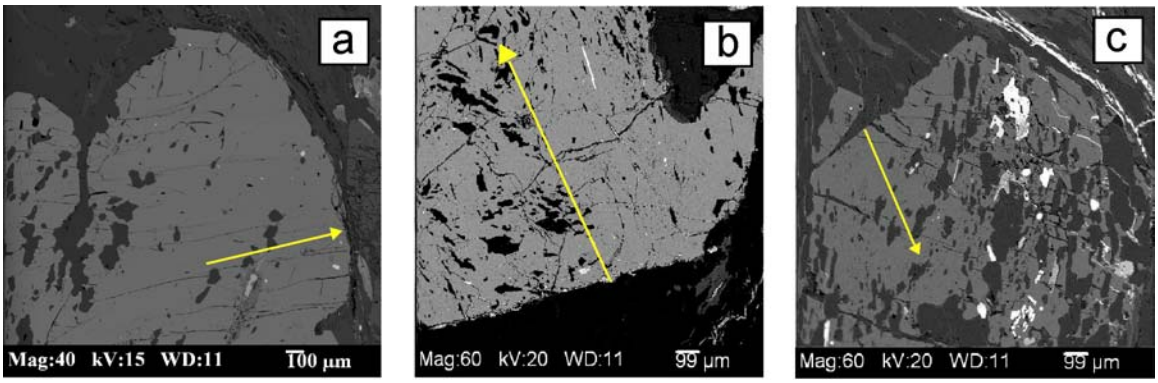

Figure 5.13 BSE images of sample MM03-26 (A) and MM03-27 (B) and MM03-28 (C). Arrows indicate the path of the compositional traverse plotted in Figure 5.12. The arrowheads indicate the end point.

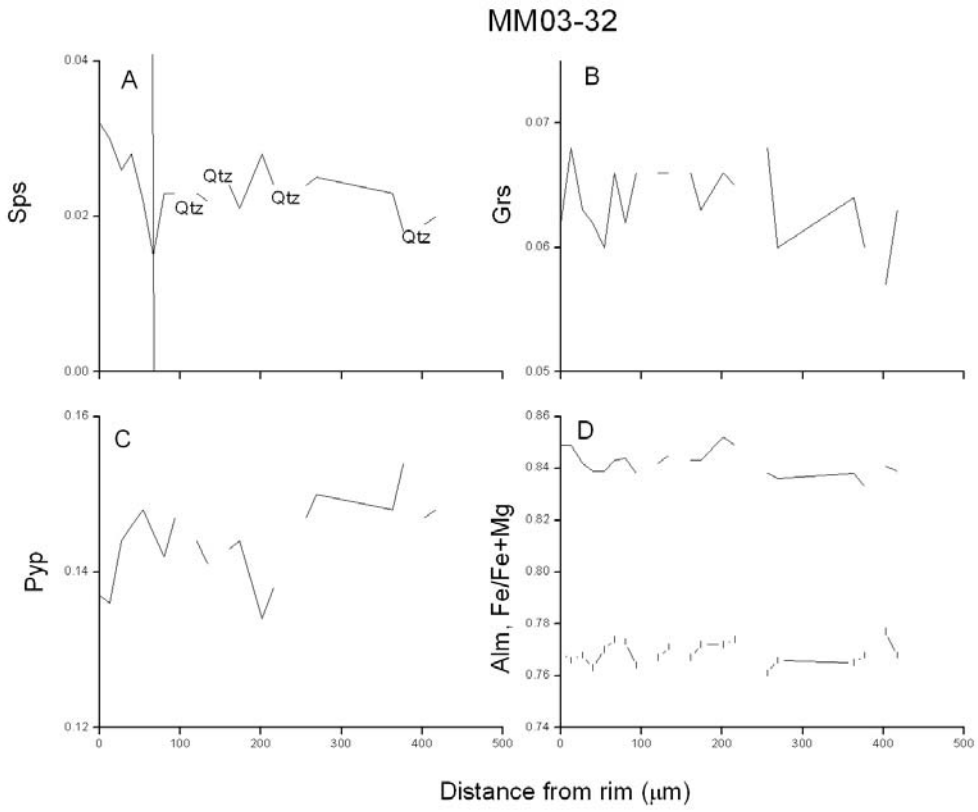

Figure 5.14 Compositional traverses in (A) Spessartine, (B) Grossular, (C) Pyrope, (D) Almandine and Fe/(Fe+Mg) across a garnet in sample MM03-32. Abbreviation: Qtz, Quartz inclusion. Tick marks in (D) are plotted on the almandine traverses; the each tick corresponds to the location of an analysis. The length of the tick has no statistical significance.

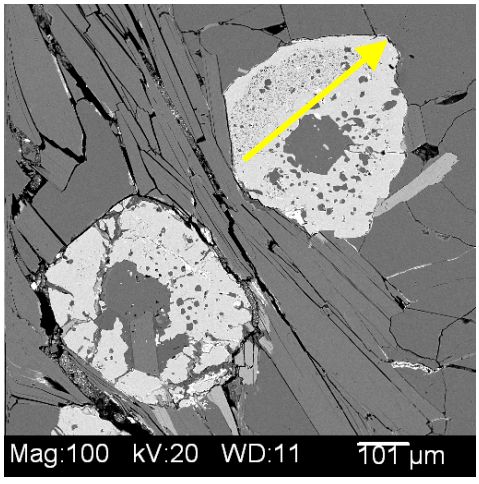

Figure 5.15 BSE image of sample MM03-32. Arrow indicates where the traverse obtained (Figure 5.14). Arrows indicate the path of the compositional traverse plotted in Figure 5.14. The arrowheads indicate the end point.

Tables 5.2, 5.3 and 5.4 show mineral compositions that were used for thermobarometric calculations plotted in Figure 5.16. As indicated in Chapter 4, the garnet compositions were obtained from the lowest Mn and lowest Fe/(Fe+Mg) values, and Figures 5.10 and 5.14 shows where these locations are along the garnet traverses. The garnet-biotite thermometer (Ferry and Spear, 1978; Berman, 1990) and garnet-biotite-muscovite-plagioclase barometer (Hoisch, 1990) were used (see Chapter 4).

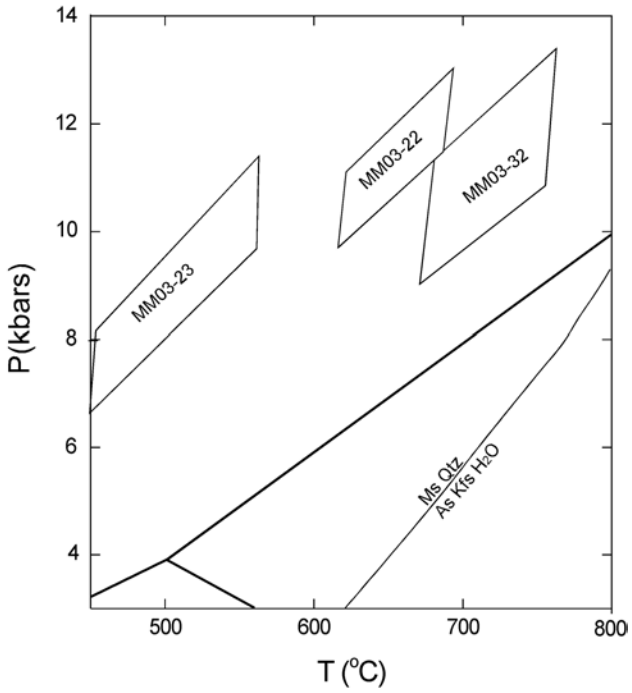

Figure 5.16 P-T diagram of transect A-A' samples MM03-22, MM03-23, and MM03-32. Also shown is the stability field of the aluminosilicate polymorphs and muscovite dehydration melting curve (Chatterjee and Johannes, 1974). Abbreviations: Ms, muscovite; Qtz, quartz; As; Aluminosilicate; Kfs; K-Feldspar.

The mineral assemblages of these samples (Table 4.1) are consistent with the P-T conditions, as all appear within the muscovite stability field. Sample MM03-22 records 650±40°C and 11.4±1.6 kbar; sample MM03-23 records 505±55°C and 9.0±2.4 kbar; and sample MM03-32 records 715±55°C and 11.2±2.2 kbar. Samples MM03-22 and MM03-23 were collected from the same outcrop, and experienced P conditions within

uncertainty. However, they appear to have experienced T conditions that differ by as much as 240°C, including uncertainty. Sample MM03-32 was collected furthest from the Kuzey detachment, but records P-T conditions within uncertainty of sample MM03-22 but just barely with respect to temperature.

Table 5.2 Mineral composition of MM03-22 used in thermobarometric calculations.

	Garnet[b]	Garnet	Biotite[b]	Biotite	Plag[b]	Plag	Mus[b]	Mus
SiO_2	37.42	36.46	36.32	35.23	61.65	62.76	45.39	47.58
Al_2O_3	20.62	20.11	18.95	19.16	23.00	23.26	36.79	34.01
MnO	1.94	1.94	0.01	0.05	-	0.02	-	-
MgO	3.59	3.58	11.67	11.30	0.01	-	0.79	1.50
CaO	4.75	4.98	0.02	0.07	4.67	4.59	0.03	0.01
Na_2O	-[a]	0.01	0.14	0.10	8.21	7.05	0.71	0.81
FeO	30.12	29.71	15.39	17.38	0.03	0.06	1.05	1.23
TiO_2	0.05	0.07	1.99	1.86	0.01	0.00	0.36	0.36
Cr_2O_3	0.01	-	-	0.08	0.10	0.05	0.21	0.00
K_2O	-	-	8.55	8.77	0.07	0.06	7.85	9.38
Total	98.5	96.9	93.03	94.00	97.74	97.85	93.17	94.87
Si	3.02	3.00	5.51	5.37	2.78	2.81	6.07	6.31
Al	1.96	1.95	3.39	3.44	1.22	1.23	5.80	5.32
Mn	0.13	0.14	-	0.01	-	-	-	-
Mg	0.43	0.44	2.64	2.57	-	-	0.16	0.30
Ca	0.41	0.44	-	0.01	0.23	0.22	-	-
Na	-	-	0.04	0.03	0.72	0.61	0.18	0.21
Fe	2.03	2.05	1.95	2.21	-	-	0.12	0.14
Ti	-	-	0.23	0.21	-	-	0.04	0.04
Cr	-	-	-	0.01	-	-	0.02	-
K	-	-	1.65	1.71	-	-	1.34	1.59
Total [a]	8.0	8.0	15.42	15.56	4.96	4.88	13.74	13.89

a. "-" indicates measured but not detected.
b. Formula of garnet is calculated on the basis of 12 oxygens, biotite and muscovite are calculated on the basis of 24 oxygens, and plagioclase is calculated on the basis of 8 oxygens.

Table 5.3 Mineral composition of MM03-23 used in thermobarometric calculations.[a]

	Garnet[b]	Garnet	Biotite[b]	Biotite	Plag[b]	Plag	Mus[b]	Mus
SiO_2	36.64	38.39	37.92	36.33	64.79	63.73	48.63	48.80
Al_2O_3	21.11	19.97	16.94	17.96	22.58	23.00	36.86	35.71
MnO	0.25	0.53	-	-	0.01	0.07	-	0.04
MgO	2.16	2.96	12.84	12.41	0.01	0.01	0.71	0.73
CaO	6.36	5.68	-	-	3.36	4.24	0.02	0.02
Na_2O	-	0.27	0.35	0.30	8.79	8.38	0.83	1.55
FeO	33.28	32.42	16.04	17.32	0.14	0.01	1.07	0.93
TiO_2	0.11	0.06	1.62	1.63	0.02	0.02	0.42	0.50
Cr_2O_3	0.03	-	0.04	-	0.11	0.08	-	0.08
K_2O	-	-	8.37	8.80	0.06	0.09	5.05	7.71
Total	99.9	100.3	94.1	94.8	99.9	99.6	93.6	96.1
Si	2.95	3.06	5.69	5.48	2.85	2.82	6.33	6.32
Al	2.01	1.88	3.00	3.19	1.17	1.20	5.65	5.45
Mn	0.02	0.04	-	-	-	-	-	-
Mg	0.26	0.35	2.87	2.79	-	-	0.14	0.14
Ca	0.55	0.49	-	-	0.16	0.20	-	-
Na	-	0.04	0.10	0.09	0.75	0.72	0.21	0.39
Fe	2.24	2.16	2.01	2.19	0.01	-	0.12	0.10
Ti	0.01	-	0.18	0.19	-	-	0.04	0.05
Cr	-	-	-	-	-	-	-	0.01
K	-	-	1.60	1.69	-	-	0.84	1.27
Total [a]	8.0	8.0	15.47	15.62	4.94	4.94	13.33	13.74

a. "-" indicates measured but not detected.

b. Formula of garnet is calculated on the basis of 12 oxygens, biotite and muscovite are calculated on the basis of 24 oxygens, and plagioclase is calculated on the basis of 8 oxygens.

Table 5.4 Mineral composition of MM03-32 used in thermobarometric calculations.

	Garnet[b]	Garnet	Biotite[b]	Biotite	Plag[b]	Plag	Mus[b]	Mus
SiO_2	36.67	35.92	36.12	34.36	67.63	64.79	45.45	49.04
Al_2O_3	20.77	20.61	18.84	18.68	21.81	22.14	36.21	35.22
MnO	0.69	0.87	0.11	0.09	0.01	0.08	-	-
MgO	3.69	3.83	10.01	9.77	0.01	-	0.90	1.07
CaO	2.36	2.06	-	-	2.73	3.30	0.02	0.02
Na_2O	0.00	0.02	0.13	0.07	9.67	8.90	0.92	1.57
FeO	35.18	36.03	19.39	19.92	0.52	0.40	1.28	1.02
TiO_2	0.03	-	1.57	1.67	-	-	0.57	0.64
Cr_2O_3	-	-	0.05	-	0.11	0.07	0.03	0.09
K_2O	-	-	9.41	9.29	0.06	0.02	5.61	8.68
Total	99.4	99.3	95.6	93.9	102.6	99.7	91.0	97.3
Si	2.97	2.93	5.47	5.34	2.90	2.86	6.15	6.31
Al	1.98	1.98	3.36	3.42	1.10	1.15	5.77	5.34
Mn	0.05	0.06	0.01	0.01	-	-	-	-
Mg	0.45	0.47	2.26	2.26	-	-	0.18	0.21
Ca	0.20	0.18	-	-	0.13	0.16	-	-
Na	-	-	0.04	0.02	0.80	0.76	0.24	0.39
Fe	2.38	2.46	2.45	2.59	0.02	0.01	0.14	0.11
Ti	-	-	0.18	0.20	-	-	0.06	0.06
Cr	-	-	0.01	-	-	-	-	0.01
K	-	-	1.82	1.84	-	-	0.97	1.43
Total [a]	8.0	8.1	15.60	15.69	4.95	4.95	13.51	13.86

a. "-" indicates measured but not detected.
b. Formula of garnet is calculated on the basis of 12 oxygens, biotite and muscovite are calculated on the basis of 24 oxygens, and plagioclase is calculated on the basis of 8 oxygens.

5.2.2 Transect B-B'

Samples MM03-33 through MM03-41 were collected along transect B-B' (Figure 5.17). Only samples MM03-33, MM03-36, MM03-37, MM03-38, MM03-40, and MM03-41 contain garnet and are plotted on the cross section. Field photos of MM03-33, MM03-36, and MM03-37 (Figure 5.18), MM03-38, MM03-40 and MM03-41 (Figure 5.19) show the outcrops where those samples were collected.

All garnets collected along transect B-B' are interpreted to have retrograde zoning (Table 5.1). X-ray element maps of a garnet from sample MM03-38 shows no zoning

characteristics, indicating its composition homogenized via diffusion at high temperature. All samples from this transect have flat Mn and Fe zoning, except samples MM03-33 and MM03-37 (Figure 5.20 and 5.22) which have low Mn cores and high Mn rims and low Fe cores and high Fe rims. Samples MM03-33 and MM03-36 have flat Ca zoning (Figure 5.20 and 5.21); samples MM03-37 and MM03-41 have high Ca cores and low Ca rims; and sample MM03-40 has a low Ca core and high Ca rim (Figure 5.24). All samples have flat Mg zoning, except samples MM03-36 and MM03-37, which show opposite Mg zoning maps. A garnet from sample MM03-36 has a high Mg core and low Mg rim (Figure 5.21), whereas a garnet from sample MM03-37 has a low Mg core and high Mg rim (Figure 5.22). These observations, from rocks collected within 2 km from the same Paleozoic schist unit suggest the possibility that the rocks experienced different metamorphic histories.

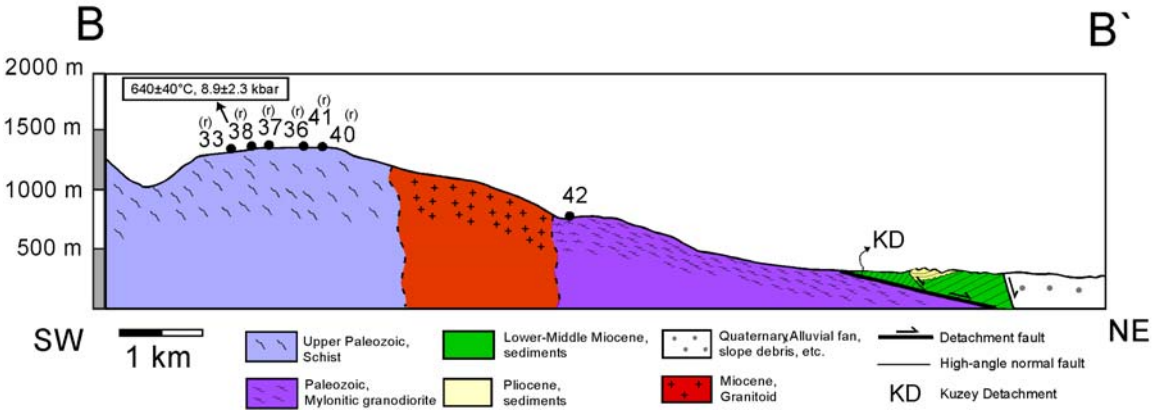

Figure 5.17 Transect B-B' showing the location of the samples and P-T data. See Figures 5.20 to 5.25 for garnet X-ray element maps and Figures 5.26 for garnet traverses. Abbreviations: (p) prograde zoning, (r) retrograde zoning.

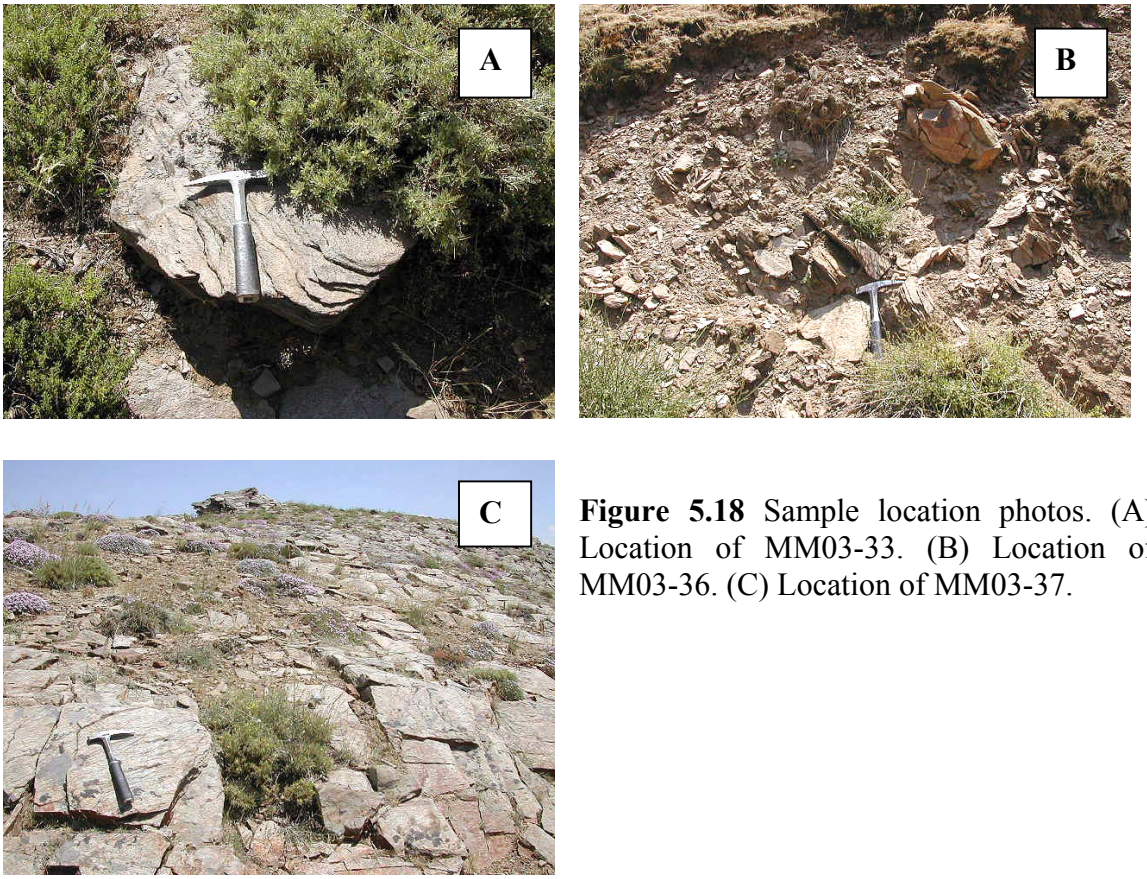

Figure 5.18 Sample location photos. (A) Location of MM03-33. (B) Location of MM03-36. (C) Location of MM03-37.

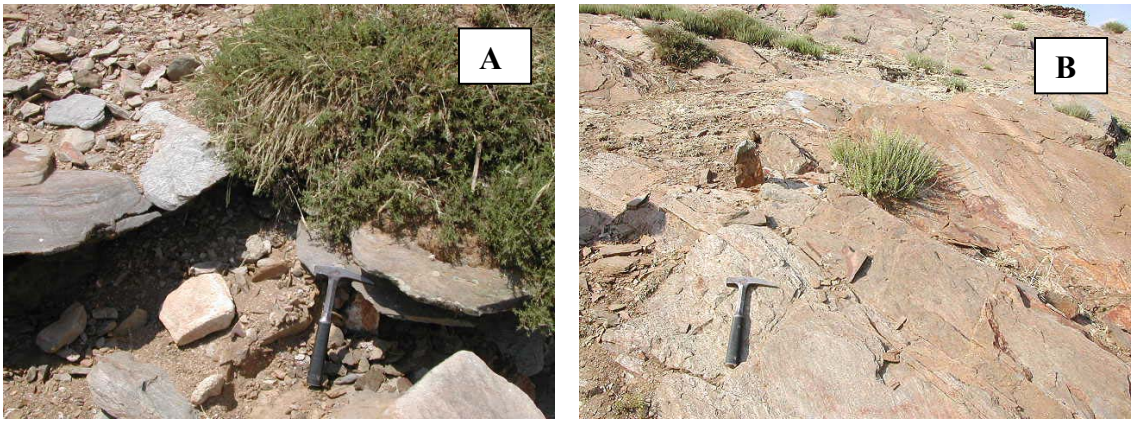

Figure 5.19 Sample location photos. (A) Location of MM03-38. (B) Location of MM03-40. (C) Location of MM03-41.

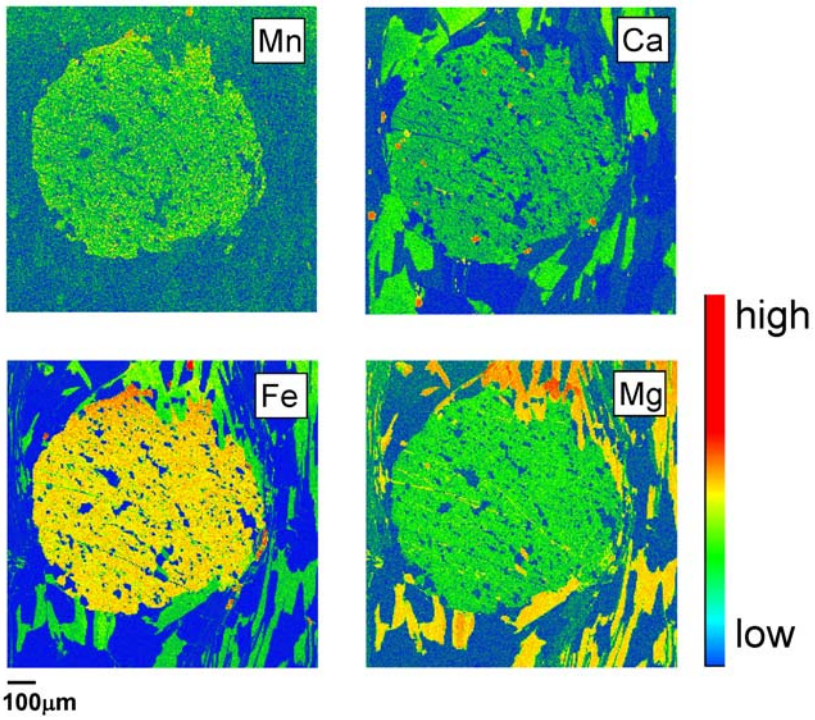

Figure 5.20 X-ray element maps of Mn, Ca, Fe, and Mg of a garnet from MM03-33. See Figure 5.27 for a BSE image of this sample and Figure 5.26 for a compositional traverse across this garnet.

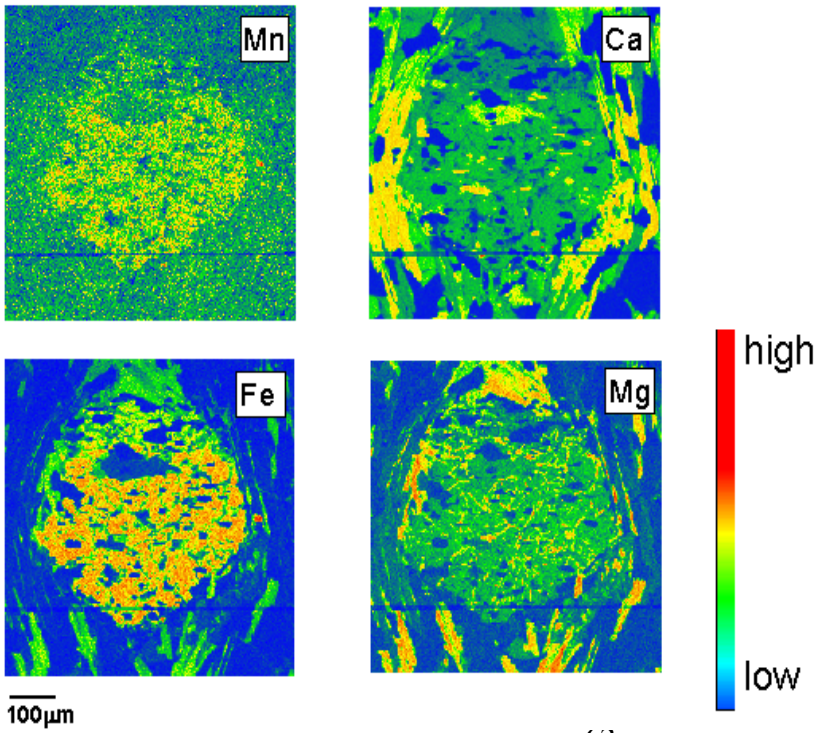

Figure 5.21 X-ray element maps of Mn, Ca, Fe, and Mg of a garnet from MM03-36.

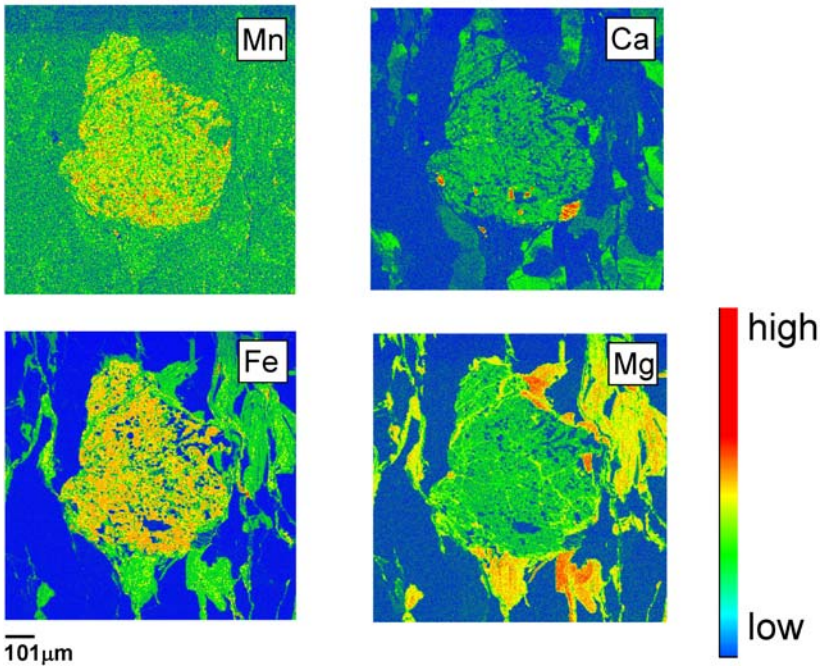

Figure 5.22 X-ray element maps of Mn, Ca, Fe, and Mg of a garnet from MM03-37.

.

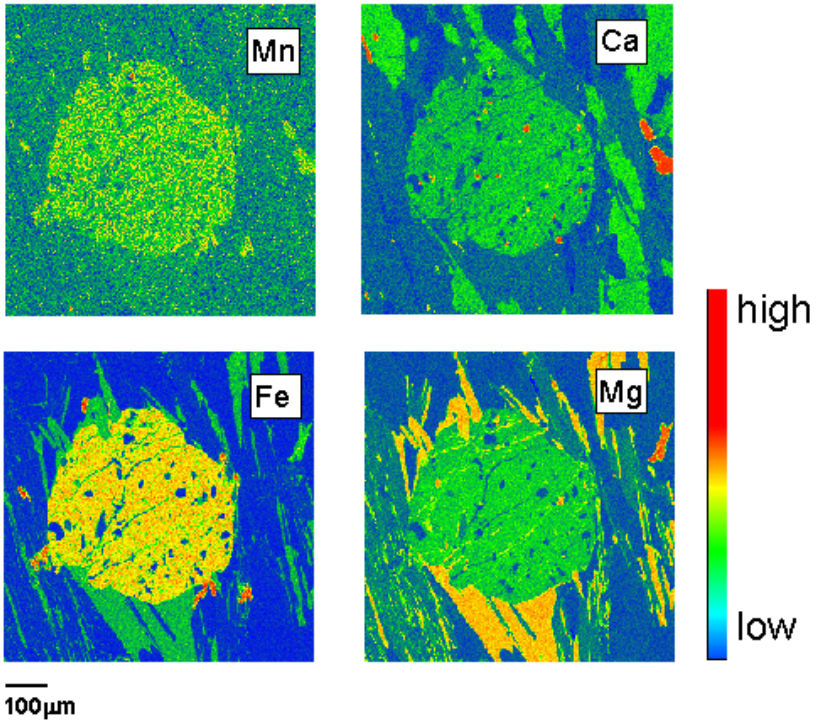

Figure 5.23 X-ray element maps of Mn, Ca, Fe, and Mg of a garnet from MM03-38. See Figure 5.27 for a BSE image of this sample and Figure 5.26 for a compositional traverse across this garnet.

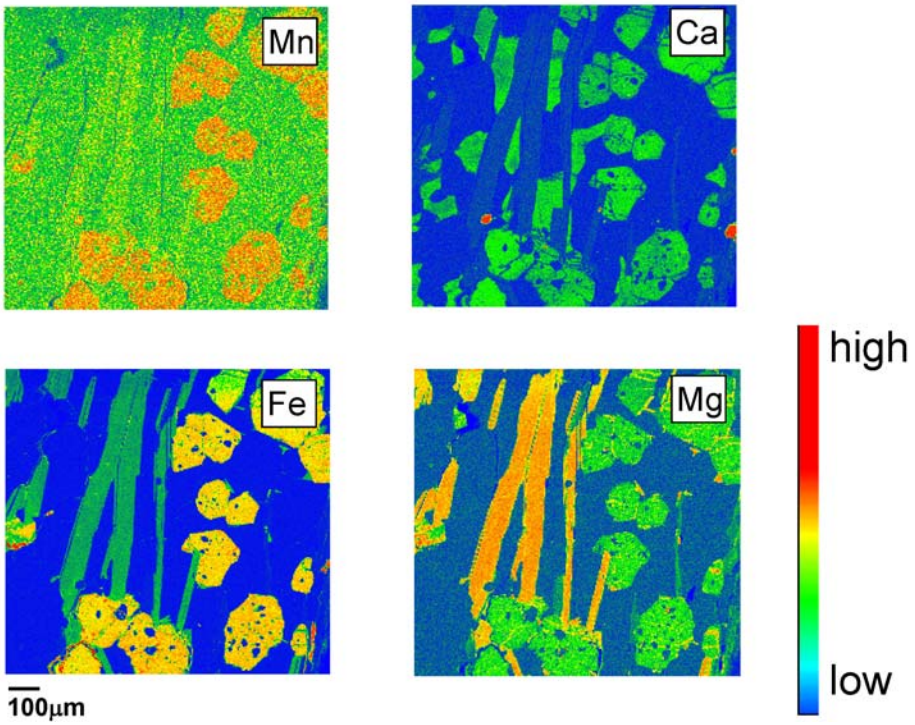

Figure 5.24 X-ray element maps of a Mn, Ca, Fe, and Mg of garnet from MM03-40.

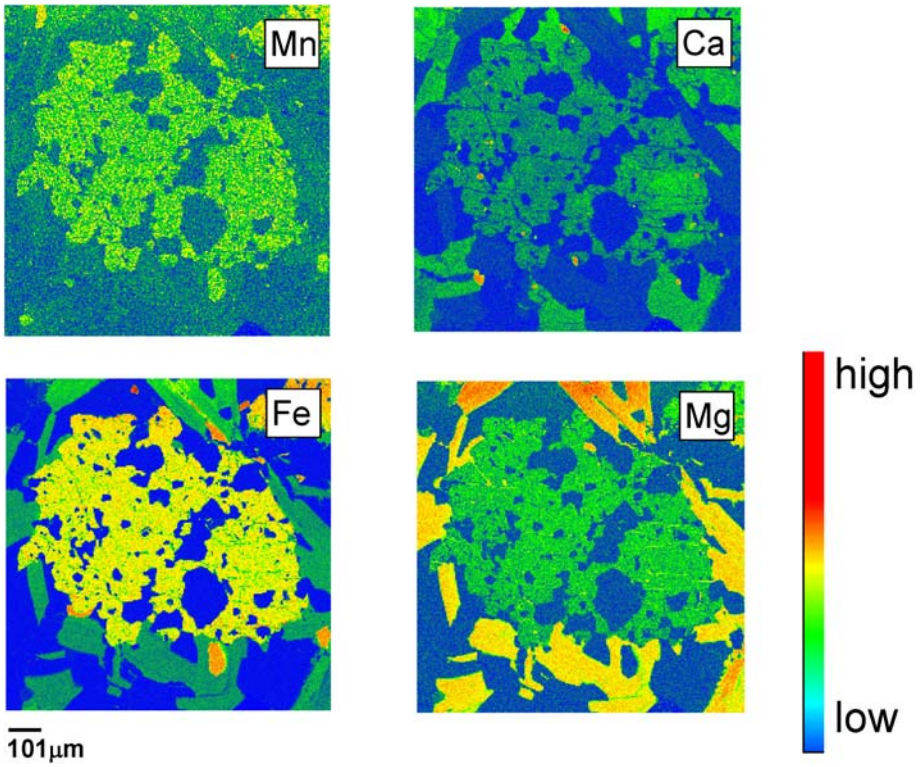

Figure 5.25 X-ray element maps of Mn, Ca, Fe, and Mg of a garnet from MM03-41.

Along transect B-B', compositional traverses were made across garnets from samples MM03-33 and MM03-38 (Figure 5.26). These traverses show that both samples have garnets that are similar in chemical content and zoning. For example, the garnet in sample MM03-33 increases from 0.020 in the core to 0.031 at the rim, whereas MM03-38 increases from 0.020 to 0.050 at the rim. The pyrope content of the garnet in MM03-33 is high in the core (0.170) and decreases towards the rim (0.134), and the pyrope content of the garnet in MM03-38 is high in the core (0.161) and low in the rim (0.115). The Fe/(Fe+Mg) content of both MM03-33 and MM03-38 increases towards the rim. MM03-33 has a Fe/(Fe+Mg) value of 0.825±0.008 for the core, which increases to 0.847 at the rim, whereas MM03-38 has a Fe/(Fe+Mg) value of 0.834±0.011, which increases to 0.869 at the rim.

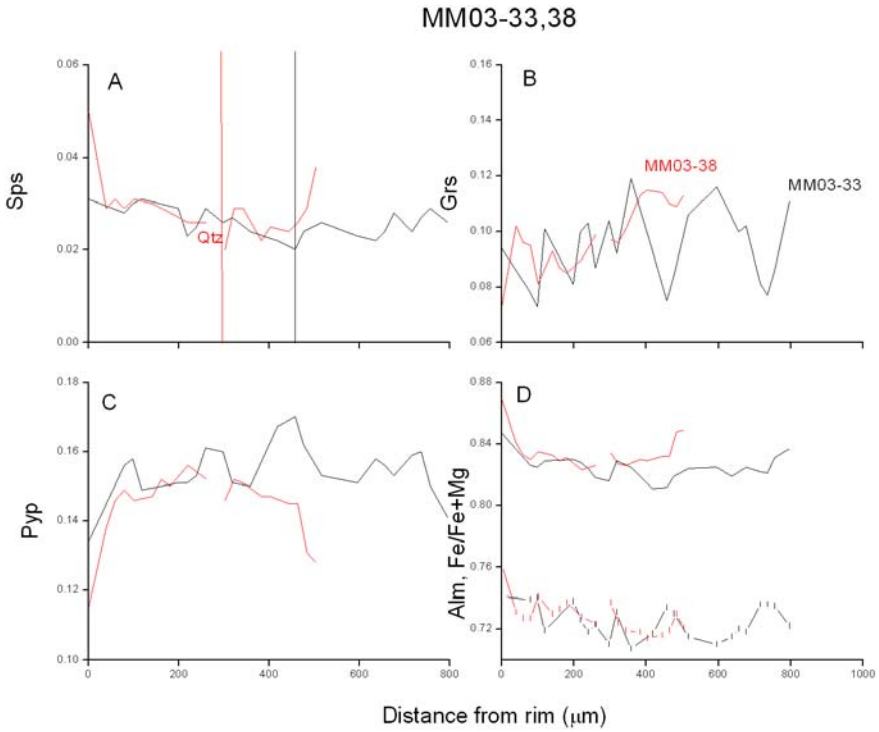

Figure 5.26 Compositional traverses in (A) Spessartine, (B) Grossular, (C) Pyrope, (D) Almandine and Fe/(Fe+Mg) across garnets in samples MM03-33 and MM03-38. Abbreviation: Qtz, Quartz inclusion. Tick marks in (D) are plotted on the almandine traverses; the each tick corresponds to the location of an analysis. The length of the tick has no statistical significance.

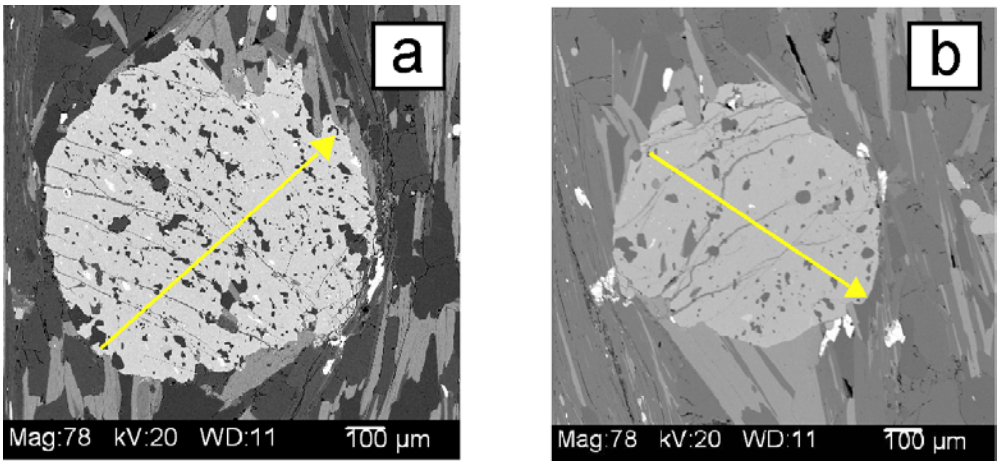

Figure 5.27 (a) BSE image of sample MM03-33. (b) BSE image of sample MM03-38. Arrows indicate where the traverses obtained. Arrow heads indicate the end points.

The mineral compositions from sample MM03-33 (Table 5.5) and MM03-38 (Table 5.6) were used for thermobarometric calculations. Figure 5.28 shows the P-T conditions of the samples MM03-33 (680±45°C and 10.3 ± 3.1 kbar) and MM03-38 (640±40°C and 8.9 ± 2.3 kbar). These conditions are consistent with their mineral assemblages and X-ray element maps that show the samples experienced retrograde diffusion.

Table 5.5 Mineral composition of MM03-33 used in thermobarometric calculations.

	Garnet[b]	Garnet	Biotite[b]	Biotite	Plag[b]	Plag	Mus[b]	Mus
SiO_2	36.79	38.46	35.96	37.28	63.21	65.24	45.65	46.68
Al_2O_3	21.34	20.93	18.64	19.82	23.80	23.63	37.03	34.44
MnO	0.99	0.90	0.08	0.06	0.05	0.01	0.00	0.00
MgO	4.22	4.26	10.27	11.27	0.01	0.00	0.48	0.94
CaO	3.26	2.62	0.03	0.03	4.45	3.68	0.00	0.00
Na_2O	0.00	0.00	0.05	0.18	6.21	8.86	0.93	0.93
FeO	32.20	32.82	17.35	16.48	0.00	0.01	0.81	1.10
TiO_2	0.21	0.04	1.56	1.72	0.02	0.00	0.46	0.73
Cr_2O_3	0.06	0.02	0.01	0.04	0.00	0.05	0.02	0.00
K_2O	-	-	8.52	8.18	0.13	0.02	7.67	8.21
Total	99.1	100.0	92.5	95.1	97.9	101.5	93.1	93.0
Si	2.96	3.05	5.55	5.53	2.82	2.82	6.10	6.27
Al	2.02	1.96	3.39	3.47	1.25	1.21	5.83	5.45
Mn	0.07	0.06	0.01	0.01	-	-	-	-
Mg	0.51	0.50	2.36	2.49	-	-	0.10	0.19
Ca	0.28	0.22	-	0.01	0.21	0.17	-	-
Na	-	-	0.02	0.05	0.54	0.74	0.24	0.24
Fe	2.17	2.18	2.24	2.04	-	-	0.09	0.12
Ti	0.01	-	0.18	0.19	-	-	0.05	0.07
Cr	-	0.01	-	0.01	-	-	-	-
K	-	-	1.68	1.55	-	-	1.31	1.41
Total [a]	8.0	8.0	15.42	15.34	4.83	4.95	13.71	13.76

a. "-" indicates measured but not detected.

b. Formula of garnet is calculated on the basis of 12 oxygens, biotite and muscovite are calculated on the basis of 24 oxygens, and plagioclase is calculated on the basis of 8 oxygens.

Table 5.6 Mineral composition of MM03-38 used in thermobarometric calculations.

	Garnet[b]	Garnet	Biotite[b]	Biotite	Plag[b]	Plag	Mus[b]	Mus
SiO_2	37.16	37.14	35.93	35.43	67.63	64.79	45.48	47.36
Al_2O_3	21.81	21.18	20.26	19.07	21.81	22.14	37.50	35.10
MnO	0.90	1.11	0.05	0.10	0.01	0.08	0.00	0.00
MgO	3.70	4.13	11.32	11.10	0.01	-	0.85	0.95
CaO	3.40	2.62	0.02	0.02	2.73	3.30	0.01	0.01
Na_2O	0.01	0.01	0.21	0.15	9.67	8.90	0.70	0.63
FeO	33.24	33.87	16.53	18.67	0.52	0.40	1.21	1.04
TiO_2	0.01	0.03	1.67	1.57	-	-	0.62	0.76
Cr_2O_3	0.05	0.08	0.07	0.00	0.11	0.07	0.05	0.00
K_2O	-	-	7.76	8.11	0.06	0.02	5.58	6.47
Total	100.3	100.2	93.82	94.22	102.55	99.70	91.99	92.33
Si	2.96	2.97	5.41	5.39	2.90	2.86	6.07	6.32
Al	2.05	2.00	3.59	3.42	1.10	1.15	5.90	5.52
Mn	0.06	0.08	0.01	0.01	-	-	0.00	0.00
Mg	0.44	0.49	2.54	2.52	-	-	0.17	0.19
Ca	0.29	0.22	0.00	0.00	0.13	0.16	0.00	0.00
Na	-	-	0.06	0.04	0.80	0.76	0.18	0.16
Fe	2.21	2.26	2.08	2.38	0.02	0.01	0.14	0.12
Ti	-	-	0.19	0.18	-	-	0.06	0.08
Cr	-	0.01	0.01	0.00	-	-	0.00	0.00
K	-	-	1.49	1.57	-	-	0.95	1.10
Total [a]	8.0	8.0	15.38	15.53	4.95	4.95	13.48	13.48

a. "-" indicates measured but not detected.

b. Formula of garnet is calculated on the basis of 12 oxygens, biotite and muscovite are calculated on the basis of 24 oxygens, and plagioclase is calculated on the basis of 8 oxygens.

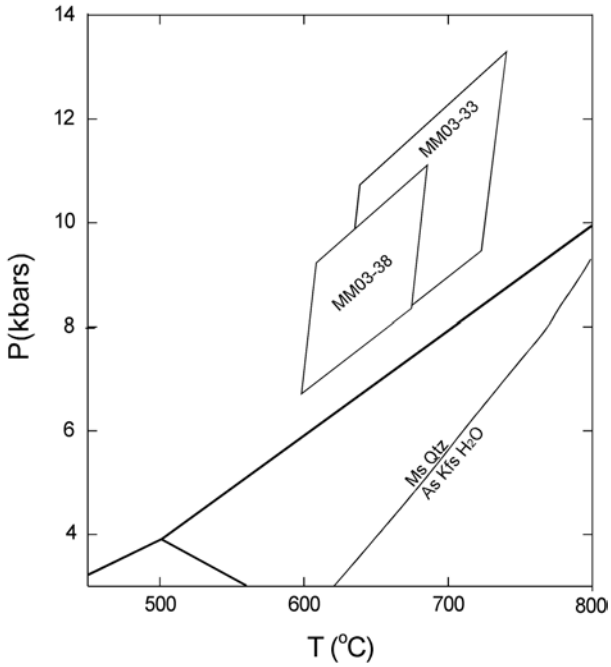

Figure 5.28 P-T diagram of transect B-B' samples MM03-33 and MM03-38. Also shown is the stability field of the aluminosilicate polymorphs and muscovite dehydration melting curve (Chatterjee and Johannes, 1974). Abbreviations: Ms, muscovite; Qtz, quartz; As; Aluminosilicate; Kfs; K-Feldspar.

5.2.3 Transect C-C'

Samples MM03-45 through MM03-48 were collected along transect C-C' (Figure 5.33). Only samples MM03-45 and MM03-48 contained garnet and are plotted on the cross section. Field photos of MM03-45 and MM03-48 (Figure 5.30) show the outcrops where those samples were collected.

X-ray element maps of garnets in samples MM03-45 and MM03-48 show prograde zoning, with high Mn cores and low Mn rims. However, these garnets differ in Ca, Mg, and Fe zoning. The garnet in sample MM03-45 has flat zoning in Ca, Mg, and Fe. However, the garnet in sample MM03-48 has a high Fe and high Ca core and low Fe and low Ca in the rim, but a low Mg core and a high Mg rim.

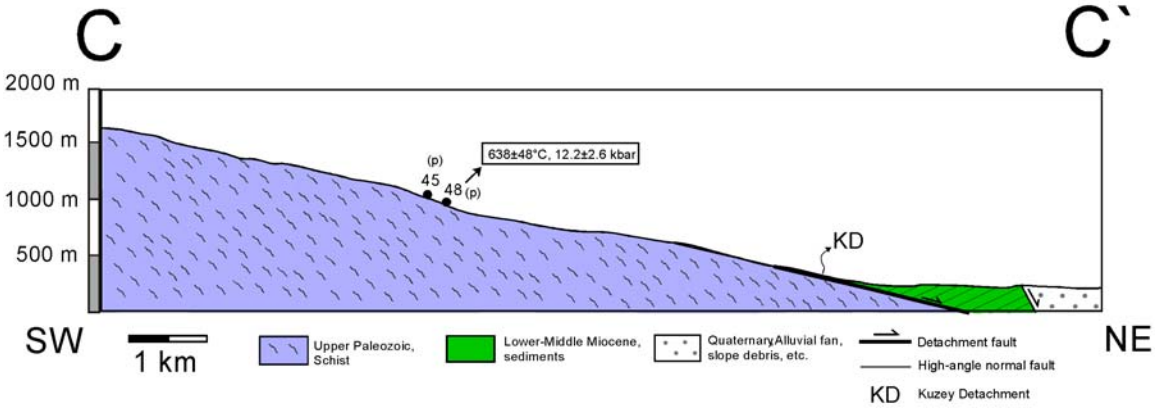

Figure 5.29 Transect C-C' showing the location of the samples and P-T data. See Figures 5.31 to 5.32 for garnet X-ray element maps and Figures 5.33 for garnet traverse. Abbreviations: (p) prograde zoning, (r) retrograde zoning.

Figure 5.30 Sample location photos. (A) Location of MM03-45 B) Location of MM03-48

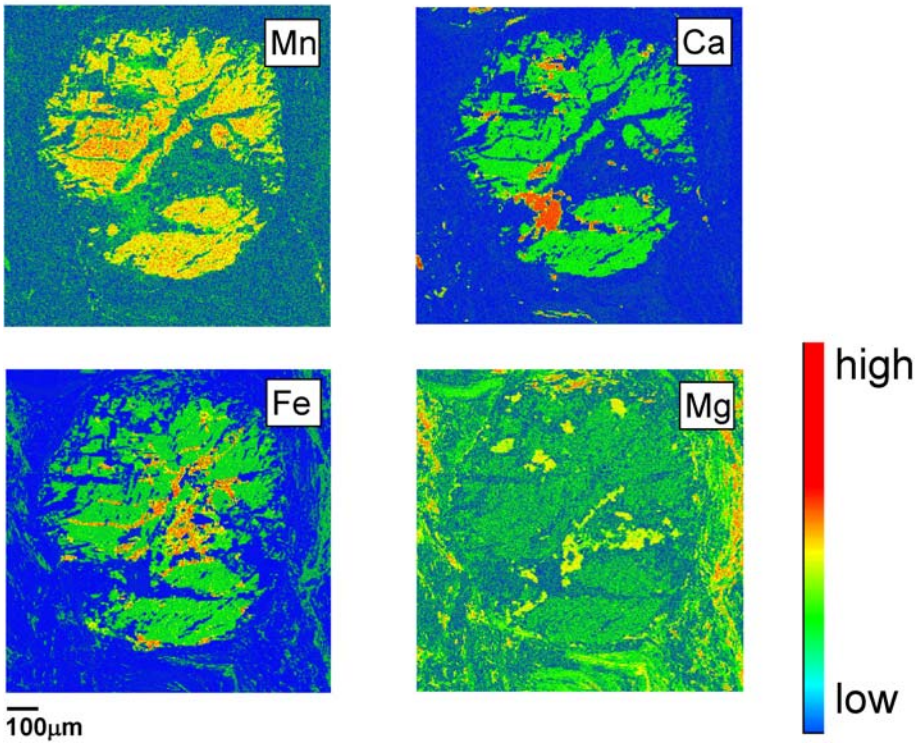

Figure 5.31 X-ray element maps of Mn, Ca, Fe, and Mg of a garnet from MM03-45.

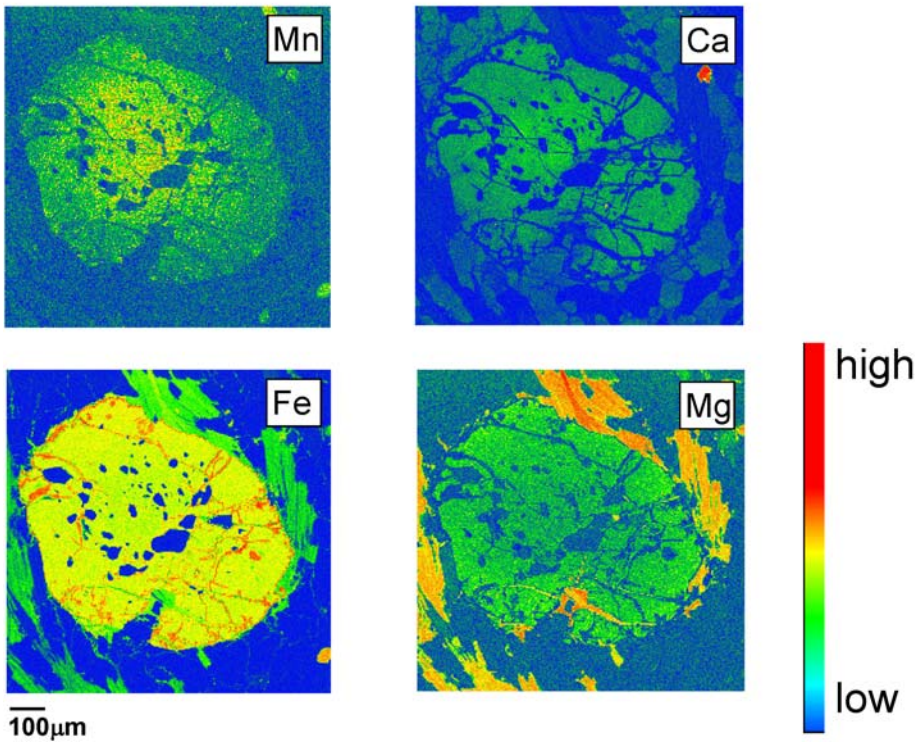

Figure 5.32 X-ray element maps of Mn, Ca, Fe, and Mg of a garnet from MM03-48. See Figure 5.34 for a BSE image of this sample and Figure 5.33 for a compositional traverse across this garnet.

A compositional traverse was only made across the garnet in sample MM03-48. The traverse reveals a sharp increase in spessartine content from 0.008 in the core to 0.022 at the rim. This was not immediately evident from the X-ray element map. The grossular and pyrope content steadily decrease from core to rim, from 0.121 mole fraction grossular in the core to 0.091 at the rim and 0.154 mole fraction pyrope in the core to 0.149 at the rim. The Fe/(Fe+Mg) content of this garnet show flat zoning (0.147±0.006).

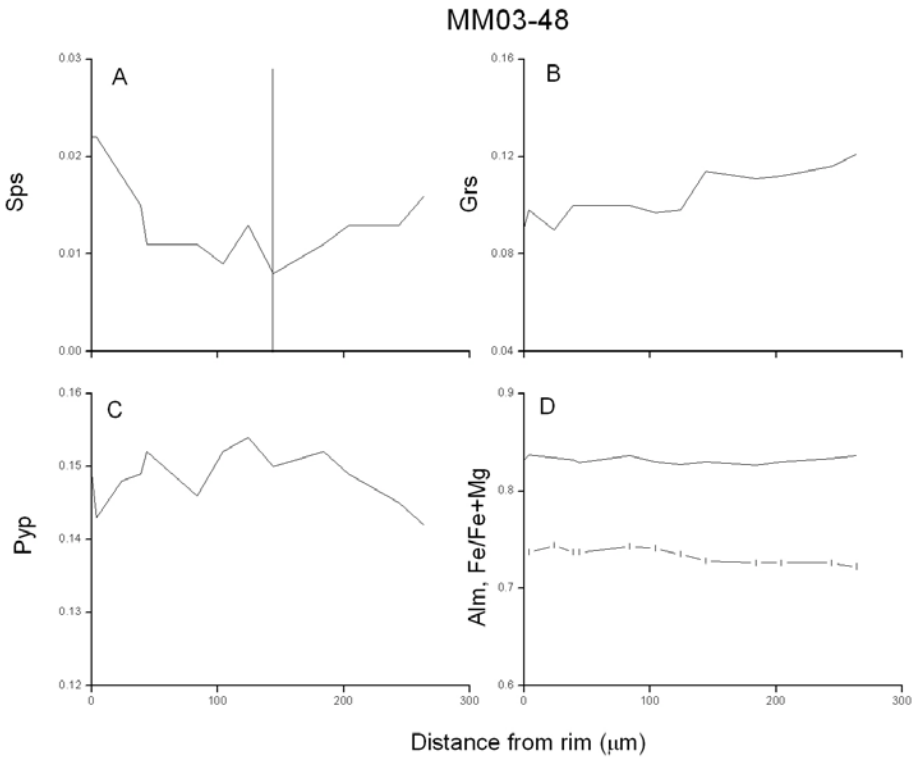

Figure 5.33 Compositional traverses in (A) Spessartine, (B) Grossular, (C) Pyrope, (D) Almandine and Fe/(Fe+Mg) across a garnet in sample MM03-48. Abbreviation: Qtz, Quartz inclusion. The vertical lines show the locations of compositions used for estimating the P-T conditions. Tick marks in (D) are plotted on the almandine traverses; the each tick corresponds to the location of an analysis. The length of the tick has no statistical significance.

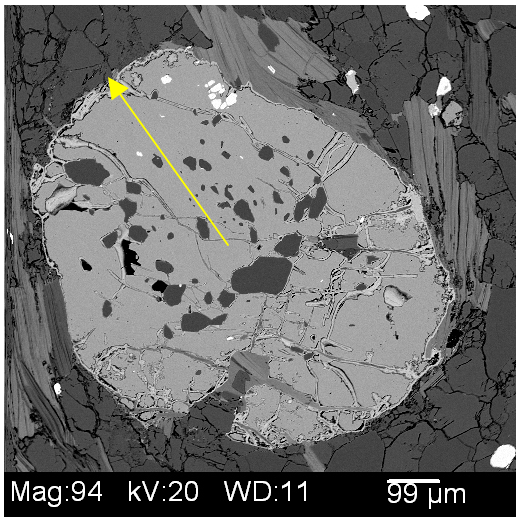

Figure 5.34 BSE image of sample MM03-48. Arrow indicates where the traverse obtained. Arrow head indicates the end point.

Only the mineral compositions from sample MM03-48 (Table 5.7) were used for thermobarometric calculations. Figure 5.35 shows the P-T conditions of this sample (640±50°C and 12.2±2.6 kbar). This condition is consistent with the mineral assemblage (Table 4.1) and the baric condition is the highest estimated for samples in this study. The thermal condition is consistent with the compositional traverses (Figure 5.33) that show the sample preserves its prograde zoning with minor retrograde diffusion at the rim.

Table 5.7 Mineral composition of MM03-48 used in thermobarometric calculations.

	Garnet[b]	Garnet	Biotite[b]	Biotite	Plag[b]	Plag	Mus[b]	Mus
SiO_2	38.46	38.03	39.89	36.57	64.31	65.82	46.89	45.74
Al_2O_3	22.09	21.79	21.33	19.95	24.05	23.10	37.31	35.77
MnO	0.34	0.38	0.06	0.07	-	0.07	-	0.01
MgO	3.54	3.52	10.76	10.55	0.01	-	0.74	0.90
CaO	3.75	3.14	0.20	0.11	3.18	2.92	0.02	-
Na_2O	0.03	-	0.19	0.17	9.54	6.77	1.04	1.47
FeO	30.74	30.63	14.38	16.73	0.06	0.12	0.80	0.89
TiO_2	0.06	1.91	1.39	1.43	-	-	0.35	0.54
Cr_2O_3	0.08	0.03	0.01	-	-	-	0.09	0.07
K_2O	-	-	6.79	7.39	0.09	0.07	6.58	8.79
Total	99.1	99.4	95.0	93.0	101.2	98.9	93.8	94.2
Si	2.96	2.97	5.76	5.54	2.80	2.89	6.16	6.11
Al	2.05	2.00	3.63	3.56	1.23	1.19	5.78	5.63
Mn	0.06	0.08	0.01	0.01	-	-	-	-
Mg	0.44	0.49	2.31	2.38	-	-	0.14	0.18
Ca	0.29	0.22	0.03	0.02	0.15	0.14	-	-
Na	-	-	0.05	0.05	0.80	0.58	0.26	0.38
Fe	2.21	2.26	1.74	2.12	-	-	0.09	0.10
Ti	-	-	0.15	0.16	-	-	0.03	0.05
Cr	-	0.01	-	-	-	-	0.01	0.01
K	-	-	1.25	1.43	-	-	1.10	1.50
Total [a]	8.0	8.0	14.93	15.26	4.99	4.81	13.59	13.96

a. "-" indicates measured but not detected.

b. Formula of garnet is calculated on the basis of 12 oxygens, biotite and muscovite are calculated on the basis of 24 oxygens, and plagioclase is calculated on the basis of 8 oxygens.

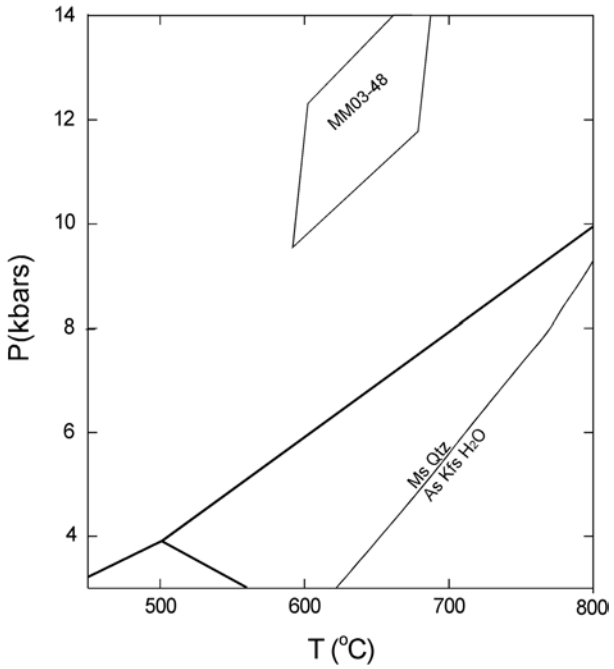

Figure 5.35 P-T diagram of transect C-C' sample MM03-48. Also shown is the stability field of the aluminosilicate polymorphs and muscovite dehydration melting curve (Chatterjee and Johannes, 1974). Abbreviations: Ms, muscovite; Qtz, quartz; As; Aluminosilicate; Kfs; K-Feldspar.

5.3 Discussion and Conclusions

This thesis presents 60 new X-ray element garnet maps and 6 new P-T conditions from garnet-bearing assemblages from the Menderes Massif. Thermobarometric results are often used to develop models for the evolution of the Menderes Massif. However, the results presented in this thesis show that rocks from this area have a potential to have experienced different metamorphic events, thus recording a polymetamorphic history. Several themes emerge from the data reported in this thesis.

1. *X-ray element garnets maps and transects across garnets from samples collected from the same unit, even the same outcrop, in the central Menderes Massif show very different zoning profiles*. For example, garnets from samples MM03-22 and MM03-23 from the same outcrop along transect A-A' (Figure 5.2) have similar Mn and Ca zoning, but very different Fe and Mg zoning (Figures 5.4 and 5.5), suggesting the rocks

experienced similar baric conditions, but different thermal conditions. Samples MM03-26, MM03-27, and MM03-28 were collected in close proximity (Figure 5.2), but garnets in these rocks show very different Mg zoning, indicating that these rocks may have experienced different metamorphic histories.

2. *P-T conditions estimated for garnet-bearing assemblages collected from the same unit, even the same outcrop, in the central Menderes Massif show yield very different thermal conditions.* Table 5.8 and Figure 5.36 summarize the P-T conditions estimated for samples in this study. The calculations indicate that the region experienced high-grade metamorphism, and the mineral assemblages of these samples are consistent with the P-T conditions (see Table 4.1). However, the P-T conditions of two rocks collected from the same outcrop (MM03-22 and MM03-23) yield different temperature results, irresolvable within uncertainty. This observation indicates that garnets from the Menderes Massif have experienced and recorded different metamorphic events.

Table 5.8 Summary of the P-T results of the samples.

Sample (MM)	T (°C)	P (kbar)
22	650 ± 40	11.4 ± 1.6
23	505 ± 55	9.0 ± 2.4
32	715 ± 55	11.2 ± 2.2
33	680 ± 45	10.3 ± 3.1
38	640 ± 40	8.9 ± 2.3
48	640 ± 50	12.2 ± 2.6

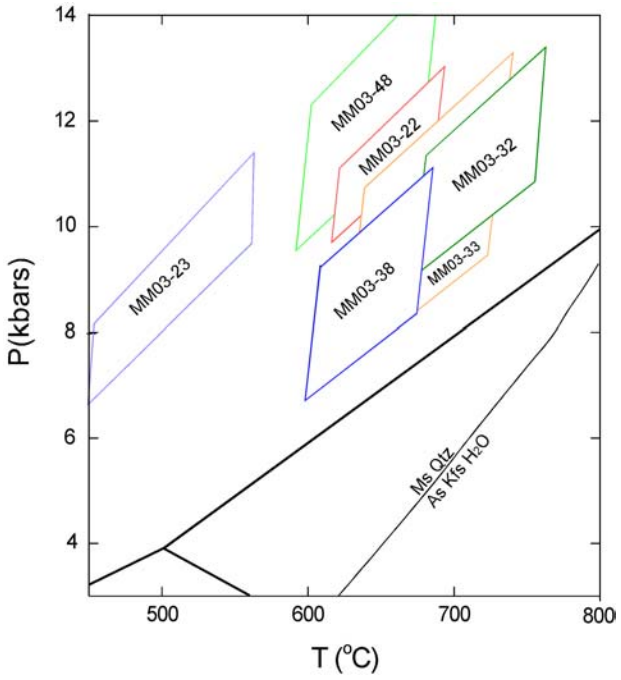

Figure 5.36 P-T diagram of all samples analyzed in this study. Also shown is the stability field of the aluminosilicate polymorphs and muscovite dehydration melting curve (Chatterjee and Johannes, 1974). Abbreviations: Ms, muscovite; Qtz, quartz; As; Aluminosilicate; Kfs; K-Feldspar.

3. *P-T conditions reported here for Menderes Massif garnet-bearing assemblages are consistent with those estimated by previous researchers.* The results obtained from the garnet-bearing assemblages in this thesis are plotted in Figure 5.37 to show their relationship to the results obtained by previous researchers. Overall, the data appear consistent, but some of the garnets we analyzed may not have grown in equilibrium with their matrix minerals. Thus, the possibility of polymetamorphic garnet growth in the central Menderes Massif has implications on previous results produced by garnet-based thermobarometric methods. We suggest for future work that multiple samples from the same outcrop be analyzed for consistency of the P-T results. For example, we have confidence in the P-T conditions of samples MM03-33 and MM03-38, as they were collected in close proximity of each other and yield similar peak conditions and garnet

zoning (Figure 5.26; Table 5.8). However, samples MM03-22 and MM03-23 were collected adjacent to each other, but yield very different peak conditions and garnet zoning (Figure 5.10; Table 5.8).

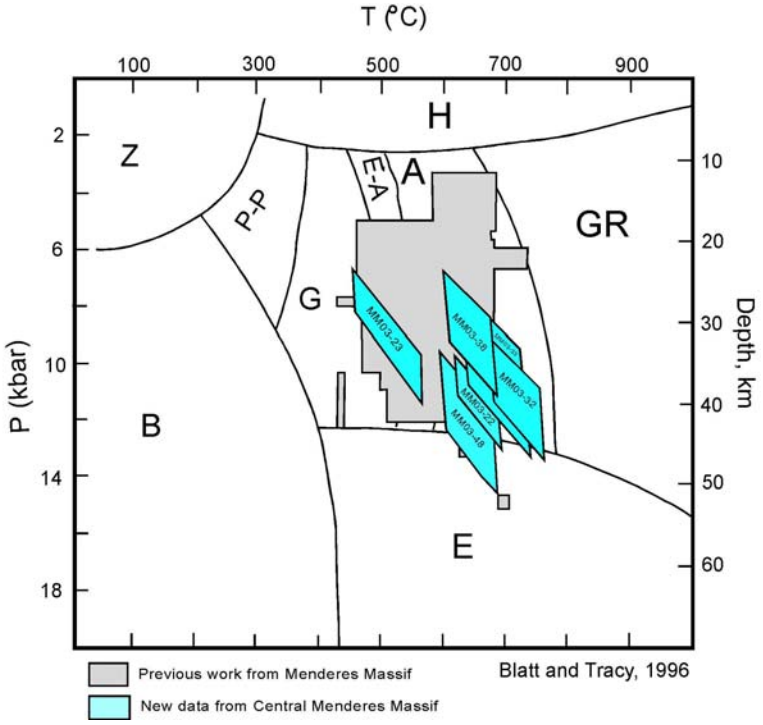

Figure 5.37 Plot of P (depth) – T plane showing distribution of metamorphic facies and P-T results from Menderes Massif samples (after Blatt and Tracy, 1996). See Figure 2.6 for references of previous work.

The same processes that govern garnet growth in other areas are the same as those that operate in the Menderes Massif; however this area has experienced a complicated multi-phase metamorphic history. In this case, some of the garnets grew in different rocks at different times, perhaps during the Pan African and during Eocene-Oligocene compression (Figure 2.5). Instead of having a single outcrop undergoing polymetamorphism, rocks of different histories and compositions were juxtaposed together at different times. The major conclusion from the observation that two garnets of

very different P-T conditions and compositions are present in the same outcrop suggests that assuming a simple metamorphic history and trying to get P-T conditions using garnets in the Menderes Massif should be done only by understanding how and when exactly the mineral appeared in these rocks.

To broaden our perspective, further geochronologic work using other thermobarometric indicators could help to improve the interpretation of the metamorphic history of the Menderes Massif. In situ ion microprobe dating of monazite (e.g., Catlos and Çemen, 2004) would be useful, particularly of garnet-bearing samples from the same outcrop. Then, the thermobarometric conditions of the high-grade metamorphic rocks in the region can be used to evaluate and develop models that explain large-scale extension.

REFERENCES

Akkök, R., 1983. Structural and metamorphic evolution of the northern part of the Menderes massif: new data from the Derbent area and their implication for the tectonics of the massif. J. Geol. 91, p. 342 – 350.

Ashworth, J.R., Evirgen, M.M., 1984. Garnet and associated minerals in the southern margin of the Menderes Massif, southwest Turkey. Geol. Mag. 121 (4), p. 323- 337

Ashworth, J.R., Evirgen, M.M., 1985. Plagioclase relations in pelites, Menderes Massif, Turkey; II. Perturbation of garnet-plagioclase geobarometers. J. Metamorphic Geology, 3. p. 219 – 229.

Berkhemer, H., 1977. Some aspects of the evolution of marginal seas deduced from observations in the Aegean regions, *in* Biju-Duval, B., and Montadert, L., eds., Structural history of the Mediterranean basins: Paris, Editions Technip, p. 303 – 313.

Berman, R.G., 1990. Mixing properties of Ca-Mg-Fe-Mn garnets. American Mineralogist, 75. p. 328-344

Bozkurt, E., Park, G.R., 1994. Southern Menderes Massif: an incipient metamorphic core complex in western Anatolia, Turkey. J. Geol. Soc. London 151, p. 213 – 216.

Bozkurt, E., 1996. Metamorphism of Paleozoic schists in the Southern Menderes Massif: Field, petrographic, textural and microstructural evidence. Turkish J. Earth Sci. 5, p. 105 – 121.

Bozkurt, E., Satır, M., 1999. Age of Alpine extensional shear zone in the southern Menderes Massif and its tectonic significance, western Turkey; A Rb-Sr geochronology. EUG 10 J. Conf. Abst. 4:34

Bozkurt, E., 2001. Late Alpine evolution of the central Menderes Massif, western Turkey. Int. J. Earth Sci. 89, p. 728-744.

Bozkurt, E., Oberhaensli, R., 2001a. Menderes Massif (western Turkey): Structural, metamorphic and magmatic evolution: A synthesis. Int. J. Earth Sci. 89, p. 679-708.

Bucher, K., Frey, M., 1994. Petrogenesis of Metamorphic Rocks. p. 114 – 144.

Buck, W.R., 1988. Flexural rotation of normal faults. Tectonics 7, p. 959 – 973.

Buick, I.S., 1991. The late-Alpine evolution of an extensional shear zone, Naxos, Greece, J. Geol. Soc. London 148, p. 93 – 103.

Candan, O., Dora, O.O., Oberhaensli, R., Çetinkaplan, M., Partzsch, J.H., Warkus, F.C., Dűrr, S., 2001. Pan-African high-pressure metamorphism in the Precambrian basement of the Menderes Massif, western Anatolia, Turkey. Int. J. Earth Sci. 89, p. 793 – 811.

Catlos, E.J., Çemen, I., Işık, V., Seyitoglu, G., 2002. In situ timing constraints from the Menderes Massif, Western Turkey. GSA Fall 2002 Meeting.

Catlos, E.J., Çemen, I., 2004. Monazite ages and rapid exhumation of the Menderes Massif, western Turkey. Int. J. Earth Sci. in press.

Çemen, I., Göncűoglu, C., Dirik, K., 1999. Structural Evolution of the Tuzgölű Basin in Central Anatolia, Turkey. J. Geol. 107, no. 6, p. 693 – 706.

Chatterjee, N.D., Johannes, W., 1974. Contributions to Mineralogy and Petrology, 48. p. 89 – 114.

Coney, P.J., 1980. Cordilleran metamorphic core complexes; an overview. In: Crittenden, M.D., Coney, P.J., Davis, G.H. (Eds.), Cordilleran Metamorphic Core Complexes. Geol. Soc. Am. Mem., vol. 153, p. 7 – 31.

Deer, W.A., Howie, R.A., Zussman, J., 1992. An introduction to The Rock-Forming Minerals. p. 31 – 46.

Dewey, J.F., 1988. Extensional collapse of orogens. Tectonics 7, p. 1123 – 1139

Doglioni, C., Gueguen, E., Harabaglia, P., Mongelli, F. 1999. On the origin of west-directed subduction zones and applications to the western Mediterranean, In: Durand, B., Jolivet, L., Horvath, F., Seranne, M. (eds). The Mediterranean Basins: Tertiary Extension within Alpine Orogen. Geol Soc London Spec Pub, London, UK, 156. p. 541 – 561.

Dora, O.Ö., Kun, N., Candan, O., 1990. Metamorphic history and geotectonic evolution of the Menderes Massif. In Proceedings of the International Earth Sciences Congress on Aegean Regions (eds M. Y. Savascin and A. H. Eronat), Geological Society of Greece. p. 102 – 115.

Dora, O.Ö., Candan, O., Kaya, O., Dűrr, S., Oberhaensli, R., 1995. New evidence on the geotectonic evolution of the Menderes Massif. Proceedings of International Earth Sciences Colloquium on the Aegean Region, 4-14 October 1995, Izmir / Gűllűk – Turkey, p. 53 – 72.

Dűrr, S., 1975. Űber Alter und geotektonische Stellung des Menderes-Kristallins/SW-Anatolien und seine Aequivalente in der mittleren Aegaeis. PhD Thesis, Univ. Marburg/Lahn, Germany. pp. 106

Emre, T., Sözbilir, H., 1997. Field evidence for metamorphic core complex, detachment faulting and accommodation faults in the Gediz and Buyuk Menderes grabens (western Turkey). Int. Earth Sci. Coll. Aegean Reg. Izmir Proc. 1: p. 73-93.

Ferry, J.M., Spear, F.S., 1978. Experimental calibration of partitioning of Fe and Mg between biotite and garnet. Contributions to Mineralogy and Petrology, 66. p. 113 – 117.

Florence, S.P., Spear, F.S., 1991. Effects of diffusional modification of garnet growth zoning on P-T path calculations. Contributions to Mineralogy and Petrology, 107, p. 487 – 500.

Gessner, K., Ring, U., Passchier, C.W., Johnson, C., Hetzel, R., Gűngör, T., 2001. An active bivergent rolling-hinge detachment system: Central Menderes metamorphic core complex in western Turkey. Geology 29, p. 611 – 614.

Gilley, L.D., 2001. Timing of Left-lateral Shearing and Prograde Metamorphism along the Red River Shear Zone, China and Vietnam. Master's Thesis, Univ. of California Los Angeles, CA, USA. pp. 199

Görűr, N., Şengör, A.M.C., Sakınc, M., 1995. Rift formation in the Gokova region, southwest Anatolia: implications for the opening of the Aegean Sea. Geol. Mag. 132, p. 637 – 650.

Hetzel, R., Ring, U., Akal, C., Troesch, M., 1995a. Miocene NNE-directed extensional unroofing in the Menderes Massif, southwestern Turkey. J. Geol. Soc. London 152, p. 639 – 654.

Hetzel, R., Passchier, C.W., Ring, U., Dora, O.Ö., 1995b. Bivergent extension in orogenic belts; the Menderes Massif (southwestern Turkey). Geology 23, p. 455-458.

Hetzel, R., Reischmann, 1996. Intrusion age of Pan-African augen gneisses in the southern Menderes Massif and the age of cooling after Alpine ductile extensional metamorphism. Geol. Mag. 133, p. 505 – 572.

Hetzel, R., Romer, R., Candan, O., Passchier, C.W., 1998. Geology of the Bozdag area, central Menderes Massif, SW Turkey: Pan-African basement and Alpine deformation. Int. J. Earth Sci. 87, p. 394 – 406.

Hoisch, T.D., 1990. Empirical calibration of six geobarometers for the mineral assemblage quartz+muscovite+biotite+plagioclase+garnet. Contributions to Mineralogy and Petrology, 104. p. 225 – 234.

Işık, V., Tekeli, O., 2001. Late orogenic crustal extension in the northern Menderes Massif (western Turkey): evidence for metamorphic core complex formation. Int J. Earth Sci. 89, p. 757 – 765.

Işık, V., Seyitoglu, G., Çemen, I., 2003. Ductile-brittle transition along the Alasehir detachment fault and its structural relationship with the Simav detachment fault, Menderes massif, western Turkey. Tectonophysics, 374. p. 1 – 18.

Işık, V., Tekeli, O., Seyitoglu, G., 2004. The $^{40}Ar/^{39}Ar$ age of extensional ductile deformation and granitoid intrusion in the northern Menderes core complex: implications for the initiation of extensional tectonics in western Turkey. Journal of Asian Earth Sciences, article in press.

Jolivet, L., Tamaki, K., Fournier, M., 1994. Japan Sea, opening history and mechanism, a synthesis. J. Geophys. Res., 96. p. 4367 – 4384.

Johnsen, O., 2002. Minerals of the World. p. 256 – 261.

Klein, C., 2002. The Manual of Mineral Science. p. 326 – 328.

Kohn, M.J., Spear, F., 2000. Retrograde net transfer reaction insurance for pressure-temperature estimates. Geology 28, p. 1127 – 1130.

Konak, N., 2002. The Geological Map of Turkey. General Directorate of Mineral Research and Exploration. Izmir Area Map.

Koralay, E., Satır, M., Dora, O.Ö., 1998. Geochronologic evidence of Triassic and Precambrian magmatism in the Menderes Massif, west Turkey. Abstr 3rd Int. Turk. Geol. Symp. Ankara, p. 1 – 285.

Le Pichon, X., Angelier, J., 1979. The Hellenic arc and trench system; A key to the neotectonic evolution of the eastern Mediterranean area. Tectonophysics, 60. p. 1 – 42.

Le Pichon, X., Angelier, J., 1981. The Aegean Sea. Phil Trans Royal Soc. London A 300, p. 357 – 372.

Lister, G.S., Banga, G., Feenstra, A., 1984. Metamorphic core complexes of Cordilleran type in the Cyclades, Aegean Sea, Greece. Geology 12, p. 221 – 225.

Lips, A.L.W., Cassard, D., Sözbilir, H., Yılmaz, H., 2001. Multistage exhumation of the Menderes Massif, western Anatolia (Turkey). Int. J. Earth Sci. 89, p. 781 – 792.

Loos, S., Reischmann, T., 1995. Geochronological data on the southern Menderes Massif, SW Turkey, obtained by single zircon Pb evaporation. Terra Abstracts, 5, p. 353.

Loos, S., Reischmann, T., 1999. The evolution of the southern Menderes Massif in SW Turkey as revealed by zircon dating. J. Geol. Soc. London 156, p. 1021 – 1030.

Meulenkamp, J.E., Wortel, M.J.R., Van Wamel, W.A., Spakman, W., Hoogerduyn, S.E., 1988. On the Hellenic subduction zone and the geodynamic evolution of Crete since the late middle Miocene. Tectonophysics, 146. p. 203 – 215.

Oberhaensli, R., Candan, O., Dora, O.O., Duerr, S.H., 1997. Eclogites within the Menderes Massif, western Turkey. Lithos, 41. p. 135 – 150.

Oberhaensli, R., Partzsch, J.H., Candan, O., Çetinkaplan, M., 2001. First occurrence of Fe-Mg-carpholite documenting a high-pressure metamorphism in metasediments of the Lycian nappes, SW Turkey. Int. J. Earth Sci. 89, p. 867 – 873.

Okay, A.I., 2001. Stratigraphic and metamorphic inversions in the central Menderes Massif: a new structural model. Int J Earth Sci. 89, p. 709 – 727.

Okay, A.I., Satir, M., 2000. Coeval plutonism and metamorphism in a latest Oligocene metamorphic core complex in northwest Turkey. Geol. Mag. 137, p. 495 – 516.

Passchier, C. W., Trouw, R. A. J., 1996. Microtectonics. Springer, Berlin Heidelberg New York. pp. 1-304.

Pyle, J., Spear, F.S., 1999. Yttrium zoning in garnet: Coupling of major and accessory phases during metamorphic reactions. Geological Materials Research, v1n6: p. 1 – 49.

Reed, S.J.B., 1993. Electron Microprobe Analysis. p. 161 – 185.

Reed, S.J.B., 1996. Electron Microprobe Analysis and Scanning electron microscopy in Geology. p. 126 – 152.

Régnier, J.L., Ring, U., Passchier, C.W., Gessner, K., Gűngör, T., 2003. Contrasting metamorphic evolution of metasedimentary rocks from the Cine and Selimiye nappes in the Anatolide belt, western Turkey. J. Metamorphic Geology, 21. p. 699 – 721.

Reischmann, T., Kroener, A., Todt, W., Duerr, S., Şengör, A.M.C., 1991. Episodes of crustal growth in the Menderes Massif, West Turkey, inferred from zircon dating. EUG Terra Abstracts 3, p. 34.

Rimmele, G., Oberhaensli, R., Goffe, B., Jolivet, L., Candan, O., Çetinkaplan, M., 2003. First evidence of high-pressure metamorphism in the "Cover Series" of the southern Menderes Massif: tectonic and metamorphic implications for the evolution of SW Turkey. Lithos, 71. p. 19 – 46.

Ring, U., Gessner, K., Gűngör, T., Passchier, C.W., 1999. The Menderes Massif of western Turkey and the Cycladic massif in the Aegean: Do they really correlate? J. Geol. Soc. London 156, p. 3 – 6.

Ring, U., Willner A.P., Lackmann, W., 2001. Stacking of nappes with different pressure-temperature paths; an example from the Menderes Nappes of western Turkey. Am. J. Sci. 301. p. 912 – 914.

Satır, M., Friedrichsen, H., 1986. The origin and evolution of the Menderes Massif, W-Turkey: A rubidium/strontium and oxygen isotope study. Int. J. Earth Sci.75, p. 703 – 714.

Schellart, W.P., Lister, G.S., Jessell, M.W., 2002. Analogue modeling of asymmetrical back-arc extension. In: Schellart, W.P. and Passchier, C., 2002. Analogue modeling of large-scale tectonic processes. J. Virtual Explorer, 7, p. 25 – 42.

Seyitoglu, G., Scott, B.C., 1991. Late Cenozoic crustal extension and basin formation in West Turkey. Geol. Mag. 128, p. 155 – 166.

Seyitoglu, G., Scott, B.C., 1992. Rundle Timing of Cenozoic extensional tectonics in West Turkey. J. Geol. Soc. London 157, p. 533 – 538.

Seyitoglu, G., Scott, B. C. 1996a. Age of Alasehir graben (west Turkey) and its tectonic implications. Geological Journal, 31, p. 1 – 11.

Seyitoglu, G., Scott, B.C., 1996b. The cause of N-S extensional tectonics in western Turkey: Tectonic escape vs. back-arc spreading vs. orogenic collapse. J. Geodyn 22, p. 145 – 153.

Seyitoglu, G., Tekeli, O., Çemen, I., Şen, Ş., Işık, V., 2002. The role of the flexural rotation/rolling hinge model in the tectonic evolution of the Alasehir graben, western Turkey. Geol. Mag. 139, p. 15 – 26.

Şengör, A.M.C., Yılmaz, Y., 1981. Tethyan evolution of Turkey: A plate tectonic approach. Tectonophysics, 75. p. 181 – 241.

Şengör, A.M.C., Satır, M., Akkök, R., 1984. Timing of tectonic events in the Menderes Massif, western Turkey: implications for tectonic evolution and evidence for Pan-African basement in Turkey. Tectonics 3, p. 693 – 707.

Şengör, A.M.C., Görűr, N., Saroglu, F., 1985. Strike-slip faulting and related basin formation in zones of tectonic escape; Turkey as a case study. Spec. Pub. Soc. Econ. Paleo. Mineral 37, p. 227 – 264.

Simpson, R.L., Parrish, R.R., Searle, M.P., Water, D.J., 2000. Two episodes of monazite crystallization during metamorphism and crustal melting in the Everest region of the Nepalese Himalaya. Geology 28, p. 403 – 406.

Smith, H.A., Barriero, B., 1990. Monazite U-Pb dating of staurolite grade metamorphism in politic schists. Contributions to Mineralogy and Petrology, 105, p. 602 – 615.

Sözbilir, H., Emre, T., 1996. Supradetachment basin and rift basin developed during the neotectonic evolution of the Menderes Massif. Abstracts, 49th Geological Congress of Turkey, p. 30 – 31.

Sözbilir, H., 2001. Extensional Tectonics and the Geometry of Related Macroscopic Structures: Field Evidence from the Gediz Detachment, Western Turkey. Turkish J. Earth Sci. 10, p. 51 – 67.

Spear, F.S., 1993. Metamorphic Phase Equilibria and Pressure – Temperature – Time Paths. Mineralogical Society of America Washington DC, pp 1 – 799.

Spear, F.S., Kohn, M.J., 1999. Program Thermobarometry v2.1, Rensselear Polytechnic Institute, Troy, NY, pp. 43.

Spear, F.S., Peacock, S.M., 1989. Metamorphic Pressure-Temperature-Time Paths, Short Course in Geology, 7, p. 1 – 55.

Stampfli, G.M., 2000. Tethyan oceans. In Bozkurt E., Winchester, J.A., Piper JDA (eds). Tectonics and Magmatism in Turkey and the Surrounding Area. Geol. Soc. London Spec Pub, London UK, 173, p. 1 – 23.

Tapponnier, P., Peltzer, G., Le Dain, A.Y., Armijo, R., Cobbold, P., 1982. Propagating extrusion tectonics in Asia: New insights from simple experiments with plasticine. Geology, 10. p. 611 – 616.

Townsend, K.J., Miller, C.F., D'Andrea, J.L., Ayers, J.C., Harrison, T.M., Coath, C.D., 2000. Monazite replacement during modification of the Ireteba granite, southern Nevada: Geochronological implications. GSA Abstracts with Programs, 30: A214.

Vanderhaeghe, O., Teyssier, C., 2001. Partial melting and flow of orogens. Tectonophysics, 342. p. 451 – 472.

Whitney, D. L., Bozkurt, E., 2002. Metamorphic history of the southern Menderes Massif, western Turkey. GSA Bulletin 114: 829 – 838.

Yılmaz, Y., Genç, S.C., Gűrer, F., Bozcu, M., Yılmaz, K., Karacik, Z., Altunkaynak, S., Elmas, A., 2000. When did the western Anatolian grabens begin to develop? In: Bozkurt E., Winchester, J.A., Piper JDA (eds). Tectonics and Magmatism in Turkey and the Surrounding Area. Geol. Soc. London Spec. Pub., London UK, 173, p. 353 – 384.

Yin, A., Harrison, T.M., 2000. Geologic evolution of the Himalayan-Tibetan orogen. Annual Review of Earth and Planetary Sciences, 28. p. 211 – 280.

APPENDIX A

Locations of the Menderes Massif rocks for future study

Mineral assemblages and locations of the rocks for future studies.[a]

Sample[a]	Northing	Easting
1	597398	4202109
2	597345	4202116
3	597207	4203118
4	597119	4202146
5	597124	4203153
6	592358	4199553
7	597492	4201887
8	597442	4201986
9	596722	4200986
10	596723	4200985
11	596263	4200426
12	594733	4194067
13	595529	4202648
14	594585	4202428
15	594586	4202430
16	594624	4202540
17	564623	4202538
18	595244	4203477
19	596206	4202213
20	596207	4202214
21	594560	4201910

a. Sample names are referred to as MM03-#.

VITA

CENK OZERDEM

Candidate for the Degree of

Masters of Science

Thesis: THERMOBAROMETRIC CONSTRAINTS ON THE EVOLUTION OF THE MENDERES MASSIF (WESTERN TURKEY): INSIGHTS INTO THE METAMORPHIC HISTORY OF A COMPLEXLY-DEFORMED REGION

Major Field: Geology

Biographical:

Personal: Born in Ankara, TURKEY, August 17, 1978, the son of F. Erkan and F. Gulay Ozerdem.

Education: Graduated from T.E.D. Ankara College, May, 1995; attended Ankara University 1996-2001; received Bachelor of Science Degree in Geological Engineering; completed requirements for Masters of Science degree at Oklahoma State University in July, 2004.

Professional Experience: 01/2004 – 05/2004: Teaching assistant for Electron Microprobe Analyses and Physical Geology; 08/2003 – 12/2003: Teaching assistant for Practical Mineralogy; 01/2002 – 05/2002: Teaching assistant for Physical Geology; 08/2001 – 12/2002: Teaching assistant for Practical Mineralogy. Members of Society of Turkish Geological Engineers, Geological Society of America, Mineralogical Society of America, American Geophysical Union, American Association of Petroleum Geologists (Student chapter secretary in 2002-2003), Friends of Mineralogy, Midwest Chapter, Sigma Gamma Epsilon (SGE) Earth Science Honor Society, Oklahoma State University Geological Society (Secretary in 2002-2003) Stillwater Gem and Mineral Society (Oklahoma) Tulsa Rock and Mineral Society (Oklahoma)